Radiation Damage and Inert Gas Bubbles in Metals

by

Xiao Gai

June 15, 2015

Abstract

Inert gases in metals can occur due to ion implantation, from a plasma in a magnetron device or as a result of being by-products of nuclear reactions. Mainly because of the nuclear applications, the properties of the inert gases, helium, argon and xenon in the body centred cubic (bcc) iron crystal are examined theoretically using a combination of molecular dynamics, static energy minimisation and long time scale techniques using empirical potential functions. The same techniques are also used to investigate argon and xenon in aluminium.

The primary interest of the work occurred because of He produced in nuclear fission and its effect on the structural materials of a fission reactor. This structure is modelled with perfectly crystalline bcc Fe. In bcc iron, helium is shown to diffuse rapidly forming small bubbles over picosecond time scales, which reach a certain optimum size. In the initial phase of He accumulation, Fe interstitials are ejected. This occurs instantaneously for bubbles containing 5 He atoms and as the more He accumulates, more Fe interstitials are ejected. The most energetically favourable He to vacancy ratios at 0 K, vary from $1:1$ for 5 vacancies up to about $4:1$ for larger numbers of vacancies. An existing He bubble can be enlarged by a nearby collision cascade through the ejection of Fe interstitials, allowing more He to be trapped.

Ar and Xe in bcc Fe prefer to be substitutional rather than interstitial and there are large barriers to be overcome for the inert gas atoms to diffuse from a substitutional site. Bubbles that form can again be enlarged by the presence of a nearby collision cascade or at very high temperatures. In this case the most energetically favourable vacancy ratios in the bubbles is $1:1$ for Ar and from $0.6:1$ to $0.8:1$ for Xe. For Ar and Xe, bubble formation is more likely as a direct result of radiation or radiation enhanced diffusion rather than diffusion from a substitutional site.

Ar in aluminium is also studied. Ar atoms in fcc Al prefer to be substitutional rather than interstitial and evolution into substitutional occurs over picosecond time scales at room temperature. Bubble formation can occur more easily than in bcc iron, mainly because the barriers for vacancy diffusion are much lower but the time scales for bubble accumulation are much longer than those for He. A vacancy assisted mechanism is found which allows Ar to diffuse through the lattice. Finally some preliminary results on the energetics of different geometrical structures of larger Xe bubbles in Al are investigated since experiment has indicated that these can become facetted.

Acknowledgements

First I would like to express my gratitude to my wife Ye Luo and our family for their unlimited support during this research and in all my pursuits. I am also very grateful to my supervisors Prof. Roger Smith and Prof. Steven Kenny for giving the opportunity to undertake this PhD and also for providing continued support and guidance.

I must also thank Tomas Lazauskas for the help getting started with the project and very productive discussions and the joint work on the He bubbles formation; Chris Scott for developing the atomic visualisation software and his and Miao Yu's collaboration during the software development; Kenny Jolley and Zainab Al Tooq for analysis software.

Finally, I would like to acknowledge the financial support by EPSRC and the Department of Mathematical Sciences at Loughborough University for providing the necessary facilities for the research and the Loughborough High Performance Computing centre for the computational resources.

Contents

List of Figures

List of Tables

Chapter 1

Introduction and Background

Rapidly growing energy demand and global depletion of fossils fuels force mankind to investigate other energy sources such as nuclear energy. Fission and fusion reactors are promising because of producing energy without emitting greenhouse gasses.

Neutron irradiation of metals in fission and fusion reactors results in the production of a high density of displacement defects such as vacancies and self-interstitials atoms (SIA) and produces foreign atoms through nuclear transmutations. Among these atoms, helium, argon and xenon are particularly detrimental to the mechanical properties of the materials.

These energetic particles during radiation interact with atoms of the target material and induce a large number of point defects, which aggregate to form vacancy clusters, voids, dislocation loops and stacking fault tetrahedron [1, 2, 3, 4]. Inert gases can produce swelling which leads to macroscopic distortion and volume increase of fuel rods and structural materials and will also cause intergranular embrittlement resulting in severe degradation of mechanical properties [5]. It is of great interest and technologically important to develop radiation tolerant materials that can promote the annihilation of radiation induced defects.

It has been established that inert gases play an important role on the evolution of microstructures and mechanical properties of irradiated materials [6, 7, 8]. In crystalline metals and alloys inert gas atoms can sometimes migrate interstitially below room temperature [9]

and may form bubbles by a nucleation and growth process [10, 11, 12, 13, 14]. Vacancies are involved in the nucleation process, whereas growth can occur by capturing mobile vacancies or in the prevacancy regime by loop punching [15]. Ultimately, it is the long-range diffusion of vacancy, self-interstitial defects and impurity gas atoms over long times and increasing length scales, which is responsible for nano/ microstructural evolution. Enhanced defect transport leads to a re-distribution of inert gas atoms as a consequence of radiation enhanced diffusion and segregation. This is thought by many people to occur as the result of the migration and coalescence of small inert gas bubbles which are produced by nuclear transmutation. Therefore it is necessary to understand and control those phenomena which underlay the present limitations.

Experimental and theoretical investigations are performed to model these problems, such as how inert gas atoms interact with the materials during the cascades and how ion beams effect the alloy (details are introduced in the introductions of the following separate sections). However, quantification of the inert gas atom diffusion, trapping and interaction mechanisms, the importance of small cluster mobility, bubble nucleation processes and the evolution of the bubbles in metals remain outstanding issues. A primary aim of the thesis is to investigate these mechanisms for He, Ar and Xe in α-Fe using advanced computational techniques. In addition, because of recent modelling work on the deposition of Al thin films in a magnetron device [16] and experimental work on Xe bubbles in Al [17, 18, 19, 20, 21], bubble growth in Al is also considered using the same computation techniques.

1.1 Computer Simulation

Computer simulation is an extremely powerful tool in materials science today. Generally, various techniques are available depending on what you wish to model. *Ab-initio* methods, such as density functional theory (DFT) [22] models on an atomistic level (Å) for very short time scales (up to picoseconds). Continuum methods, such as finite elements, can be used

to model situations on larger length and time scales (metres and seconds).

Classical molecular dynamics (MD) [23, 24] is also an atomistic technique used for the range from femtosecond to nanoseconds. It was first introduced in the 1950s when Alder and Wainwright studied phase transitions in a hard sphere system [23]. Vineyard *et al.* were the first to model radiation damage using MD in the 1960s [25] to model radiation events in systems containing approximately 500 atoms and MD is now one of the standard tools for the investigation of radiation.

As computers have been developed more, the system sizes that can be modelled have rapidly grown and more complex potential energy functions have been developed to model the different materials. It is now possible to model millions of atoms, and reach simulation times of the order of nanoseconds. However this is still some way short of time scales that can be measured experimentally. Hybrid techniques can be used to model even longer time scales. For example MD and on-the-fly kinetic Monte Carlo can be used together to reach simulation times of the order of seconds [26].

1.2 Research Goals

This work is a part of an EPSRC project to investigate the mechanisms of the formation and growth of inert gas bubbles in metals at the atomic level and look into the effects of processing conditions and irradiation.

Simulations compared together with experiments help in providing a wider perspective of the problem and give a deeper look into the processes that happen at the atomistic level. The simulations can help to link the results obtained before and after irradiation events that cannot be followed on an experimental time scale. Also, computer simulation allows parameters to be changed without performing costly experiments, such as temperature, energy and material composition.

1.3 Implemented and Developed Software

Some of the techniques used in the thesis are briefly described in this section together with their acronyms.

LBOMD (LoughBOrough Molecular Dynamics [27]) - collision cascades, potential energy function static minimisation.

KMC (Kinetic Monte Carlo technique [28, 29]) - bubble formation.

Atomic visualisation - a 3D visualiser written in the Python language has been used to analyse the output from the simulations in this work.

NEB (Nudged Elastic Bands method) - calculate the diffusion barriers when the pathway of the end states are known [30].

Saddle point searching methods - search the transition when the end state is not known. These can be incorporated into an otf-KMC (on-the-fly Kinetic Monte Carlo technique [28, 29]) method to study long time scale dynamics.

1.4 Thesis Layout

Chapter 1 introduces the research problems and gives reference to some of the previous work on the topic.

Chapter 2 is the methodology chapter. The first part explains the main concepts of the MD technique, potential functions and the necessary extensions to it. The second part is focussed on saddle point searching methods to determine the pathways for diffusion and the corresponding energy barriers.

Chapter 3 describes the MD and KMC simulations that were used to study the formation and growth of He bubbles in bcc Fe. The results compare two different potentials.

Chapter 4 is mainly focussed on the MD and KMC simulations that were used to study the formation and growth of Ar bubbles in bcc Fe. The results are compared with the He work in **Chapter 3**.

Chapter 5 describes the static calculations and KMC simulations that were used to study the formation of Xe bubbles and diffusion mechanisms in bcc Fe.

Chapter 6 is focussed on Ar in fcc Al. Some static calculations and diffusion mechanisms are shown in this chapter.

Chapter 7 is the final chapter, where all the achieved results are summarised and the potential future studies are highlighted.

Chapter 2

Methodology

In this section the various computational methods used in the work are described.

2.1 Molecular Dynamics

2.1.1 Introduction

The Molecular Dynamics (MD) method is an atomistic computer simulation technique introduced in the 1950s by B. J. Alder and T. E. Wainwright and has been used extensively since then [31]. It is designed to use classical mechanics to describe the time evolution of physical systems by modelling atomic and molecular interactions. The method has been proven to be an extremely powerful tool to study lots of aspects in different subjects such as radiation damage and biology.

The aim of the MD simulation is to model the motion of the N atoms in the system and how the positions and the velocities change with time, based on Newton's second law:

$$m_i \frac{d^2 \mathbf{x_i}}{dt^2} = -\nabla V\left(\mathbf{x}_1, ..., \mathbf{x}_N\right), \qquad i = 1 \ldots N, \tag{2.1}$$

where m_i is the mass of the i-th atom, whose position at time t is $\mathbf{x}_i$. Here the force

on each atom is assumed to be derived from a potential function V, which depends only on the coordinates of the atoms. The MD code utilised in this work was the LBOMD (LoughBOrough Molecular Dynamics) package. This section will outline the aspects of MD used and their implementation in this thesis.

2.1.2 Time Integration

In order to obtain the movement of the N atoms in the simulation system, a time integration algorithm is required to numerically solve the equations of motion:

$$\mathbf{F}_i = m_i \ddot{\mathbf{x}}_i, \qquad i = 1, \ldots, N, \tag{2.2}$$

where $\mathbf{x}_i$ is the position of atom i and $\ddot{\mathbf{x}}_i$ is its acceleration, m_i is its mass and $\mathbf{F}_i$ is the force acting upon the atom. Normally $\mathbf{F}_i$ is calculated from the gradient of the potential energy function, V (discussed in the next section), with respect to the atom's position:

$$\mathbf{F}_i = -\nabla_{x_i} V. \tag{2.3}$$

However, because of the complicated nature of the potential energy there is no analytical solution for the Newton's equations in MD; thus numerical algorithms must be employed. The Verlet algorithm is the most widely used algorithm to integrate time in MD simulations, which was promoted in MD simulations by L. Verlet in 1967 [31]. It combines two Taylor expansions of the position vector $\mathbf{x}$ from time t forward to $t + \Delta t$ and backward to $t - \Delta t$:

$$\mathbf{x}(t + \Delta t) = \mathbf{x}(t) + \frac{d\mathbf{x}(t)}{dt}\Delta t + \frac{1}{2}\frac{d^2\mathbf{x}(t)}{dt^2}\Delta t^2 + \frac{1}{3!}\frac{d^3\mathbf{x}(t)}{dt^3}\Delta t^3 + O(\Delta t^4), \tag{2.4}$$

$$\mathbf{x}(t - \Delta t) = \mathbf{x}(t) - \frac{d\mathbf{x}(t)}{dt}\Delta t + \frac{1}{2}\frac{d^2\mathbf{x}(t)}{dt^2}\Delta t^2 - \frac{1}{3!}\frac{d^3\mathbf{x}(t)}{dt^3}\Delta t^3 + O(\Delta t^4). \tag{2.5}$$

By adding these two expressions, odd-order terms have been eliminated:

$$\mathbf{x}(t+\Delta t) = 2\mathbf{x}(t) - \mathbf{x}(t-\Delta t) + \frac{d^2\mathbf{x}(t)}{dt^2}\Delta t^2 + O(\Delta t^4), \tag{2.6}$$

Thus we make this integrator an order more accurate than the Taylor expansion alone and also steps do not depend on velocities, only on acceleration $\frac{d^2\mathbf{x}(t)}{dt^2}$, which can be derived from intermolecular forces and Newton's second law. By employing the Taylor expansion an alternative formulation, the Velocity Verlet algorithm can be derived as follows:

$$\mathbf{x}(t+\Delta t) = \mathbf{x}(t) + \mathbf{v}(t)\Delta t + \frac{1}{2}\mathbf{a}(t)\Delta t^2 + O(\Delta t^3), \tag{2.7}$$

$$\mathbf{v}(t+\Delta t) = \mathbf{v}(t) + \mathbf{a}(t)\Delta t + \frac{1}{2}\frac{d\mathbf{a}(t)}{dt}\Delta t^2 + O(\Delta t^3), \tag{2.8}$$

$$\mathbf{a}(t+\Delta t) = \mathbf{a}(t) + \frac{d\mathbf{a}(t)}{dt}\Delta t + O(\Delta t^2), \tag{2.9}$$

where $\mathbf{v}(t) = \frac{d\mathbf{x}(t)}{dt}$ and $\mathbf{a}(t) = \frac{d\mathbf{v}(t)}{dt}$. After updating the positions using (2.9) we can derive:

$$\frac{d\mathbf{a}(t)}{dt} = \frac{\mathbf{a}(t+\Delta t) - \mathbf{a}(t)}{\Delta t} + O(\Delta t^2). \tag{2.10}$$

By substituting the last expression into Equation 2.8 we will get an expression in Equation 2.11 to calculate the new velocities, that can be used in Equation 2.7.

$$\boldsymbol{v}(t+\Delta t) = \boldsymbol{v}(t) + \frac{1}{2}\left[\boldsymbol{a}(t+\Delta t) + \boldsymbol{a}(t)\right]\Delta t + O(\Delta t^2). \tag{2.11}$$

This is the form of the algorithm implemented in LBOMD (Loughborough molecular dynamics) that is a package developed at Loughborough University [27] and is used throughout this project to perform all MD simulations. The code was written to allow the user to monitor the parameters of the simulation such as simulation time, system temperature, thermostat type, the constraints of the boundary conditions, the frequency of data writing and the

parameters required for the collision cascades.

LBOMD uses a variable time step dependant on the maximum kinetic energy and the maximum positive potential energy:

$$\Delta t = \frac{1.5}{\sqrt{1.5 + 0.1T_s}}, \tag{2.12}$$

where T_s is the sum of the maximum kinetic energy and maximum positive potential energy in the system. A typical time step is 1 fs (1×10^{-15} s).

2.1.3 Interatomic Potentials

Choosing the right interatomic potential $V(\mathbf{x}_1, \ldots, \mathbf{x}_N)$ depending on the positions $\mathbf{x}_1, \ldots, \mathbf{x}_N$ of the N atoms in the system to represent the interaction is crucial in an MD simulation. The general many-body form of the interatomic potential energy function is to sum over increasing numbers of atoms [32]:

$$V_{TOT} = \sum_{i,j} V_2(\mathbf{x}_i, \mathbf{x}_j) + \sum_{i,j,k} V_3(\mathbf{x}_i, \mathbf{x}_j, \mathbf{x}_k) + \ldots, \tag{2.13}$$

where V_2 is the interaction between pairs of atoms $\{i, j\}$, V_3 the interaction between triplets of atoms $\{i, j, k\}$, and so on.

For the simulations presented here, two types of interatomic potentials were used: pair potentials and Finnis-Sinclair type potentials [33].

2.1.3.1 Pair Potentials

The pair potential is the earliest and simplest form of potential:

$$U = \frac{1}{2} \sum_{i,j(i \neq j)} V_{ij}\left(r_{ij}\right), \tag{2.14}$$

where U is the total potential energy of the whole system, V_{ij} is the pair potential energy function and r_{ij} is the separation between atoms i and j.

It has been shown that a pair potential can represent the interaction of noble gases very well, however, its drawbacks appear when used for metals, such as its inability to reproduce elastic constants accurately [33]. The advantage of the pair potential is the ease to be implemented and computed efficiently due to their simplicity.

2.1.3.1.1 L-J

The Lennard-Jones 6-12 potential is one of the pair potentials used to describe the interaction of noble gases [34, 35]. It has the form:

$$\phi(r_{ij}) = -\frac{A}{r_{ij}^{6}} + \frac{B}{r_{ij}^{12}}, \tag{2.15}$$

where A and B are positive constants, and r_{ij} is the distance between atoms. The potential is usually written in the following form

$$\phi(r_{ij}) = 4\epsilon[(\frac{\sigma}{r_{ij}})^{12} - (\frac{\sigma}{r_{ij}})^{6}], \quad \sigma = (B/A)^{\frac{1}{6}}, \quad \epsilon = \frac{A^2}{4B}. \tag{2.16}$$

The values of ϵ and σ that fit the solid gas phases are displayed in Table 2.1 [34].

	Ar	Kr	Xe
$\epsilon(eV)$	0.0104	0.0140	0.02
$\sigma(\mathring{A})$	3.40	3.65	3.98

Table 2.1: Values of the Lennard-Jones Parameters for the noble gases.

However the repulsive part of the potential for small particle separation is inadequate and so here another approach is required.

2.1.3.1.2 ZBL

At the short ranges, most of the potentials fail to correctly represent the interactions between the atoms. Therefore, it is preferable to use another potential to describe the interactions at

very small distances. The well-known screened Coulomb ZBL universal repulsive potential [36] developed by Ziegler, Biersack and Littmark models this close range interaction by multiplying the Coulombic potential between the atom cores with a screening function.

The ZBL potential is a function of the atomic numbers Z_1, Z_2 of atoms i and j, the interatomic separation r_{ij} and the screening function φ and is shown in the following equation:

$$V_{ZBL}(r_{ij}) = \frac{1}{4\pi\varepsilon_0}\frac{Z_1 Z_2 e^2}{r_{ij}}\varphi(\frac{r_{ij}}{a}), \tag{2.17}$$

where e - electronic charge, ε_0 the permittivity of free vacancy, a - a screening parameter. The forms of screening function φ and parameter a are respectively given in Equations 2.18 and 2.19:

$$\varphi(x) = 0.1818e^{-3.2x} + 0.5099e^{-0.9423x} + 0.2802e^{-0.4029x} + 0.02817e^{-0.2016x}, \tag{2.18}$$

$$a = \frac{0.8854a_0}{Z_1^{0.23} + Z_2^{0.23}}, \tag{2.19}$$

where a_0 - the Bohr atomic radius = 0.530Å.

The ZBL potential in this work was implemented to estimate interactions for Ar-Fe, Xe-Fe and Ar-Al.

2.1.3.1.3 Aziz

The Aziz potential [37] is used to describe the He-He interaction in this thesis and has the Hartree-Fock-dispersion form [38] and is reported to have a good agreement with the *ab-initio* results.

$$V_{Aziz}(x) = \epsilon\left(A\exp\left(-\alpha x + \beta r_{ij}^2\right) - F(x)\sum_{j=0}^{2} c_{2j+6}/x^{2j+6}\right), \tag{2.20}$$

with

$$F(x) = \begin{cases} \exp\left[-\left(\frac{D}{x}-1\right)^2\right], & x < D \\ 1, & x \geq D \end{cases}, \tag{2.21}$$

where $x = r_{ij}/r_m$. The values of the constants are given in Table 2.2 and the form of the potential is shown in Figure 2.1.

A	α	c_6	c_8	c_{10}
1.86924404×10^5	10.5717543	1.35186623	0.41495143	0.17151143
$\beta(\text{Å}^{-2})$	D(Å)	ϵ(eV)	r_m(Å)	
-2.358	1.438	9.441093×10^{-4}	0.29683	

Table 2.2: The constant values for the Aziz potential to describe the He-He interaction [37].

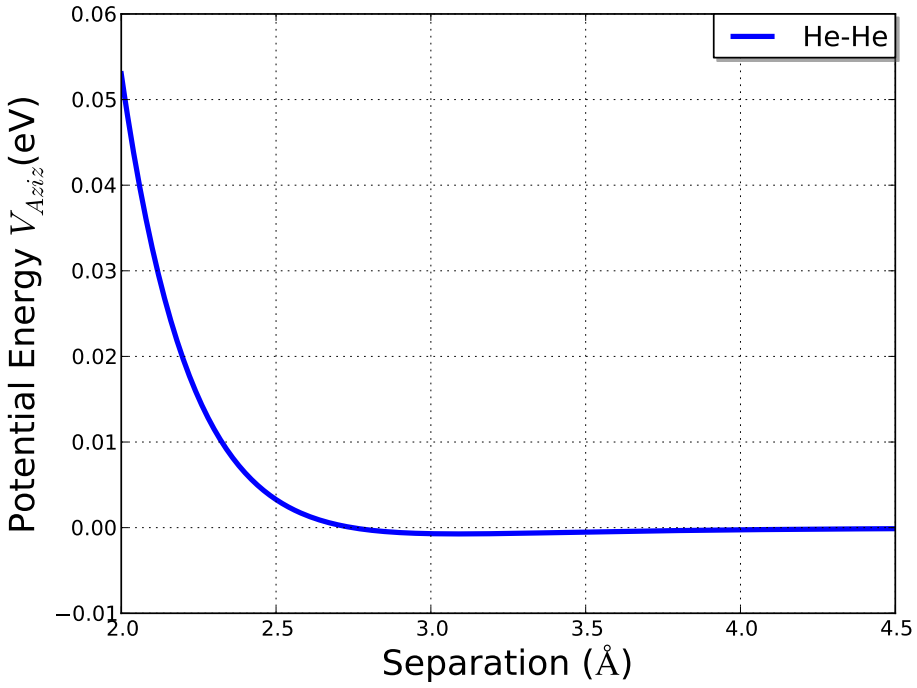

Figure 2.1: The form of the Aziz potential.

A spline function is normally used to link the potential to the ZBL potential for short ranges. There are numerous methods, but here a fifth order exponential polynomial is applied

to make the function and its first and second derivatives smooth and continuous.

$$S(r_{ij}) = e^{f_0+f_1 r_{ij}+f_2 r_{ij}^2+f_3 r_{ij}^3+f_4 r_{ij}^4+f_5 r_{ij}^5}, a \leq r_{ij} \leq b \tag{2.22}$$

where $f_0, \ldots, f_5$ are splining coefficients and r_{ij} is the atomic separation.

Cutoff distances a and b that point out where the pair potential is splined to ZBL and the outer potential are determined to ensure the functions are as smooth and continuous as possible.

2.1.3.2 Many-body Potentials

An important potential is the Embedded Atomic Method (EAM) suggested by Finnis & Sinclair (F-S) [33] and Daw & Baskes [32, 39] in 1980s. The idea behind this technique is that each atom is treated as an impurity embedded in a sea of electrons of all remaining atoms. The energy calculated by the F-S and EAM methods $V_i^{EAM}(r_{ij})$ can be expressed as

$$V_i^{EAM}(r_{ij}) = \frac{1}{2}\sum_j V_{ij}(r_{ij}) - \sum_i F(\rho_i(r_{ij})), \tag{2.23}$$

where $V_{ij}(r_{ij})$ is a central pair potential, $\rho_i(r_{ij})$ - electron density and F - an embedding function for the EAM potential specifically. Various forms for the electron density and the embedding function F have been given.

2.1.3.2.1 Ackland-Mendelev Fe-Fe

In this work, the potential developed by Ackland *et al.* based on the earlier EAM and Finnis-Sinclair type potentials is used to describe the interactions for Fe-Fe interaction. Three different sets of parameters were used [40, 41, 42] where the general form of the potentials to calculate the energy in a N atom system is :

$$E = \frac{1}{2}\sum_{i\neq j=1}^{N} V_{ij}(r_{ij}) - \sum_{i=1}^{N} F(\rho_i(r_{ij})), \tag{2.24}$$

where the first term represents a pair potential and the second the embedded part. In this thesis, we apply the Ackland 2004 [42] for computations give a better agreement with the lattice parameter, elastic constants, point-defects energies etc, obtained experimentally and by first-principles calculations. The details are given in Equations 2.25, 2.27, 2.28, 2.29 and 2.30 and Tables 2.3, 2.4 and 2.5.

$$V(r_{ij}) = \sum_k a_k H\left(r_k - r_{ij}\right)\left(r_k - r_{ij}\right)^3, \tag{2.25}$$

a_k, r_k are constants, with the values given in Table 2.4, r_{ij} is the atomic separation between atoms i and j and H is the Heaviside function:

$$H(x) = \begin{cases} 1, & x \geq 0, \\ 0, & x < 0. \end{cases} \tag{2.26}$$

$$F(\rho_i(r_{ij})) = a_0^f \left[\rho_i(r_{ij})\right]^{1/2} + a_1^f \left[\rho_i(r_{ij})\right]^2 + a_2^f \left[\rho_i(r_{ij})\right]^4. \tag{2.27}$$

$a_0^f(\mathrm{eV/\AA})$	$a_1^f(\mathrm{eV/\AA}^4)$	$a_2^f(\mathrm{eV/\AA}^8)$
-1.0	$-6.7314115586063 \times 10^{-4}$	$7.6514905604792 \times 10^{-8}$

Table 2.3: Values of the parameters in Equation 2.27 for the Fe-Fe interaction described by the Ackland 2004 potential [42].

$$\rho_i(r_{ij}) = \sum_{j=1}^{N} \Phi_{ij}(r_{ij}) \tag{2.28}$$

$$\begin{aligned} \Phi_{ij}(r_{ij}) =& 11.686859407970(2.4 - r_{ij})^3 H\left(2.4 - r_{ij}\right) \\ &- 0.01471074009883(3.2 - r_{ij})^3 H\left(3.2 - r_{ij}\right) \\ &+ 0.47193527075943(4.2 - r_{ij})^3 H\left(4.2 - r_{ij}\right) \end{aligned} \tag{2.29}$$

For the extreme short range repulsion, the screened electrostatic form of Biersack and Ziegler [43] was adopted here as shown in Equation 2.30.

$$\begin{aligned} V(r_{ij}) = & \sum_k a_k H\left(r_k - r_{ij}\right) H\left(r_{ij} - r_2\right) \left(r_k - r_{ij}\right)^3 \\ & + H\left(r_2 - r_{ij}\right) H\left(r_{ij} - r_1\right) \exp\left(B_0 + B_1 r_{ij} + B_2 r_{ij}^2 + B_3 r_{ij}^3\right) \\ & + H\left(r_1 - r_{ij}\right) V_{ZBL}(r_{ij}), \end{aligned} \tag{2.30}$$

The parameters in Table 2.4 are splining coefficients used to link the pair potential to the

k	B_k
0	7.4122709384068 eV
1	-0.64180690713367 eV/Å
2	-2.6043547961722 eV/Å^2
3	0.6262539393123 eV/Å^3

Table 2.4: Values of the parameters in Equation 2.30 for the Fe-Fe interaction described by the Ackland 2004 potential [42].

ZBL potential, which is calculated by Ackland *et al.* [42]. In fact, it would be better to apply a fifth order exponential polynomial as shown in Equation 2.22.

2.1.3.2.2 Gao

A new Fe-He EAM potential was recently developed by F. Gao *et al.* [44] in combination with the Ackland 2004 [42] and the Aziz [37] potentials. The potential based on an "s-band model" shows an agreement with both *ab-initio* and the previous potential calculations.

The expression of the potential is very similar to the Ackland potential [42] and has the same form of the pair potential (Equation 2.25) and the many-body interaction function (Equation 2.27) with the parameters given in Tables 2.6 and 2.7 accordingly.

The total electron density is calculated in a different way to that of the Fe-Fe model. It

k	a_k(eV/Å^3)	r_k(Å)
1		1.0
2		2.05
3	−27.444805994228	2.2
4	15.738054058489	2.3
5	−2.2077118733936	2.4
6	−2.4989799053251	2.5
7	4.2099676494795	2.6
8	−0.77361294129713	2.7
9	0.80656414937789	2.8
10	−2.3194358924605	3.0
11	2.6577406128280	3.3
12	−1.0260416933564	3.7
13	0.35018615891957	4.2
14	−0.058531821042271	4.7
15	−0.0030458824556234	5.3

Table 2.5: Values of the parameters in Equation 2.30 for the Fe-Fe interaction described by the Ackland 2004 potential [42].

k	1	2	3	4	5	6	7
a_k(eV/Å^3)	−45.91636	35.55031	164.31987	−1.72746	0.10677	0.07372	0.03824
r_k(Å)	1.6155	1.6896	1.8017	2.0482	2.3816	3.5067	3.9028

Table 2.6: Parameters of the pair potential function in the many-body potential for the Fe-He interaction described by the Gao potential [44].

a_0^f(eV/Å)	a_1^f(eV/Å^4)	a_2^f(eV/Å^8)
0.22081	1.36751	3.38226

Table 2.7: Parameters of the many-body interaction function in the many-body potential for the Fe-He interaction described by the Gao potential [44].

is derived from the s-band model as follows:

$$\rho_i = \sum_j \Phi_{ij}(r_{ij}), \quad \Phi_{ij}(r_{ij}) = N_s r_{ij}^3 \exp\left(-2\xi_s r_{ij}\right), \tag{2.31}$$

where $\xi_s = 12.89363\text{Å}^{-1}$ - an average from the 1s and 4s Hartee-Fock orbitals for He and Fe and $N_s = 20.0\text{Å}$ - represents the s-electron density at the first nearest neighbour distance.

For the short range interaction, the repulsive part of the pair potential was connected to the ZBL universal function [43] and the final form of the interaction is:

$$V_{ij}^{Fe-He}(r_{ij}) = V_{ij}(r_{ij})F(r_{ij}) + V_{BZ}(r_{ij})\left[1 - F(r_{ij})\right], \tag{2.32}$$

where $F(r_{ij}) = 1/\left(1 + \exp\left(-b_f\left(r_{ij} - r_f\right)\right)\right)$ with $b_f = 10.0\text{Å}^{-1}$, $r_f = 0.25\text{Å}$.

2.1.3.2.3 Stoller

A recently developed potential for He-Fe interactions, which was introduced by Stoller's group [45], includes a three-body term to stabilize the interstitial He defect in the tetrahedral position in the Fe bcc system. This potential is tested and compared with the Gao potential. To describe the atomic interaction of the helium-vacancy clusters He_nV_m in the bcc Fe system, the Stoller potential is combined with the 1997 Ackland *et al.* potential [46] for the Fe-Fe interactions whilst Gao's uses the Ackland and Mendelev potential (AM-potential) for the Fe-Fe interactions [42]. Both of the potentials use the Aziz helium potential for the He-He interactions [37].

2.1.3.2.4 Voter-Chen

For the aluminium system, Voter and Chen's EAM potential [47] was used to perform the calculations. A universal function, scaling the cohesive energy of most metals, is taken here to fit the embedding function. In their model, the pair interaction $V(r_{ij})$ was taken to be a

Morse potential;

$$V(r_{ij}) = D_M(1 - \exp(-\alpha_M(r_{ij} - R_M)))^2 - D_M \tag{2.33}$$

where parameters D_M, R_M and α_M define depth, distance to the minimum and a measure of curvature near the minimum. The density function is taken as;

$$\rho_i = \sum_j \Phi_{ij}(r_{ij}) \tag{2.34}$$

where

$$\Phi_{ij}(r_{ij}) = r_{ij}^6(\exp(\beta r_{ij}) + 2^9 \exp(-2\beta r_{ij})) \tag{2.35}$$

where β is adjustable and 2^9 is a relative normalisation factor, and the embedding function $F(\rho_i(r_{ij}))$ (Equation 2.24) is fitted numerically from the Rose equation of the state [48]. To ensure continuity between the potential and first derivatives, a cut-off function is used during the fitting procedure. The parameters for the Al potential can be found in [47]. For our implementation tabulated values of the various functions were provided by A. Voter.

2.1.4 Boundary Conditions

Usually the atomic system under study is embedded in a larger system. In order for the simulation to progress boundary conditions are required. Usually these are applied on planes whose normals define the Cartesian axes.

2.1.4.1 Free Boundary Conditions

In an atomic system where particles are free to move, but confined due to strong interatomic potentials, free boundary conditions allow the edge atoms to relax according to the same rules as those internally. However, in this situation particles may be lost from the system.

2.1.4.2 Fixed Boundary Conditions

Fixing the boundary condition means that edge atoms are not allowed to move. It helps minimising the complexity of the simulation process, however, the boundary should be far enough away that this has no or negligible effect on the accuracy of the simulation. Fixing boundaries, is a common way to ensure process containment, such as when a large momentum is imparted and atomic drift is to be avoided. This is depicted schematically in Figure 2.2.

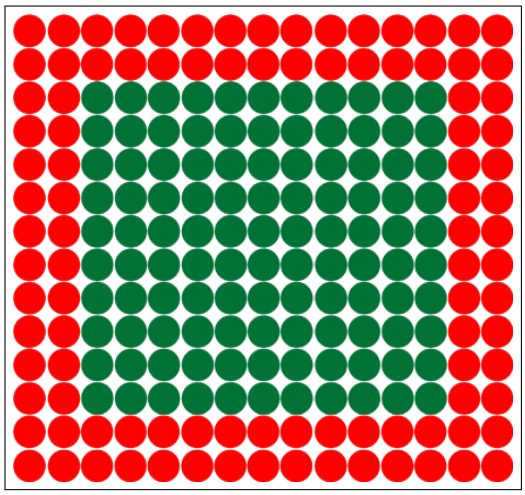

Figure 2.2: Schematic representation of fixed boundary conditions in 2D with two outside atom layers fixed (shown in red) and the rest of the atoms are allowed to move (shown in green).

2.1.4.3 Absorbing Boundary Conditions

In the case of radiation studies where a collision cascade reaches the boundary of the system, it is possible to set the kinetic energy of the arriving cascade particles and the boundary atoms to zero. This is the case of absorbing boundaries.

2.1.4.4 Periodic Boundary Conditions

An alternative to fixed boundaries are periodic boundary conditions (PBC). In this case the simulation cell is replicated in each direction forming an infinite lattice (see Figure 2.3). This helps simulating larger cells but only works well while the simulated event is contained in the simulation box. Figure 2.3 represents the main principle of PBC: a particle which goes

out of the primary cell through one side is brought back into the cell through the opposite site.

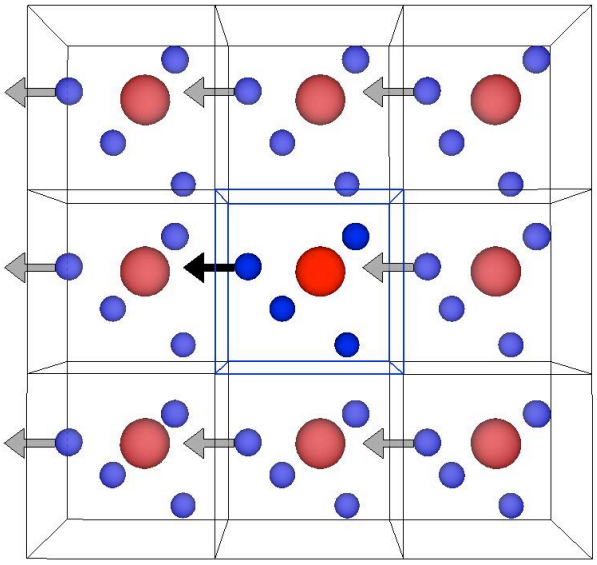

Figure 2.3: Schematic representation of periodic boundary conditions, where the centre cell (primary cell) is the simulated system and the cells around the primary cell (image cells) responsible for replicating the bulk system effect. The main principle: if a particle leaves the primary cell on one side, it must re-enter the cell on the opposite side.

These boundary conditions can be used in combination. In this thesis, the periodic boundaries conditions are applied in three dimensions.

2.1.5 System minimisation

The results from simulations strongly depend on the initial state. Thus at the beginning of a simulation it is necessary to make sure that the atoms are located at a global or at least a local potential energy minimum, which is usually achieved by optimising the system's structure through the force field generated by the interatomic potentials. To minimise the system, the minimisation method and required tolerance are the two main inputs. In this work, two techniques were used for system minimisation: the conjugate gradient method and L-BFGS-B.

2.1.5.1 Conjugate Gradient

The conjugate gradient (CG) method developed by Fletcher and Reeves [49] is an iterative method with a high rate of convergence to find the minimum of a non-linear function $f(\mathbf{x})$ if its gradient vector $g(\mathbf{x})$ can be calculated at any point $\mathbf{x}$. This technique is used when the lattice configuration was already close to a minimum energy configuration.

The first step is to calculate the initial gradient $g(\mathbf{x}_n)$ ($g(\mathbf{x}_n) = -\nabla f(\mathbf{x}_n)$) which is taken to be the initial search direction $\mathbf{s}_0$ from point $\mathbf{x}_0$, $\mathbf{s}_0 = g(\mathbf{x}_0)$.

Then start the iterations

Step 1. Calculate α satisfying:

$$\frac{\mathrm{d}f(\mathbf{x}_n + \alpha \mathbf{s}_n)}{\mathrm{d}\alpha} = 0. \tag{2.36}$$

Step 2. Compute a new point $\mathbf{x}_{n+1}$:

$$\mathbf{x}_{n+1} = \mathbf{x}_n + \alpha_n \mathbf{s}_n. \tag{2.37}$$

Step 3. Compute the new gradient $g(\mathbf{x}_{n+1})$:

$$g(\mathbf{x}_{n+1}) = -\nabla f(\mathbf{x}_{n+1}). \tag{2.38}$$

Step 4. Compute the parameter β:

$$\beta_n = \frac{\|g(\mathbf{x}_{n+1})\|^2 - g(\mathbf{x}_{n+1})^T g(\mathbf{x}_n)}{\|g(\mathbf{x}_n)\|^2}. \tag{2.39}$$

Step 5. Find the new direction $\mathbf{s}_{n+1}$:

$$\mathbf{s}_{n+1} = g(\mathbf{x}_{n+1}) + \beta_n \mathbf{s}_n. \tag{2.40}$$

Step 6. Check the convergence by checking if the gradient is less than a tolerance ε to see

if a minimum has been reached,

$$g(\mathbf{x}_{n+1}) \leq \varepsilon. \tag{2.41}$$

If the minimum is attained, terminate the iterations, if not - go to **Step 1**.

2.1.5.2 L-BFGS-B

The Broyden-Fletcher-Goldfarb-Shanno (BFGS) optimization algorithm is to approximate the Hessian matrix by repeating using gradient evaluations.

The method starts with an initial guess $\mathbf{x}_0$ and the initial approximation of the Hessian H_0:

$$H_0\mathbf{s}_0 = -\nabla f(\mathbf{x}_0), \tag{2.42}$$

where f is the function being minimised.

Then iterations to approximate the Hessian H_n are given through:

- **Step 1 - new direction** - find a new direction $\mathbf{s}_n$ by solving $H_n\mathbf{s}_n = -\nabla f(\mathbf{x}_n)$,
- **Step 2 - line search** - find a reasonable step size α_n (as in Equation 2.36) and get $\mathbf{x}_{n+1} = \mathbf{x}_n + \alpha_n\mathbf{s}_n$,
- **Step 3 - new gradient** - compute the new gradient $g(\mathbf{x}_{n+1})$:

$$g(\mathbf{x}_{n+1}) = -\nabla f(\mathbf{x}_{n+1}). \tag{2.43}$$

- **Step 4 - Hessian approximation** - update the Hessian approximation:

$$H_{n+1} = H_n - \frac{(\nabla g(\mathbf{x}_{n+1}) - \nabla g(\mathbf{x}_n))\,(\nabla g(\mathbf{x}_{n+1}) - \nabla g(\mathbf{x}_n))^T}{(\nabla g(\mathbf{x}_{n+1}) - \nabla g(\mathbf{x}_n))^T\,\alpha_n\mathbf{s}_n} - \frac{H_n\,(\alpha_n\mathbf{s}_n)\,(\alpha_n\mathbf{s}_n)^T\,H_n}{(\alpha_n\mathbf{s}_n)^T\,H_n\,(\alpha_n\mathbf{s}_n)}. \tag{2.44}$$

- **Step 5 - repeat** - if the convergence tolerance has not been achieved, go to **Step 1**.

In this work, the improved BFGS method (L-BFGS-B) [50, 51] is applied. It uses only a couple of vectors to represent the inverse Hessian matrix to improve the efficiency. The L-BFGS-B method is implemented from the open source library SciPy 0.12.0 for the Python programming language (http://www.scipy.org/).

2.1.6 System Thermalisation

In many cases, a thermostat is required to maintain the temperature of the system at the desired temperature. When studying radiation damage in materials, this will be the case when an excess energy is introduced in the system by collision cascades. Then the energy of the system will increase causing the increase of temperature. Ideally, if a large enough system is chosen, the energy from these impacts would dissipate throughout the system. However, for small systems, thermal layers may be needed to remove the excess energy and to bring the system to the required temperature.

To control a system's temperature, so called thermostat algorithms are used. The actual temperature can be calculated by

$$T = \frac{2}{3}\frac{E_K}{Nk_B}, \tag{2.45}$$

where E_K is the total kinetic energy, N is the number of moving atoms and k_B is Boltzmann constant.

There are quite a few thermostats and all of them have their advantages and disadvantages. One of the most popular is the Nosé-Hoover thermostat [52]. It governs the atoms' velocities by introducing a friction term coefficient in the equations of motion, which depends on the actual and target kinetic energies. The coefficient is fairly easy to calculate and the method can give a good canonical ensemble of the atoms. One of the drawbacks is that it usually takes longer to reach the required temperature due to big oscillations.

Another popular thermostat follows Langevin dynamics [53]. In this case a small damping constant is used in a modification of the Newton's equations of motion proportional to the

velocity, so that the actual temperature matches the target temperature.

In this work, the Berendsen thermostat [54] was used to control the temperature of the systems by scaling the atoms' velocities at each step in a way that the change in temperature with respect to time is proportional to the difference between the actual temperature T and the desired temperature T_0,

$$\frac{dT(t)}{dt} = 2\gamma \left(T_0 - T(t)\right), \tag{2.46}$$

where $T(t)$ is the temperature of the system at time t and where γ is a decay constant, which controls the correction of the temperature.

It is proven that the velocity scaling factor per time step Δt can be made exactly equal to $2\gamma \left(T_0 - T(t)\right)$ as follows:

$$\lambda = \sqrt{1 + \frac{\Delta T}{\tau_T}(\frac{T_0}{T} - 1)}, \tag{2.47}$$

where τ_T is a time constant, which is equal to $\frac{1}{2\gamma}$. Although a correct canonical ensemble generated by this thermostat cannot be achieved for a small system, in practise all thermostats generate an approximate canonical ensemble for big systems.

2.2 Long Time Scale Dynamics

2.2.1 Introduction

While MD is an extremely powerful method for investigating many processes on an atomic level, one of the major drawbacks it has is that simulations are generally limited to the order of nanoseconds to microseconds. However diffusion processes occur on a much longer time scale and are therefore out of reach of MD simulations.

In order to overcome this problem, we apply the on-the-fly Kinetic Monte Carlo (otf-KMC) method, which was initially introduced by Henkelman [55]. This method differs from the traditional KMC simulation in the way that all the transitions that can occur in the system are not known before the simulation starts, but are calculated on-the-fly at the

beginning of each KMC step. By this method, a simulation could be started from various random system configurations, but this does not guarantee that all possible transitions will be found during each step. When a list of transition events is generated, rates for each transition are calculated from transition state theory, then a rate list is made and next the system is evolved into a new state using the appropriate transition probability.

Point Defects

One way to quantify damage in a crystal lattice is to look for point defects. Basically they can be classified into two types: an interstitial (an atom positioned away from a lattice site) and a vacancy (an unoccupied lattice site). In this work, interstitials are visualized as spheres and vacancies as cubes (see Figure 2.4).

(a) (b)

Figure 2.4: A visual representation of the main types of defects: (a) - He interstitial, (b) - Fe vacancy

The way to identify defects in the system is to compare the initial atom positions (reference lattice), with the current atom positions (input lattice). All the atoms that are not located within a certain radius R_{vac}, named vacancy radius, are identified as defects, e.g. A vacancy is simply a lattice site that should contain an atom within R_{vac} but does not, while an interstitial is an atom that does not occupy a normal lattice site within R_{vac}.

Kinetic Monte Carlo

As an input KMC requires a list of all possible transitions the system can undergo along with the associated energies. The algorithm can be expressed as an iterative procedure as follows:

1. Set the initial time (usually t = 0),

2. Make a list of rates in the system r_i regarding the possible events and sum them as

$R = \sum_{j=1}^{N} r_j$,

3. Generate a random number P between 0 and R,

4. Cumulatively step through all events until P is exceeded,

5. The transition is selected with respect to the current event and the system evolves into a new state,

6. The time increment δt during the step is given by $\delta t = -\frac{\ln u}{R}$, where u is a random number between 0 and 1,

7. Return to step 2.

Pre-definition of all possible events is sometimes feasible if simulating a simple crystal structures. However, it becomes a problem when dealing with more complex systems. Henkelman and Jónsson [55] attempted to overcome this problem with their on-the-fly kinetic Monte Carlo (otfKMC) method to carry out long time scale dynamics simulations within the harmonic transition state theory (hTST) approximation to study $Al\,(100)$ crystal growth. They suggested to characterise a system by its local energy minimum, do multiple saddle searches on the fly and calculate the rate of each transition using harmonic transition theory, where the clock was advanced with a chosen transition.

The rate of each transition is calculated using the Arrhenius equation:

$$r = \tau \exp\left(-\Delta E / k_B T\right), \tag{2.48}$$

where ΔE is the energy barrier of the i'th transition, k_B - Boltzmann's constant, T - temperature of the system and τ is the transition prefactor. For example, 0.3 eV implies a hop time of 110 ps at 500 K with a prefactor of 10^{13} and 2 eV implies 0.46 years for a hop at 500 K with a prefactor of 10^{13}, more examples are shown in Chapter 3.

As can be seen in Equation 2.48, transition rates mainly depend on the energy barrier ΔE and the prefactor τ. Further, ΔE is calculated by examining the initial minimum and

saddle states of the transition. Therefore it is crucial to determine the saddle state accurately since it connects two minima via the minimum energy pathway (MEP) and determines how likely a transition will be picked to advance the system. Various methods are introduced to find the saddle points. These are known as transition search methods.

2.2.2 Saddle Finding Methods

As mentioned earlier, saddle point finding methods are used in the otf-KMC scheme to find possible transitions. The main feature is that they require only the initial configuration of the system in order to return local saddle points. All these techniques work in a similar way by locating and following the lowest curvature mode, along which the saddle point is a maximum.

2.2.2.1 Dimer Method

The Dimer method developed by Henkelman and Jónsson [56] represents a system's state as two images (this pair of images is referred as a "dimer") having almost the same set of coordinates with small fixed displacement. It can be thought of as a two step algorithm, where the first step is the dimer's movement and the calculation of the acting forces and energies on it (Figure 2.5a). The second step is the rotation of the dimer towards the minimum energy configuration (Figure 2.5b). The advantage of the Dimer method is the usage of only first derivatives of the potential energy since the inverse Hessian is computationally expensive to calculate.

In Figure 2.5a R represents the coordinate of the system's midpoint (state) in 3N dimensional space. Points R_1 and R_2 are the pair images separated from R by ΔR and are orientated in the direction of a unit vector $\hat{\mathbf{N}}$. Initially and every time when the dimer is moved to a new location, the corresponding energies (E_1, E_2) and forces ($\mathbf{F_1}$, $\mathbf{F_2}$) at (R_1, R_2) are evaluated. The energy of the dimer is simply a sum of energies of the images $E = E_1 + E_2$, where the force and the energy at the midpoint R, $\mathbf{F}_R$ and E_0, are calculated from the two

images (Equation 2.49) as follows:

$$\begin{aligned} \mathbf{F_R} &= (\mathbf{F_1} - \mathbf{F_2})/2, \\ E_0 &= \frac{E}{2} + \frac{\Delta R}{4}(\mathbf{F_1} - \mathbf{F_2}) \cdot \hat{\mathbf{N}}. \end{aligned} \tag{2.49}$$

The dimer's rotation towards the minimum energy configuration is based on the idea, that minimising the dimer's energy E is equal to finding the lowest curvature mode at R, estimated using Equation 2.50. This is done by rotating the dimer along the rotational force $\mathbf{F}^{\perp} = \mathbf{F_1^{\perp}} - \mathbf{F_2^{\perp}}$, where $\mathbf{F_i^{\perp}} \equiv \mathbf{F_i} - (\mathbf{F_i} \cdot \hat{\mathbf{N}}) \cdot \hat{\mathbf{N}}, i = 1, 2$, until the tangential force is zero.

$$C = \frac{(\mathbf{F_2} - \mathbf{F_1}) \cdot \hat{\mathbf{N}}}{2\Delta R} = \frac{E - 2E_0}{(\Delta R)^2}. \tag{2.50}$$

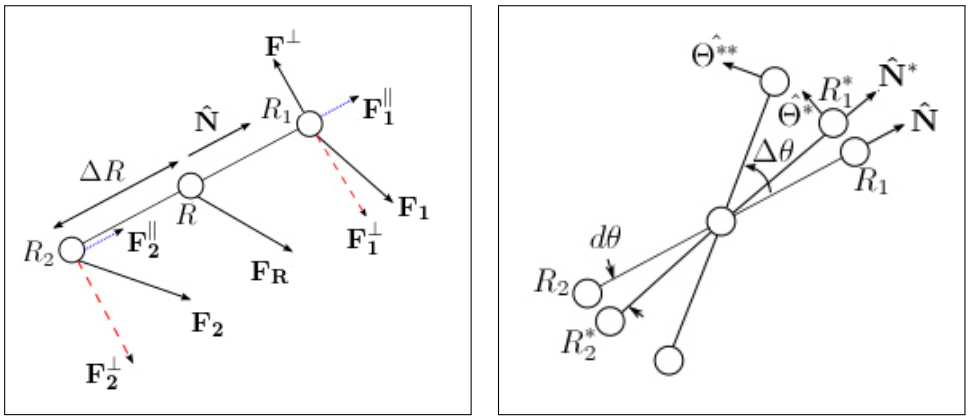

(a) (b)

Figure 2.5: The Dimer method as in [56]. (a) - the definitions of the dimer's midpoint, image points and the acting component and rotational forces on them, (b) - the definitions of the quantities used during the rotation of the dimer.

Figure 2.5b shows the basic steps of the dimer's rotation. A new unit vector $\hat{\mathbf{\Theta}}$, perpendicular to $\hat{\mathbf{N}}$ and parallel to $\mathbf{F}^{\perp}$, is defined to form an orthonormal basis which spans the rotation plane. At first, the dimer is rotated about a small angle $d\theta$ (see Figure 2.5b), then using the orthonormal basis new image points are calculated (Equation 2.51) and the acting

forces $\mathbf{F_1^*}$, $\mathbf{F_2^*}$, $\mathbf{F^*} = \mathbf{F_1^*} - \mathbf{F_2^*}$ are estimated.

$$\begin{aligned} \mathbf{R}_1^* &= \mathbf{R} + \left(\hat{\mathbf{N}} \cos d\theta + \hat{\mathbf{\Theta}} \sin d\theta\right) \Delta R, \\ \mathbf{R}_2^* &= \mathbf{R}_1^* - 2\Delta R \hat{\mathbf{N}}. \end{aligned} \tag{2.51}$$

The finite difference approximation of the derivative of the rotational force is given in Equation 2.52, which is to be minimised.

$$F' \approx \left| \frac{\mathbf{F}^* \cdot \hat{\mathbf{\Theta}}^* - \mathbf{F} \cdot \hat{\mathbf{\Theta}}}{d\theta} \right|_{\theta = d\theta/2}. \tag{2.52}$$

In this work the harmonic approximation of the rotational force $F = A \sin\left[2(\theta - \theta_0)\right]$, where A, θ, θ_0 are fitting constants and its derivative $F' = 2A \cos\left[2(\theta - \theta_0)\right]$ are used to approximate the rotation angle $\Delta\theta$ as follows:

$$\Delta\theta = -\frac{1}{2} \arctan \frac{2F_0}{F_0{}'}, \tag{2.53}$$

where F_0 and $F_0{}'$ are values of F and F' evaluated at $\theta = 0$.

Then $\Delta\theta$ is used to minimise the dimer's energy with the CG method using the modified Newton method [56] as the line search.

After the minimisation by rotation, the dimer will be oriented along the local lowest curvature mode and this is followed by the dimer's translation. Depending on the curvature value C, calculated using Equation 2.50, two schemes are used. First, when the curvature value is positive, the dimer is allowed to move out of that region by relatively big steps. Second, when the curvature has a negative value, the dimer is getting closer to the saddle point and the saddle point is approached by smaller steps. The two cases can be expressed as follows:

$$\mathbf{F}_{trans} = \begin{cases} -\mathbf{F}^{\parallel}, & C > 0, \\ \mathbf{F} - 2\mathbf{F}^{\parallel}, & C < 0, \end{cases} \tag{2.54}$$

where $\mathbf{F}$ is the real force acting on the dimer, $\mathbf{F}^{\parallel}$ - the component of the force parallel to the $\hat{\mathbf{N}}$ and given by: $\mathbf{F}^{\parallel} = \mathbf{F}_{\mathbf{1}}^{\parallel} + \mathbf{F}_{\mathbf{2}}^{\parallel}$.

In the $C < 0$ region, the modified force is equivalent to converting the saddle point to a local minimum and in this region the lowest curvature direction is calculated from the lowest eigenvalue of the Hessian via the Lanczos method, followed by a CG minimisation.

2.2.2.2 Activation-Relaxation Technique (ART)

The Activation-Relaxation Technique (ART) was developed by Barkema and Mousseau [57, 58]. The ART algorithm requires only an initial state and consists of three main steps:

Escaping from a local minimum: this is done by an initial random displacement from the minimum. The displacement could include one or more atoms, however, it will be more efficient when atoms displaced are within the area surrounding the defect. The direction of the displacement is chosen to be along the force resulting from the displacement, which is done by checking that the increment in force components parallel to the displacement is getting very small or the ratio between the parallel and perpendicular force components is less than a given value. In this work a single point $\mathbf{R}$ is considered in 3N space and displaced to $\mathbf{R}^*$ using a random displacement vector $\vec{N}$ as shown in Figure 2.6.

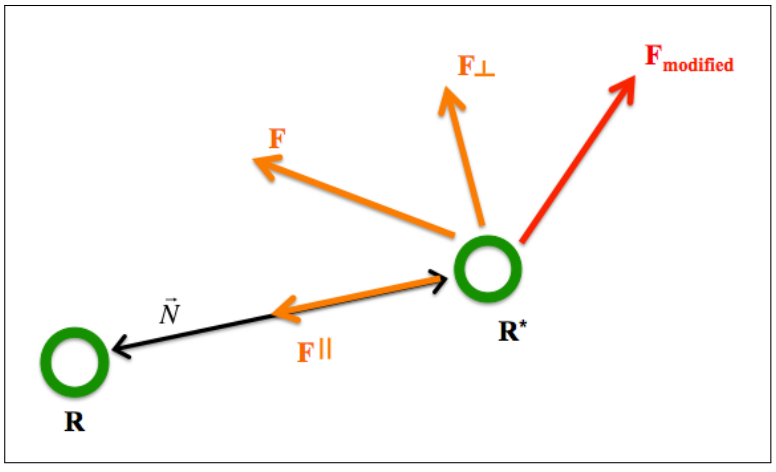

Figure 2.6: This figure shows the components of force resulting from a random displacement from point $\mathbf{R}$ to point $\mathbf{R}^*$ using a random displacement vector $\vec{\mathbf{N}}$ used in the ART method to escape from a basin. The modified force vector is described below.

Moving to an adjacent saddle: the next step is to introduce a modified force vector:

$$\mathbf{F}_{modified} = \mathbf{F} - (1 + \alpha)\mathbf{F}^{\parallel} \tag{2.55}$$

where the total force $\mathbf{F}$ can be decomposed into parallel and perpendicular forces. α is a control parameter usually set to be 0.15/displacement. After the modified force is determined the point $\mathbf{R}^*$ is moved to $\mathbf{R}^{**}$ with a step size δt:

$$\mathbf{R}^{**} = \mathbf{R}^* + \mathbf{F}_{modified}\delta t \tag{2.56}$$

The direction of the modified force is then followed until it finds a saddle point. Changing the sign of the component of the force which is parallel to $\vec{\mathbf{N}}$ is considered to be an indication of crossing a saddle point.

Minimising to new minimum: once the saddle point is found, a minimisation technique such as conjugate gradient can be used to bring this saddle to a new minimum on the other side of the hill. To avoid the convergence to the original minimum it is usual to move slightly past the saddle point before minimisation.

2.2.2.3 Relaxation and Translation Method

The relaxation and translation (RAT) method was developed by Vernon [28] (see Figure 2.7). The idea behind it was that the ART method gave lots of transition duplicates for the calculations and thus larger number of searches would have to be done before all possible transitions had been explored.

Unlike the ART method, in the RAT method, the vector $\mathbf{N_i}$ is constructed by tethering the current position $\mathbf{R_i}$ to the previous historical step $\mathbf{R_{i-1}}$. Similarly to the ART method, the force acting on the search point is decomposed into perpendicular and horizontal forces and the search point is relaxed along the perpendicular vectors to $\mathbf{N_i}$. There are two main steps involved in RAT method:

In the first part, after an initial displacement or translation step, force minimisation is applied. $\mathbf{R'_i}$ is relaxed along the direction $\mathbf{F_{\perp,j}}$ which is the perpendicular force to $\overrightarrow{\mathbf{N'_i}}$ and moved to $\mathbf{R_i}$, as shown in Figure 2.7, with a variable step size depending on force change, which is given by:

$$Stepsize_{j+1} = \begin{cases} Stepsize_j + 20\% Stepsize_j, & ratio < 1.2, \\ Stepsize_j - 50\% Stepsize_j, & ratio > 1.2, \end{cases} \tag{2.57}$$

$$ratio = \frac{\|\mathbf{F_{\perp,j+1}} - \mathbf{F_{\perp,j}}\|}{\|\mathbf{F_{\perp,j}}\|} \tag{2.58}$$

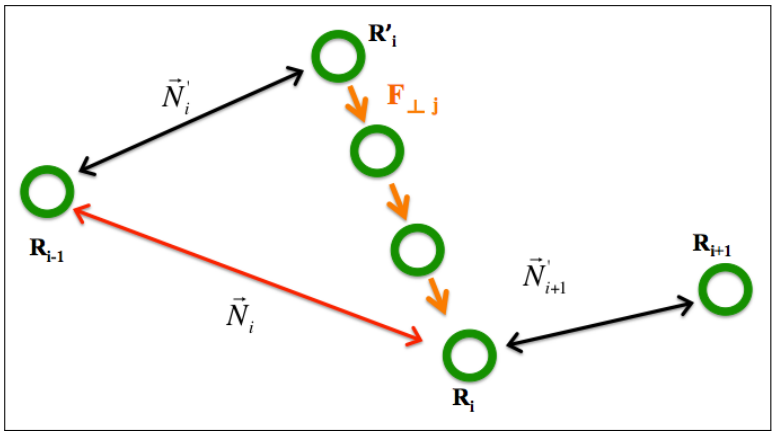

Figure 2.7: Schematic illustration of force minimisation in the RAT method. Orange arrows indicate the direction of the perpendicular force component. The initial displacement vector $\mathbf{N'_i}$ tethers the current position $\mathbf{R'_i}$ to previous step $\mathbf{R_{i-1}}$, while the relaxed displacement vector $\mathbf{N_i}$ tethers the relaxed position $\mathbf{R_i}$ to $\mathbf{R_{i-1}}$.

After the relaxation step, the point $\mathbf{R'_i}$ is relaxed to $\mathbf{R_i}$. Then the new normalised translation vector can be constructed by:

$$\mathbf{N'_{i+1}} = \frac{\mathbf{N'_i} + \mathbf{N_i}}{|\mathbf{N'_i} + \mathbf{N_i}|} \tag{2.59}$$

where the vector $\mathbf{N}_0$ is a random unit vector, which for all the other steps $\mathbf{N}_i, i \geq 1$ is constructed in this way.

The search point is then moved along this new direction $\mathbf{N'_{i+1}}$. The relaxation and

translation procedure is replicated until the dot product of the parallel force component and the displacement vector turns positive. The saddle point will then be crossed.

2.2.2.4 Minimum Mode Following Algorithm

The basic idea to find the saddle point with only the knowledge of the initial state is to climb up from the initial minimum to the saddle using the vector of the lowest eigenvalue (minimum mode) of the Hessian matrix when in a region close to a saddle. The biggest drawback is the computationally expensive effort of finding the full Hessian matrix in order to solve the eigenvalue problem.

A Minimum Mode Following Algorithm (MMFA) has been developed by A. Pederson *et al.* [59] in 2011. The MMFA could be used to climb up from initial point to the saddle without the need of constructing the Hessian matrix. This is done by introducing the effective force:

$$\mathbf{F}^{eff} = \mathbf{F} - 2\left(\mathbf{F} \cdot \mathbf{v}_{min}\right)\mathbf{v}_{min}, \tag{2.60}$$

where $\mathbf{F}^{eff}$ is the effective force driving the system to a saddle point, $\mathbf{F}$ is the actual force and $\mathbf{v}_{min}$ is the eigenvector corresponding to the lowest eigenvalue. With the $\mathbf{F}^{eff}$ so defined, the rank 1 saddles become local minima and local optimisation algorithms can be used to found them.

$\mathbf{v}_{min}$ can be found by constructing the Hessian which includes the second derivatives of the potential energy, diagonalising the matrix and find the lowest eigenvalue. However, since to know the eigenvalues for the full Hessian matrix is wasteful, this construction can be omitted from this process and the lowest eigenvalue only can be calculated during the simulation. For instance, a similar technique used in the dimer method can be used here as the dimer after rotation is along the minimum mode direction. Another approach which has been used to obtain the lowest eigenvalue is using the Lanczos algorithm [60] without the need of constructing the Hessian matrix.

For this work, the dimer method is used to approach the saddle and then the Lanczos

algorithm is used for saddle convergence. The Lanczos algorithm is used to convert the Hessian into a tridiagonal matrix where the Linear Algebra Package (LAPACK) is used to find the lowest eigenvalue of the updated matrix. This reduces the computational time spent by minimisation and finding the Minimum Energy pathway (MEP) using the NEB technique given in Section 2.2.3.1.

2.2.2.5 Lanczos Algorithm

The Lanczos algorithm is a very powerful technique to save computational time while calculating eigenvalues and eigenvectors of a symmetric matrix. The algorithm is an iterative procedure [60] and operates on the idea of converting a symmetric matrix $\mathbf{A}$ to a tridiagonal symmetric matrix as follows:

Listing 2.1: Lanczos algorithm

```
1 β_1 = 0; v_0 = 0; v_1 = normalised random vector.
2 for i in range(1, m)
3           w_i = A v_i
4           α_i = w_i · v_i
5           w_i = w_i − α_i v_i − β_i v_{i−1}
6           β_{i+1} = ||w_i||
7           v_{i+1} = w_i / β_{i+1}
8 end;
```

where $\mathbf{A}$ is a symmetric matrix (in our case it is the Hessian at a certain phase space point of the system), α_i and β_i are the elements of the tridiagonal result matrix (Equation 2.61),

m - the size of the symmetric matrix and $\mathbf{v}_i$ are the orthonormal Lanczos basis vectors.

$$T = \begin{bmatrix} \alpha_0 & \beta_1 & 0 & \cdots & 0 \\ \beta_1 & \alpha_1 & \beta_2 & \cdots & 0 \\ 0 & \beta_2 & \alpha_2 & \cdots & 0 \\ 0 & \ddots & \ddots & \vdots & 0 \\ 0 & 0 & \beta_{n-2} & \alpha_{n-2} & \beta_{n-1} \\ 0 & 0 & 0 & \beta_{n-1} & \alpha_{n-1} \end{bmatrix} \tag{2.61}$$

The effectiveness of the Lanczos method also comes from the approximation of $\mathbf{A}\mathbf{v}_i$ by the difference in the Taylor expansion forces around the phase space point $\mathbf{x}+\delta\mathbf{v}_i$ with error either $O(\delta^2)$ (Equation 2.62) or $O(\delta^3)$ (Equation 2.63) as follows:

$$\mathbf{A}\mathbf{v}_i = -\frac{\mathbf{f}\left(\mathbf{x}+\delta\mathbf{v}_i\right) - \mathbf{f}\left(\mathbf{x}\right)}{\delta} + O\left(\delta^2\right) \tag{2.62}$$

$$\mathbf{A}\mathbf{v}_i = -\frac{\mathbf{f}\left(\mathbf{x}+\delta\mathbf{v}_i\right) - \mathbf{f}\left(\mathbf{x}-\delta\mathbf{v}_i\right)}{2\delta} + O\left(\delta^3\right) \tag{2.63}$$

where $\delta \ll 1$.

It is known, that due to the computational errors, the exact orthogonality of the Lanczos basis is not exactly preserved [61]. To deal with this problem, the least squares method (LSM) is used as follows:

$$\mathbf{v}_i = \mathbf{v}_i - \mathbf{L}_i\mathbf{s}_i, \tag{2.64}$$

where $\mathbf{L}_i$ is an orthonormal Lanczos basis consisting of $i-1$ Lanczos vectors $\mathbf{v}_j$ (j $= \overline{1, i-1}$) and $\mathbf{s}_i$ is the least squares method's (LSM) solution of the problem: $\mathbf{L}_i\mathbf{s}_i = \mathbf{v}_i$. Equation 2.64 removes the non-orthogonal error from the Lanczos vector.

Empirical tests showed that the orthogonal correction by the LSM is sufficient while the number of the Lanczos basis vectors is lower than 50. Otherwise, the LSM method contribution to the overall computational costs per Lanczos iteration increases significantly and

the difference between time taken by the Lanczos method compared to explicit calculations of the eigenvalues and eigenvectors of the Hessian matrix is small.

The iterative Lanzcos procedure is stopped when the desired convergence of the lowest or other (specified by the user) eigenvalue (calculated using the QR method which is implemented from the Linear Algebra PACKage (LAPACK) library and is special designed for estimating eigenvalues/eigenvectors of a tridiagonal symmetric matrix, to calculate the lowest eigenvalue and corresponding eigenvector of the tridiagonal symmetric matrix) is reached by checking if the relative change of the eigenvalue is less than the specified value. The default tolerance used in the simulations is 0.01, since the tighter tolerance did not have a significant impact on the results.

2.2.3 Barrier Calculating

The above techniques determine the height of the saddle and a path to the next local minimisation but they may only provide a loose estimate of the actual energy barrier associated with the saddle. In fact, due to the way they work (searching up hill from a minimum) they will often overestimate the height of the saddle point unless very small steps are taken. Thus a different set of techniques are required to accurately determine the energy barrier associated with a transition in a reasonable computing time. These techniques require both the initial and final configurations of the transition to calculate the barrier and find the Minimum Energy Pathway (MEP) more accurately.

2.2.3.1 Nudged Elastic Band Method

The Nudged Elastic Band Method (NEB) is a way to find the minimum energy pathway between the initial and final system configurations (images). This is done by initially creating a chain of evenly separated intermediate images ($\mathbf{R_1}, \mathbf{R_2}, \cdots, \mathbf{R_m}$) and calculating acting forces on them as shown in Figure 2.8. Spring interactions between neighbouring images are added, thus imitating an elastic band and ensuring the continuity of the path. To prevent

both the spring and the true force from effecting the convergence to the MEP, only the perpendicular component of the true force and the tangential component of the spring force are considered. The steps of implementation of the NEB method are summarised below:

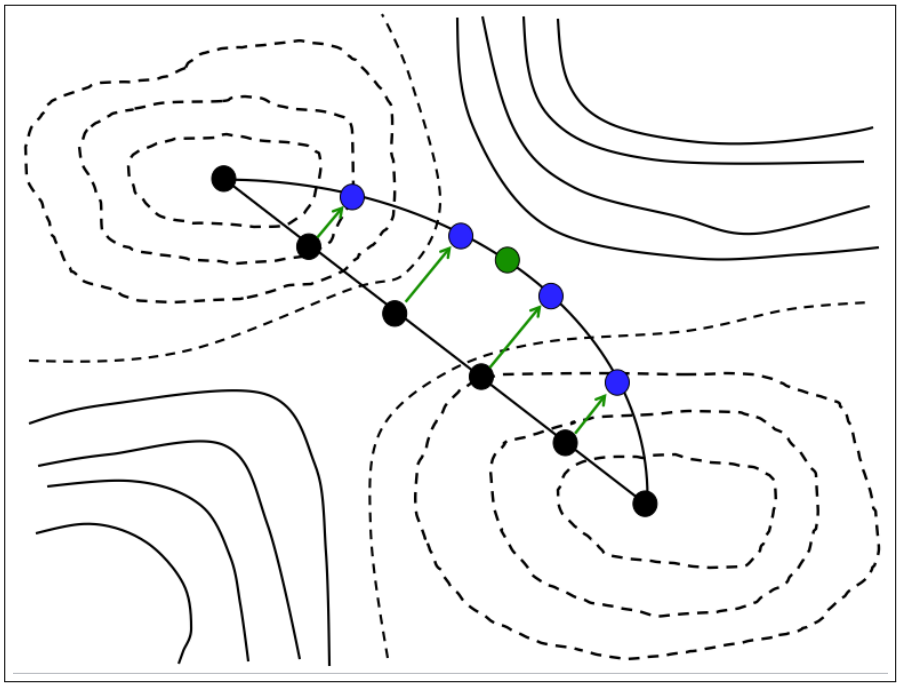

Figure 2.8: Schematic representation of the NEB method; where the black points represent the initial NEB images and the blue points are for the final NEB images joined by the MEP. Acting forces on images are shown as green arrows. The green point depicts the saddle point.

In this work an improved tangent estimation is used, which was suggested by G. Henkelman and H. Jónsson [30]. They changed the original estimation by using different tangent definitions according to the energies of the nearby images, thus eliminating some cases, when the method did not converge to the MEP. The tangent to the path τ_i is given by

$$\tau_i = \begin{cases} \mathbf{R}_{i+1} - \mathbf{R}_i & \text{if} \quad E_{i+1} > E_i > E_{i-1}, \\ \mathbf{R}_i - \mathbf{R}_{i-1} & \text{if} \quad E_{i+1} < E_i < E_{i-1}, \\ (\mathbf{R}_{i+1} - \mathbf{R}_i)\Delta E_i^{max} + (\mathbf{R}_i - \mathbf{R}_{i-1})\Delta E_i^{min} & \text{if} \quad E_i < E_{i-1} < E_{i+1}, \\ (\mathbf{R}_{i+1} - \mathbf{R}_i)\Delta E_i^{min} + (\mathbf{R}_i - \mathbf{R}_{i-1})\Delta E_i^{max} & \text{if} \quad E_i > E_{i-1} > E_{i+1}, \end{cases} \tag{2.65}$$

where $\mathbf{R}_i$ represents atoms' positions of an image i, and $\Delta E_i^{max} = \max\left(|E_{i+1} - E_i|, |E_{i-1} - E_i|\right)$,

$\Delta E_i^{min} = \min\left(|E_{i+1} - E_i|, |E_{i-1} - E_i|\right)$. The NEB method defines the force acting on image i as:

$$\mathbf{F}_i = \mathbf{F}_i^S + \mathbf{F}_i^P, \tag{2.66}$$

where $\mathbf{F}_i^P$ is the projection of the true force acting on image i perpendicular to the tangent vector, and $\mathbf{F}_i^S$ is the spring force parallel to the unit tangent vector $\hat{\tau}_i$, given by:

$$\mathbf{F}_i^S = k\left(|\mathbf{R}_{i+1} - \mathbf{R}_i| - |\mathbf{R}_i - \mathbf{R}_{i-1}|\right)\hat{\tau}_i, \tag{2.67}$$

where k is a spring constant. Once all the forces have been calculated the images are relaxed simultaneously by translating the m image points in $3N$ space to one point in $3Nm$ space. In this way the band moves iteratively towards the MEP.

After the tangent vector and acting force evaluation for each image have been determined, minimisation is carried out through simultaneous relaxation of each image. The saddle point is interpolated from the force band images.

A good improvement of the NEB is the climbing image method [62] which is implemented by movement of the image with the highest energy which can be identified after some iterations of the original NEB perpendicularly to the band. This will result in images converging to the MEP and the climbing image to the saddle point which will escape the interpolation step by converging directly to the saddle point. The way is every few relaxation steps, the force of the highest energy image is modified according to Equation 2.68, thus removing the spring force and only the real force is reflected parallel to the tangent vector.

$$\mathbf{F}_{i_{max}} = \mathbf{F}_{i_{max}}^{real} - 2\,\mathbf{F}_{i_{max}}\big|_{\parallel \tau_{i_{max}}}. \tag{2.68}$$

2.2.3.2 String Method

The NEB method uses a parameter, the spring constant k. If k is chosen too small, the elastic band may be a poor description of the MEP, while if it is chosen too big, the method

will converge only slowly and will require a lot of force calculations. The string method [63, 64] avoids this issue by constraining the distances between images.

Similarly to the NEB method, the string method also starts with given initial and final states and returns the saddle point and MEP. For any image in the potential field, it would "fall" into the local minimum due to the potential force if there were no other restraints. The NEB method assume the images are linked with elastic bands, the artificial spring force along the path prevent the images from falling into the local minimum at the ends. For the string method, this is done by enforcing a particular parameterisation. The string method can also be viewed as the inextensible limit $k \to \infty$ of the elastic band method, i.e. replace the elastic bands by strings in the elastic band method.

In each iteration of the string method, there are two main steps: an evolution step and a reparameterisation step (interpolation step). The evolution step guides the string toward the MEP, and the reparameterisation step redistributes the images along the string after each evolution step. A schematic illustration is shown in Figure 2.9.

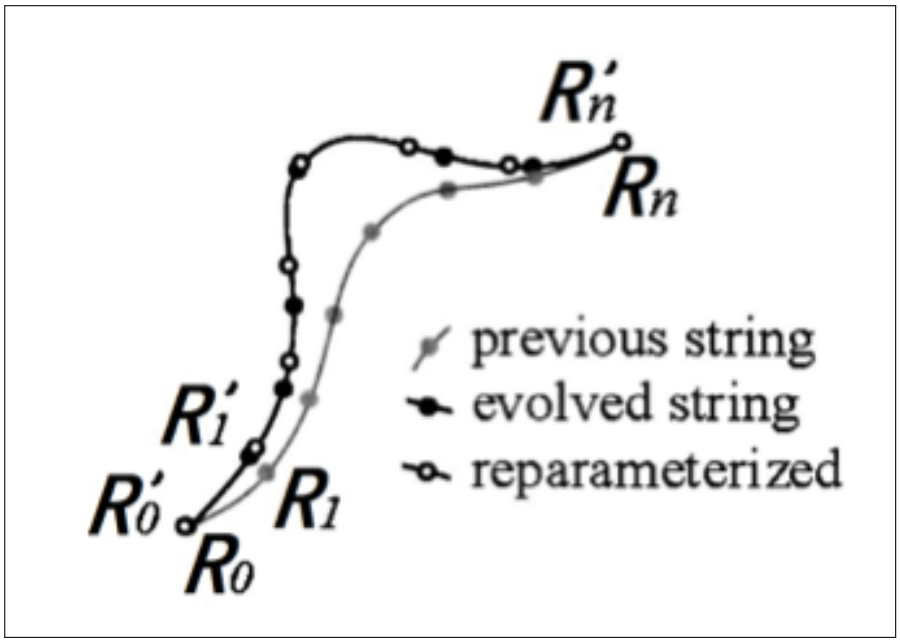

Figure 2.9: Schematic illustration of one iteration of the string method showing the initial string, the evolved string and the evolved string after reparameterisation. Figure taken from [64].

In the evolution step, the total force acting on the image is given by

$$\mathbf{F}_i = \mathbf{F}_i^P + \lambda_i \hat{\tau}_\mathbf{i}. \tag{2.69}$$

where $\lambda_i \hat{\tau}_\mathbf{i}$ is a Lagrange multiplier term, which is added to enforce the particular parametrisation that we have chosen. Together with Equation 2.65, one can get the evolved string.

Then for the interpolation step, one can choose parametrisation by equal arc length or by energy-weighted arc length.

In the original string method, the main difficulty is in the computation of the projected force. Numerical stability requires changing the way that the tangent vector is computed before and after the saddle points are crossed. To simplify the original string method, the discrete points on the string are evolved over some time interval δt according to the full potential force, i.e. replace Equation 2.69 by

$$\ddot{\mathbf{R}}_i = \mathbf{F}_i = -\nabla V(\mathbf{R}_i) \tag{2.70}$$

Then Equation 2.70 can be integrated in time by any ODE solver.

During the calculation of the simplified string method, the images are first evolved and then reparameterised (such as by interpolation to keep the images the same distance apart) at every iteration step. These images eventually converge to MEP.

Typically what could happen in a practical implementation is that each image of the string moves slightly at each step towards the nearest local minimum. The images are then interpolated so that they are equidistant and the process repeated.

The simplified string method has one more advantage: the initial string can be chosen arbitrarily, not necessary to be a string that connects two minima. The ends must only lie on different sides of the saddle.

Based on the efficiency of the computation, the dimer method is chosen to approach the saddle point and when the dimer's curvature becomes negative, MMFA is applied to get the

saddle point. The NEB method is also used for a double check of the energy barrier.

2.2.4 Atom Lists and Volumes

In order to save computational time during the force evaluation procedure in the saddle point searching technique, different radii were used to create atom lists on which forces must be evaluated without losing accuracy. It is possible to use such lists when interatomic potentials, describing the system of interest, have a rather small cut-off. In this work, atom lists were used when the α-Fe system was evolved using the KMC technique.

It was estimated, that in order to have accurate evaluations of the energy and forces acting on an atom in bcc Fe, atoms within 8.5Å must be included, as it shown in Figure 2.10. This radius is called the "inclusion radius" throughout this work.

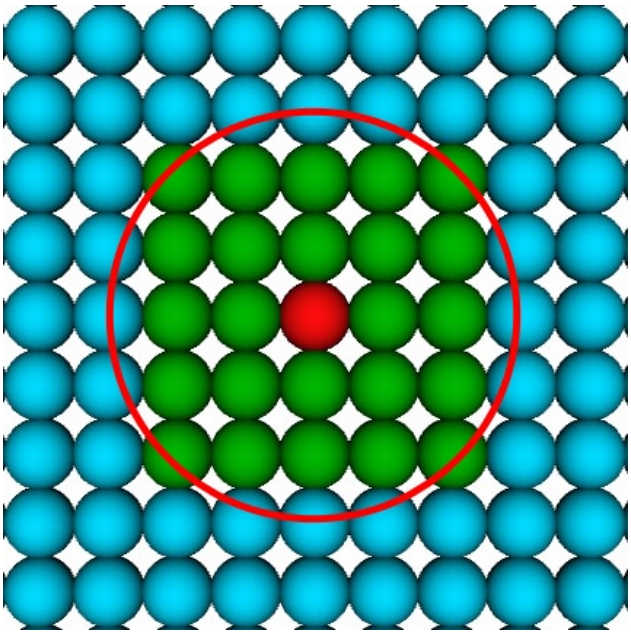

Figure 2.10: 2D representation of the inclusion radius: to have a good estimate of the energy and force acting on the Fe atom (red), atoms within an 8.5Å radius must be included (green).

Also in order to speed up simulations, different types of atom lists (volumes) are created to ensure minimum usage of computational power. The sizes of the volumes are controlled by the user of the KMC code and are created around residual defects in the system. The volumes are in ascending order of size as graphically presented in Figure 2.11.

- **Initial search radius** - this radius serves two purposes. The first one is to group residual defects into one cluster if defects are not separated by more than this value (in this work, 2.9 Å is chosen). This region is termed as a "**defect volume**" (DV) through this work and is one of the main characteristics in the otf-KMC technique.

  The second purpose is to create an initial list of atoms to be randomly displaced and used by one of the single-ended saddle search methods.

- **Graph radius** - this radius is used when building a graph network and it should include the search initial radius. 3NN (third nearest neighbour) distance is used in this work.

- **Search move radius** - this radius should be bigger than the graph radius and it includes the atoms that can move during the search for possible transitions. A typical value is 5.0Å.

- **Saddle converge radius** - sets an additional radius around the search move volume, to include even more atoms for a better convergence to a saddle point with the minimum mode following algorithm.

- **Inclusion radius** - this should include all atoms that are included in force evaluation and it should be far more than all the above radii.

2.2.5 Prefactor

When a saddle state is determined by one of the transition search methods, the next issue is to determine the prefactor for this particular transition, which describes how likely it jumps between local minima through the saddle. In this work two options were considered - a fixed prefactor with a value of $10^{13}s^{-1}$ and a calculated one, using the Vineyard equation [65]:

$$\tau = \frac{\prod_{j=1}^{N} \upsilon_j}{\prod_{j=1}^{N-1} \upsilon_j^*}, \tag{2.71}$$

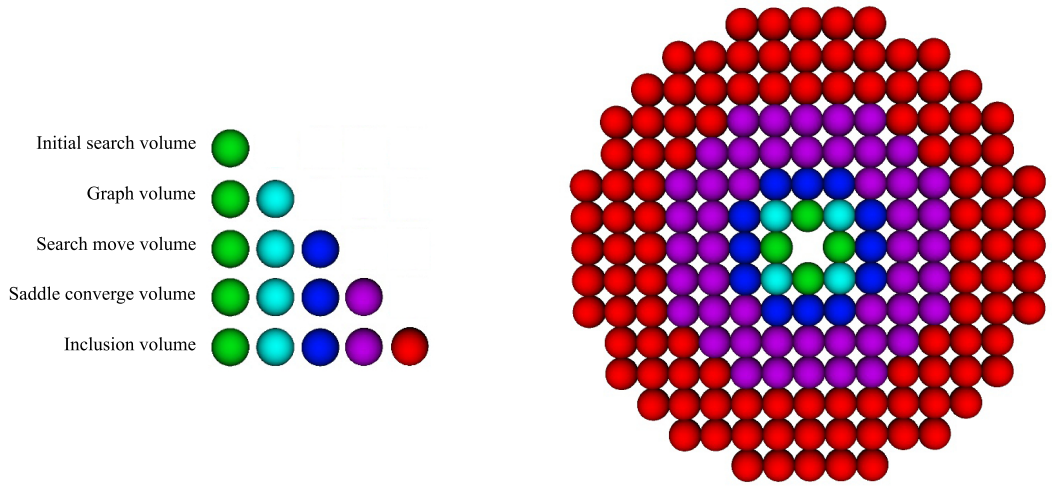

Figure 2.11: Representation of different atomic volumes used throughout the KMC algorithm around a vacancy defect: to create a defect volume (initial search volume), to classify a defect volume (graph volume), to look for saddles (search move volume), to converge to a saddle (saddle converge volume) and to estimate energetics of the saddle converge volume (inclusion volume).

where υ and υ^* are the normal frequencies for vibrations at the initial (local minimum) and saddle states respectively.

The normal frequencies used in Equation 2.71, at the initial and saddle states, are derived from the eigenvalues using Equation 2.72. Eigenvalues are calculated by numerically constructing the Hessian H (Equation 2.73) and then applying the DSYEV routine from the Linear Algebra Package (LAPACK).

$$\upsilon = \frac{\sqrt{\lambda}}{2\pi}, \tag{2.72}$$

here, λ is the eigenvalue of the Hessian matrix from which the normal frequency υ is derived. This Hessian is determined numerically whose i-j th element is given by:

$$H_{i,j} = \frac{1}{2\sqrt{m_i m_j}} \left(\frac{F_i^{j+} - F_i^{j-}}{2\delta} + \frac{F_j^{i+} - F_j^{i-}}{2\delta} \right), \tag{2.73}$$

where F_i^{j+} is the force acting on i-th component due to the positive ('-' - negative) displacement in the j-th components position, δ is the displacement (0.001Å) and m_i is atomic mass of the i-th atom. To gain accuracy, the element $H_{i,j}$ is calculated as an average of the symmetric elements, which can differ slightly due to rounding errors.

2.2.6 Transition Search Algorithm

An eight step procedure was implemented to find transitions on a defect volume.

- **Step 1: Initial displacement** - displace atoms within the initial search radius in the initial search volume, from a randomly picked atom in the volume.

- **Step 2: Saddle search** - after the initial displacement, the Dimer method is used to approach a saddle state, which is connected with the initial minimum state via the minimum energy path. The Dimer method was chosen because it is not only one of the most robust methods that uses only first derivatives, but also it estimates the curvature, which is directly linked with the lowest mode, without additional force evaluations.

- **Step 3: Convergence to a saddle** - when the Dimer approaches a saddle, the procedure switches to use the minimum mode following algorithm when the Dimer's curvature becomes negative.

- **Step 4: Estimate eigenvalues** - if prefactors are calculated on the fly, the eigenvalues at the saddle state are calculated and together with the initial eigenvalues are used to calculate the prefactor for this transition later on.

- **Step 5: Check of the saddle's rank** - if prefactors are calculated on the fly, it is important to ensure that the rank of the saddle point is equal to 1, that means it has only one negative eigenvalue. If the saddle has rank 2 (there are two negative eigenvalues), the Vineyard's equation is invalid and the prefactor cannot be calculated. To ensure, that the saddle has rank of 1, the original minimum mode following algorithm suggested by Pedersen *et al.* [59] is used to climb down from a rank 2 saddle state, to a rank 1.

- **Step 6: Uniqueness check of the saddle** - once the saddle state is approximated, calculation of the separation of atoms in the defect volume determines if it is a valid

result. If the separation is less then (0.5Å), the result is taken as a duplicate of one already determined and the procedure is terminated.

- **Step 7: Find the final minimum** - to find the final minimum joined by the MEP through the saddle state, the system at the saddle state is given a little push in the direction of the vector from the initial minimum state to the saddle state. Then this minor displacement is followed by a minimisation that uses two methods: the first one is the classical steepest descent method with tolerance of 10^{-1}eV/Å to approach the final minimum quickly with as little computational costs as possible and the second one is the L-BFGS-B method with a tight tolerance of (10^{-3}eV/Å), which works best when the initial system state is in the neighbourhood of a minimum.

- **Step 8: Calculate the rate value** - if the previous steps were successful, the transition search algorithm finishes by calculating the rate value for the found transition using the Arrhenius equation (Equation 2.48). The prefactor is either calculated on the fly or using the default value of $10^{13}s^{-1}$. $10^{13}s^{-1}$ was found to be a typical value for many transitions and considerable computing time is saved using a fixed prefactor.

If in any of the steps the algorithms fail to complete their tasks, the transition search is discarded as unsuccessful.

2.2.7 on-the-fly Kinetic Monte Carlo Algorithm

The fundamental steps of the otf-KMC method, suggested by Henkelman and Jónsson [55], can be summarised as follows:

The first step is to identify defects present in the system. In our cases, this might be an interstitial atom, a group of interstitials, a vacancy or a group of vacancies. It is crucial to locate defects in order to minimise the search space by limiting the volume where the searches are initiated, thus making transition search algorithms and the KMC technique more efficient. The next step is where a saddle search method is employed to find possible

transitions from the current state and estimate rate values for each of them. Then, the next step is the KMC roulette technique, which picks a random transition as a new state and calculates the elapsed simulation time between current state and the new one. Lastly, the system is advanced to a new state. In this thesis, generally only one step otf-KMC was applied for searching the transition but in principle the method can be repeatedly applied to follow a system's motion over long time scales.

2.2.8 Parallelisation

To efficiently perform the transition searches of the otf-KMC, it is necessary to parallelise the computation over multiple processors.

During the parallelisation, the main applied steps that the main server will do are:

- Minimising the initial system.
- Identifying defects in the initial system.
- Building defect volumes.

After that, the server allocates jobs need to be done like transition searches for the defect volumes on multiple processors. It establishes communication with these clients to send the data needed to perform their tasks and to gather results for further actions.

During this project, between 8 and 60 processors were used in parallel on Loughborough University's high performance computer (Hydra).

Chapter 3

Helium Bubble Formation and Growth in bcc Fe

3.1 Introduction

Reduced-activation ferritic/martensitic steels are candidate materials for use in nuclear reactors [66, 67]. The presence of transmutation-created helium plays an important role in the microstructural evolution of these steels under neutron irradiation. Interstitial helium atoms increase the production of Frenkel pairs whilst substitutionals tend to decrease this production [68].

Small helium-vacancy (He_nV_m) clusters may play an important role in the nucleation of He bubbles. Helium bubbles will cause additional swelling and embrittlement [1, 69]. Helium effects on microstructural evolution in tempered martensitic steels were characterised using a novel in situ He-implanter technique by Yamamoto *et al.* [70] combined with neutron irradiation at 500 °C. Most bubbles that formed had diameters of less than 2 nm (see Figure 3.1).

Ono [71] has studied the formation and migration of He bubbles in high purity Fe and Fe-9Cr ferritic alloy by in situ transmission electron microscopy (TEM) observation, which

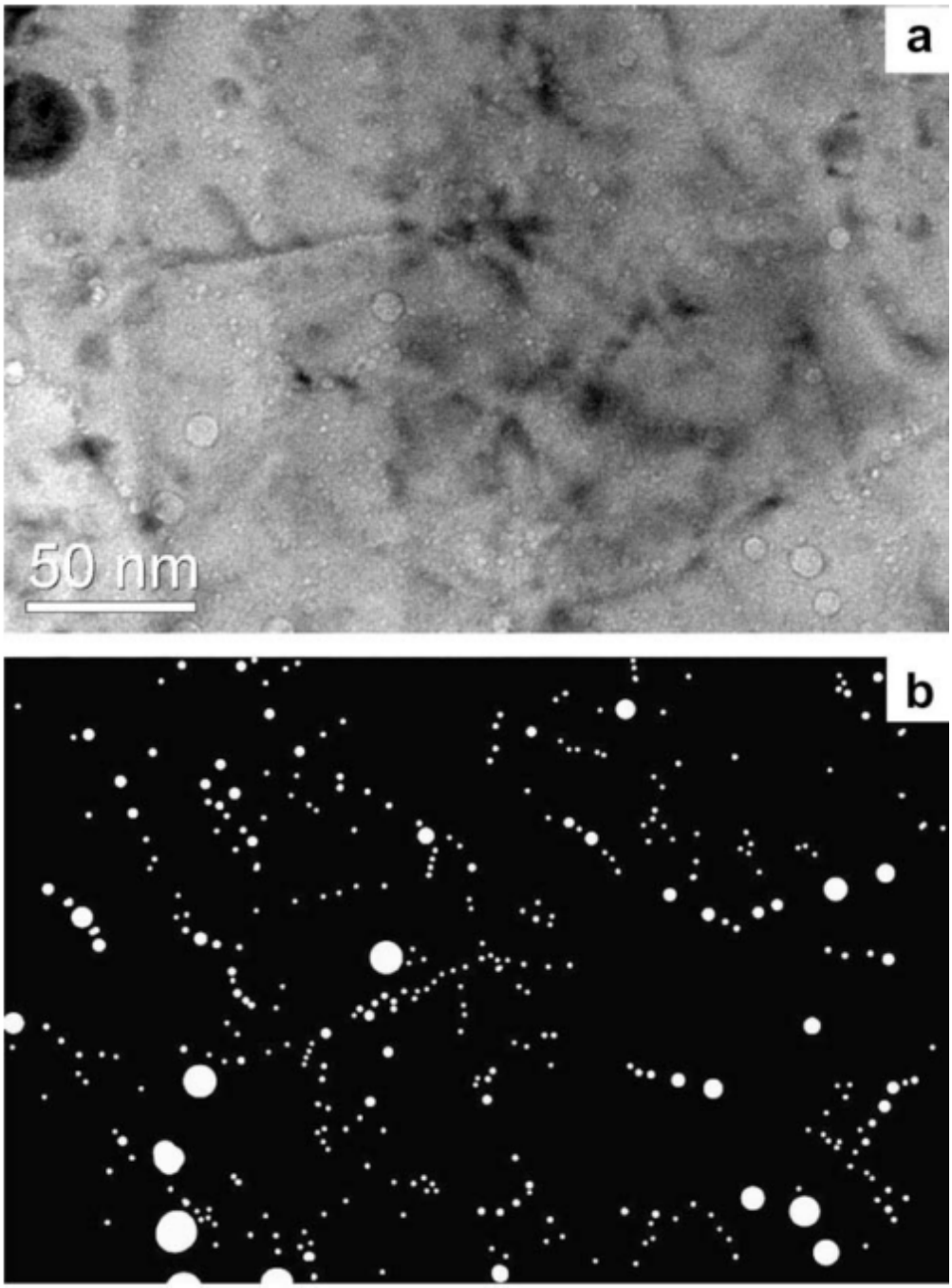

Figure 3.1: (a) shows a representative micrograph for the AT F82H implanted to 380 appm He (nominal He/dpa = 40 appm/dpa) imaged at a 768 nm under-focus condition. A map for the features identified as bubbles by through-focus sequence examinations are shown in the white on black image in (b). It shows that this irradiation condition produced $\sim 5.3 \times 10^{22}/m^3$ small bubbles with an average diameter of 2.0 ± 1.4 (one standard deviation) nm. The image is taken from [70].

shows bubbles preferentially form at dislocations in both materials at 200-400 °C. The size distributions of bubbles formed at 400 and 600 °C were compared to show that adding Cr could reduce the diffusion of He. Some bubbles that were not formed at dislocations, were shown to grow in size at elevated temperatures and the motion of small bubbles ($<\approx$ 3 nm diameter) was observed over periods of seconds in pure Fe at 750 °C. However the energy barrier for this motion to occur is very large, of the order of 3.5 eV.

Work by Henry *et al.* [72] demonstrated the effect of helium on the fracture properties of a 9Cr martensitic steel. The large number of He bubbles observed in the TEM micrograph were of the order of 0.5 nm in diameter and this small size was attributed also to the influence of Cr inhibiting bubble growth. Finally experimental work from Yu *et al.* [73] in pure Fe at room temperature has indicated that there is a distribution of sizes with a fairly narrow spread and preferred He bubble size of the order of 1.3 nm in diameter (see Figure 3.2).

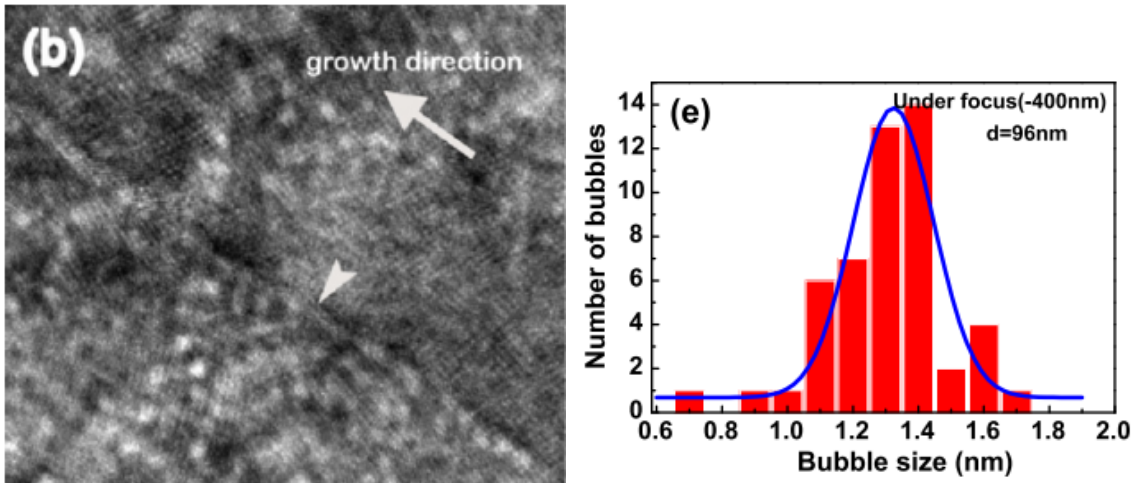

(a) (b)

Figure 3.2: (a) Higher magnification cross-sectional TEM (XTEM) micrograph shows the formation of He bubbles along a grain boundary. (b) Statistical distribution of He bubble sizes in 96 nm irradiated Fe films with an average grain size of 700 nm show the average bubble size is 1.3 nm. The images are taken from [73].

The conclusion of the experimental work is therefore that the bubbles in Fe prefer to remain small at room temperature and especially so when chromium is added to the matrix.

When the temperature is increased then smaller numbers of larger bubbles are formed.

However, the atomistic properties of He in metals are difficult to identify experimentally. Thus atomistic simulations such as molecular dynamics (MD) and Kinetic Monte Carlo (KMC) provide useful tools to study the formation and the stability of these clusters.

Because of the significance of the He bubble problem, there has been much recent work on atomistic modelling and developing interatomic potentials to model dynamical processes involving He in metals. Caro *et al.* [74, 75] investigated the properties of helium bubbles in Fe and FeCr alloys, mainly focussing on their dimensions and determining the bubble pressure. Gao *et al.* [76] carried out atomistic simulation to examine the clustering of helium in bcc iron and the growth of an helium bubble in helium-rich, vacancy-poor conditions. It was shown that a $1/2 < 111 >$ dislocation loop is formed as a sequential collection of $< 111 >$ crowdions, the latter being the most stable self-interstitial atom configuration in the presence of an over-pressurized He cluster. Di *et al.* [77] found that helium bubbles in Au preferentially nucleate at screw dislocation nodal points and result in helium bubble superlattice formation, which is completely isomorphic with the screw dislocation network along the twist-grain boundary. Stoller and coworkers investigated the pressure and compressibility for He vacancy clusters, bubble size, He content and temperature effects based on the Stoller's potential described in Section 2.1.3.2 [45, 78, 79]. It was found that the equilibrium He content is rather low and at a room temperature it is ~ 0.38 to 0.5 He per vacancy for bubble diameters from 1 to 6 nm by adopting a mechanical bubble dilatation criterion in which the equilibrium bubble does not produce any stress fields in the matrix [78]. Jourdan and Crocombette [80] proposed a variable-gap energy model for helium bubbles in Fe, based on MD calculations to determine quantities such as binding energies, solid to fluid transition and helium density in the bubbles.

Hafez and Schäublin [81] investigate the basic mechanisms of the interaction between a moving edge dislocation and a void or He bubble, as a function of its He content, temperature, interatomic potentials and interaction geometry by MD simulation. The results show that

the He bubble induces an inhomogeneous stress field in its surroundings, which strongly influences the dislocation passage depending on the geometry of the interaction.

Hayward and Deo [82] investigated He-H bubbles to examine the synergistic effect between H and He and were able to show that this synergy arose as a consequence of bubble growth through helium induced loop punching, aided by the presence of hydrogen, instead of as a direct interaction between hydrogen and helium.

Terentyev *et al.* studied the diffusivity of small helium vacancy clusters and pure He clusters and also investigated the dissociation energies for the He vacancy clusters [83]. Hepburn performed a first-principles study to show the binding of additional He and V to existing He_nV_m clusters could lead to unbounded growth [84].

Yang *et al.* [85] considered the nucleation of He bubbles at 800 K in bcc Fe using a methodology similar to that described here. They were able to conclude that He would diffuse with a low energy barrier of 0.06 eV rapidly forming small clusters that in turn could also diffuse and that He_4 clusters could emit an Fe interstitial and bind with a vacancy. This process is sometimes termed 'trap mutation' in the literature. However once an He_n cluster formed with a vacancy it became effectively immobile. This was followed by work by Gao *et al.* [86] who investigated the properties of single vacancy clusters (He_nV). The results show that at 300 K the He_nV cluster is stable up to $n = 6$ and up to $n = 16$, the He_nV_2 cluster is stabilised by the emission of an Fe interstitial in the form of a $< 110 >$ dumbbell.

Morishita also evaluated the displacement field around a helium-vacancy cluster in Fe by molecular dynamics and molecular static calculations [87]. Through computing the pressure of the He, it was found that when the He pressure of a He-V cluster is high, Fe displacements are compressive in the direction away from the cluster, but many configurations exist where the distortion is not radially symmetric.

Trinkaus studied the energetics and formation energetics of Helium bubbles in metals [88]. It was pointed out that at low helium production rates and high temperatures, an He_nV_m cluster or helium bubble can absorb a sufficient number of thermally-activated or

irradiation-induced vacancies to keep the internal pressure below the threshold values for metal self-interstitial emission and dislocation loop punching. He also declared that at low temperature, the clustering of helium leads to spontaneous formation of a Frenkel pair and emission of metal interstitial clusters by over-pressurized bubbles and this is energetically more favourable than the emission of single interstitials .

In this chapter, the results of a study both on the statics of small helium-vacancy clusters in a bcc iron and their interaction with nearby collision cascades are presented, which will provide insight into how a helium bubble forms and grows. We also investigate the structure of small He clusters in Fe and the energy barriers that need to be overcome before growth by diffusion can occur. The main results have been published in [89, 90].

3.2 Potential

As mentioned in Section 2.1.3.2, we have used two different groups of potentials for He in a bcc Fe system. The potentials will be compared in the following sections (Section 3.3 and Section 3.7) by two aspects: first is the formation energy of defects and various helium-vacancy clusters He_nV_m, and the other is the behaviour under collision cascades. The results for the potentials give consistent conclusions. We choose Gao's potential for detailed study as this has been applied more widely.

3.3 Formation Energy

The formation energy of an He-vacancy complex He_nV_m (n He in m Fe vacancies) is defined [89] as the difference in total energy between a crystal containing a defect and a perfect crystal of the same number of Fe atoms with the corresponding number of helium atoms at infinity in their lowest energy structure. This structure was determined separately for the

two potentials for comparison.

$$E_f = E_b + (n-m)E_{vac} - N_{Fe}E_{Fe} - nE_{He}^{sub}, \tag{3.1}$$

where E_f is the formation energy; E_b is the energy of the lattice containing the bubble; E_{vac} is the formation energy of a single vacancy in bcc Fe lattice, defined as follows;

$$E_{vac} = E(v, N-1) - (N-1)E_{Fe}, \tag{3.2}$$

where $E(v, N-1)$ is the energy of the lattice containing one vacancy, $N-1$ is the number of Fe atoms in the system. N_{Fe} is the number of Fe atoms in the lattice containing the bubble; E_{Fe} is the cohesive energy of Fe and E_{He}^{sub} is the energy of a helium substitutional atom, defined as follows,

$$E_{He}^{sub} = E_{sub}^{ref} - N_{Fe}^{ref}E_{Fe}. \tag{3.3}$$

It is the energy difference between a perfect lattice with an He atom at infinity and the same one that has an Fe atom replaced by the He, i.e. the energy difference from replacing an He atom at infinity with an Fe atom at infinity.

In the calculations for the formation energy, the box size is usually set to $30a_0 \times 30a_0 \times 30a_0$, where a_0 is the bcc Fe lattice parameter. For all calculations periodic boundary conditions and constant volume are used.

First, we list the formation energy of several defects in the system. The calculations give similar results which show the helium atom is energetically favourable to locate in the substitutional site while the tetrahedral interstitial is more stable than the octahedral.

Potential	Fe cohesive energy	vacancy formation energy	He substitutional formation energy	He tetrahedral formation energy	He octahedral formation energy
Stoller	4.32 eV	1.71 eV	3.70 eV	4.33 eV	4.70 eV
Gao	4.013 eV	1.72 eV	3.76 eV	4.38 eV	4.47 eV

Table 3.1: The formation energy of defects calculated in two potentials.

However, it is later shown that the energy barrier for an isolated interstitial He to become substitutional and emit an Fe interstitial is very high. In theory, Kittle demonstrates the cohesive energy of Fe is 4.28 eV [91]. Although there are some errors according to this calculation, both of the two potentials still show consistent results with the experimental work as shown in the following. Gao's potential is chosen due to that it shows better statistical results in the cascade simulations.

Assuming that the He atoms are located in pre-existing vacancies in the bcc Fe system, the formation energy of the helium-vacancy clusters He_nV_m is calculated in two different ways for comparison. The first way is to use spherical voids for the approximation of the vacancies and an initial fcc structure for the helium clusters. The clusters have been generated with the following procedure. We start by creating the pure bcc Fe lattice, then remove atoms to get an approximately spherical vacancy cluster. Next we generate an He bubble in the fcc structure of approximately the same size as the vacancy cluster and place this into the Fe lattice. The system is relaxed using a conjugate gradient algorithm. For each ratio several initial random configurations are tested and the one with the lowest formation energy is kept. The results determined in this way have been published in [89].

It was found that the previous method did not always produce the lowest energy system and so a second method was adapted. For the second way, a Monte Carlo algorithm used to determine the lowest energy configuration of the cluster [92] which is organised as follows. First, the energetics of voids without helium are investigated. A vacancy is introduced into the simulation cell and the system is minimised using a conjugate gradient algorithm, yielding a single vacancy formation energy E_{vac} of 1.72 eV. Next, the atom with the highest potential energy is removed from the system and again the system is minimised. This scheme is iteratively continued to create voids up to the number of target vacancies and the formation energy of each is calculated. Next, helium atoms are introduced to the vacancies. The total system energy is measured and recorded. At this point, a Metropolis MC scheme [93] is used to find the low energy configurations. Every helium in the system is randomly displaced from

its site up to a maximum of r_{max} (4.5 Å, the cut off distance for He-He interactions) in each of the x, y and z directions and then minimised using the conjugate gradient algorithm. Each bubble is evolved for a minimum of 10,000 steps. After that, the searches will be terminated if the system energy does not drop within a further 10 steps. A schematic of this iterative process is shown in Figure 3.3.

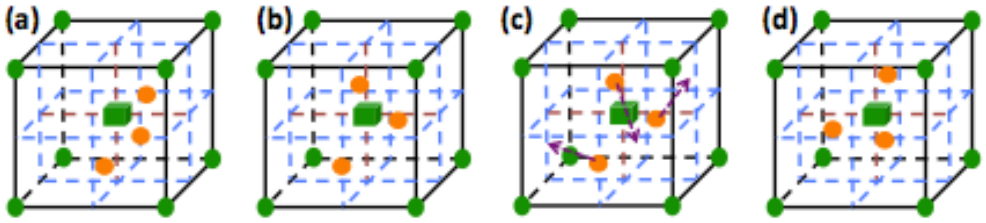

Figure 3.3: The process is shown for He_3V_1. First, He atoms are randomly inserted (a) and then minimised (b). Next, He atoms are displaced randomly in the x, y, z directions (c) and minimised multiple times. The final configurations are determined from the lowest energy of the minimised structures (d). The He atoms are shown as red spheres and Fe atoms are green. The green cube is the vacancy of the bcc Fe cell.

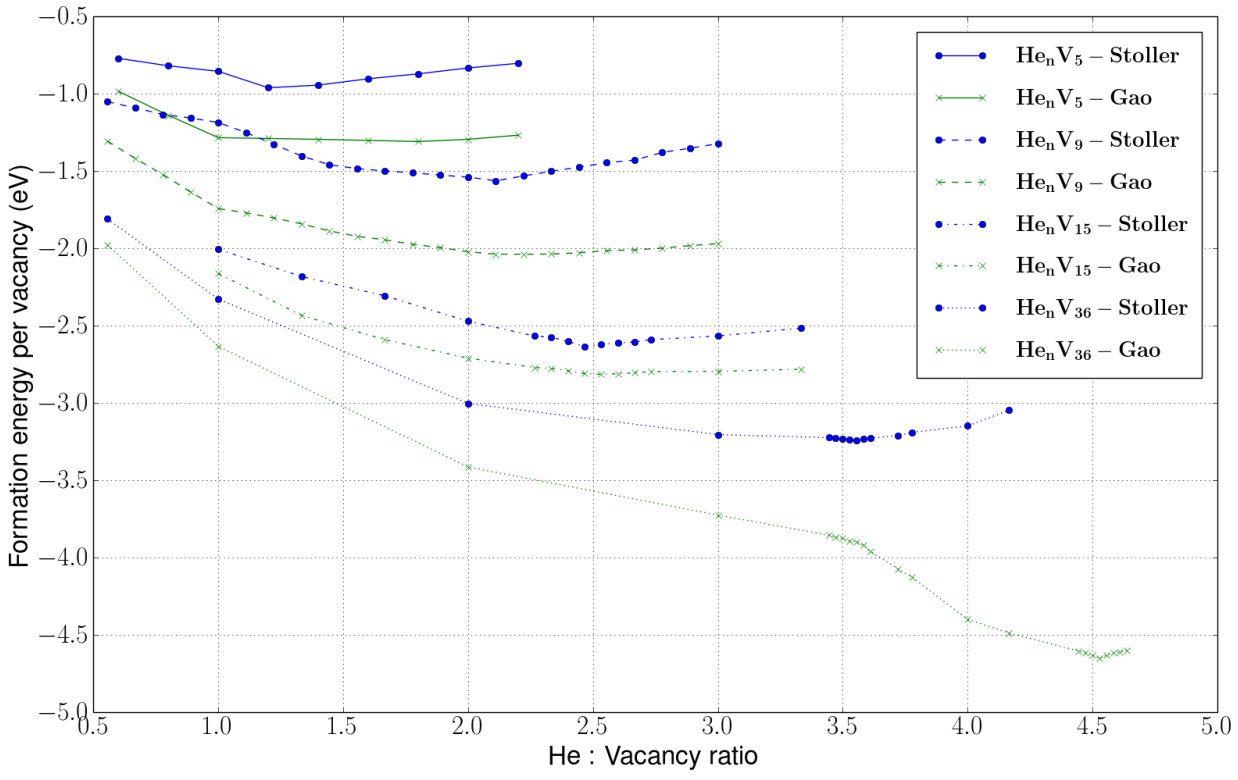

Figure 3.4: The formation energy as a function of the number of helium atoms for different sizes of He_nV_m clusters using two different potentials and computed in MC algorithm for the configuration of He_nV_m.

Figure 3.4 shows the formation energy of the He_nV_m clusters calculated from both the

tested potentials from the MC algorithm at 0 K. Each curve is with a fixed number of vacancies, which implies that all the bubbles locating on the same curve have the given number of preformed vacancies before the He is inserted. To ensure the results can be compared on a similar scale, the figure shows the formation energy per vacancy. It is clear that each curve reveals the same trend; that is to say there is an optimal (lowest formation energy per vacancy) He-to-vacancy ratio for each curve (calculated with a fixed number of vacancies). The optimum bubble size is given by the minima on the curves in Figure 3.4. It can be seen that the optimum ratio increases from around 1 : 1 for small bubbles up to more than 4 : 1 for large bubbles. Further, each curve stops at the final point because the bubble will be no longer stable to hold more helium with the given number of vacancies; in other words, if extra helium is added it will cause the bubble to push the neighbouring Fe atoms into split interstitials with more vacancies in the bubble. If we compare the previous work in [89], it is clear that the second way using the MC algorithm gives lower energy configurations rather than locating the helium atoms in fcc sites. Applying Gao's potential results in a lower formation energy than using Stoller's potential. The lowest curve in Figure 3.4 is less smooth than the other curves. This is due to the large number of vacancies in the system and the length of time required to undertake the calculations. The MC algorithm would require more than 10,000 moves in order to obtain better statistics. However, the computing time required for this would be several weeks and since the trend in the curve is clear. These calculations were not undertaken.

Moreover, we have compared the volume of He bubbles (see Figure 3.5) using a Voronoi algorithm with the work done by Caro *et al.* [74]. This gives a consistent curve of the volume of the He bubble versus number of He to help verify the reliability of these potentials.

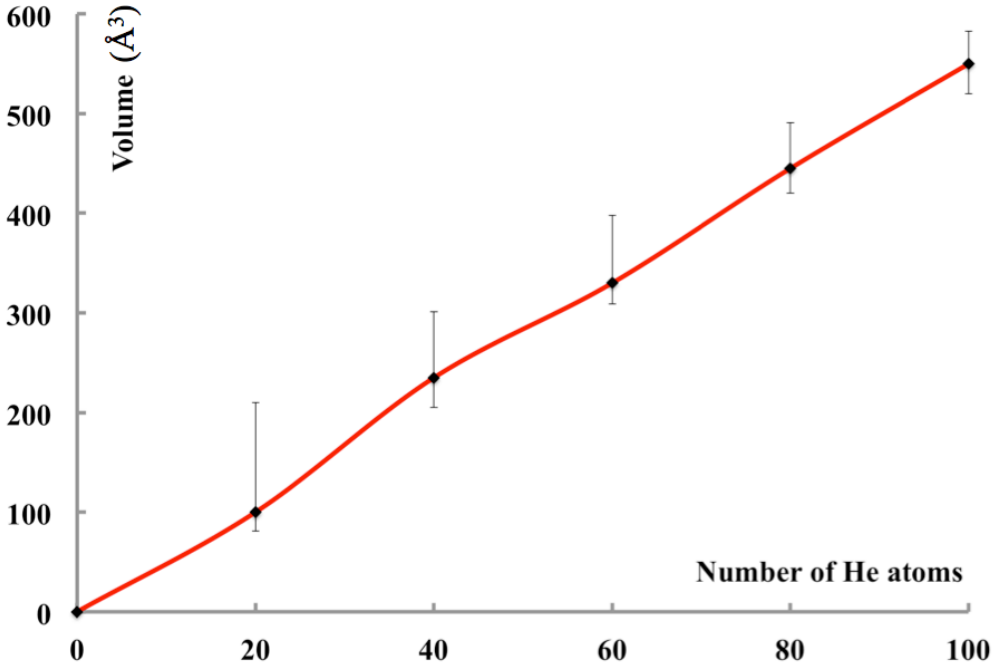

Figure 3.5: The volume as a function of the number of helium atoms for different sizes of $He_nV_m, 5 \leq m \leq 36$ clusters using Gao's potential. The error bars show the the minimum and maximum of the volume of the He bubbles.

3.4 Diffusion of isolated defects without the presence of He in bcc Fe

Before investigating how helium atoms diffuse and form into clusters, it is necessary to understand the properties of an Fe vacancy and interstitial first.

The formation energies of several defects in the bcc Fe system are listed in Table 3.2.

Fe cohesive energy	vacancy	divacancy	Fe tetrahedral interstitial	Fe octahedral interstitial	Fe $< 110 >$ dumbbell interstitial	Fe $< 111 >$ dumbbell interstitial
4.013 eV	1.72 eV	3.3 eV	4.0 eV	4.17 eV	3.53 eV	3.94 eV

Table 3.2: The formation energy of Fe defects in bcc Fe.

Results reveal that the $< 110 >$ Fe dumbbell interstitial has a more stable configuration rather than $< 111 >$.

Diffusion barriers of single vacancy and dumbbell interstitials to the first neighbour and second neighbour are found using saddle point searches and checked with the NEB method as shown in Table 3.3 with a schematic diagram illustrated in Figures 3.6 and 3.7.

defects	The energy barrier diffuse to 1 N	The energy barrier diffuse to 2 N
isolated vacancy	0.64 eV	2.61 eV
$< 110 >$ dumbbell interstitial	0.31 eV	0.33 eV

Table 3.3: The diffusion barrier of Fe defects in bcc Fe.

The calculations in Table 3.2, Table 3.3 and Figure 3.7, Figure 3.8 are in agreement with experimental results and *ab-initio* calculations [94, 95, 96, 97, 98].

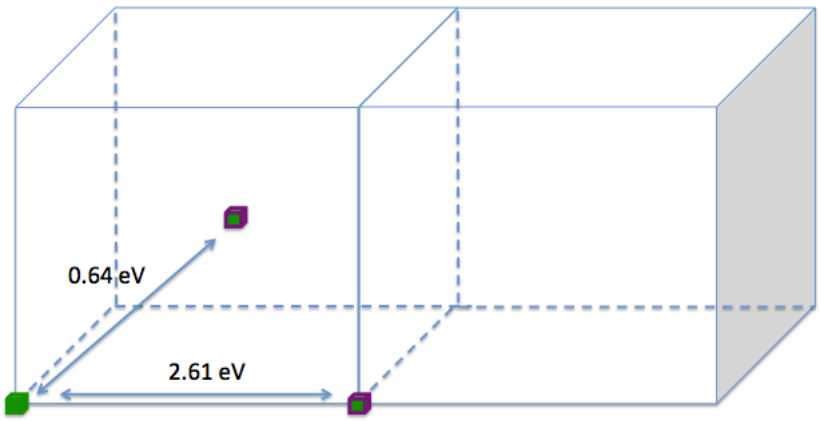

Figure 3.6: Illustration of the diffusion of an isolated Fe vacancy. The green cube is the Fe vacancy. The purple outline indicates the configuration after transition.

Fe interstitials can quickly turn into dumbbell interstitials as illustrated in Figures 3.9, 3.10 and 3.11.

We have also checked the case of the divacancy and find that the structure of the divacancy allows one of the vacancies to diffuse with a lower energy barrier than an isolated vacancy. Therefore, an extra vacancy nearby could help the vacancy diffuse more quickly. In fact, two vacancies in second neighbour configuration is 0.1 eV lower than the divacancy configuration (see Figure 3.12).

In summary, Fe vacancies and interstitials could diffuse within MD time scales at room temperature if we assume a constant prefactor of 10^{13}.

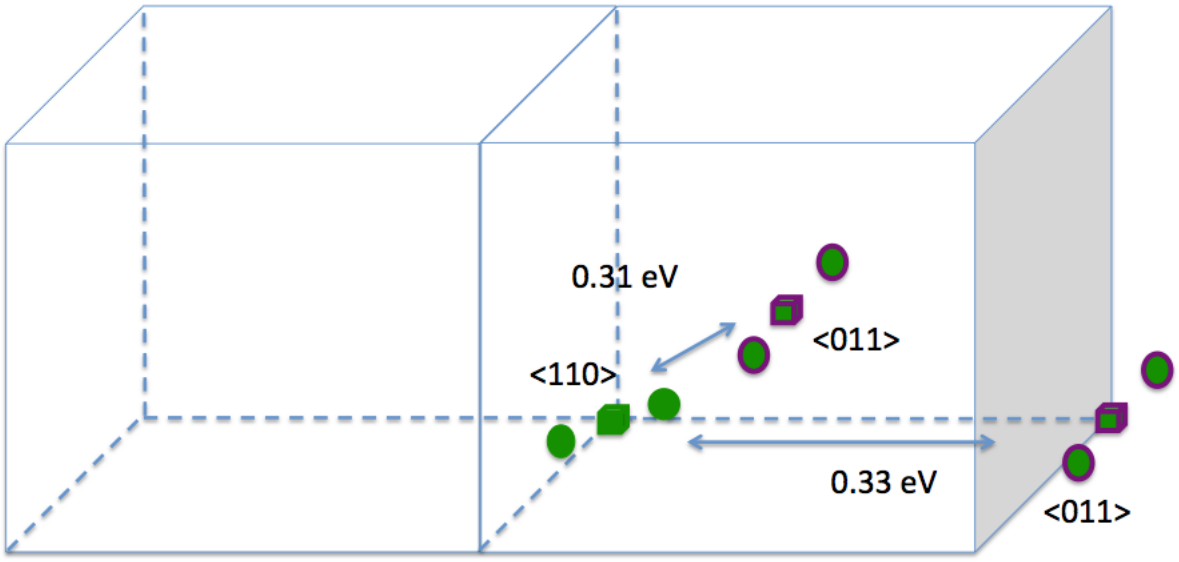

Figure 3.7: Illustration of two diffusion mechanisms for the Fe $< 110 >$ dumbbell interstitial. The green sphere is the Fe interstitial and the green cube is the Fe vacancy. The purple outline represents the configuration after transition.

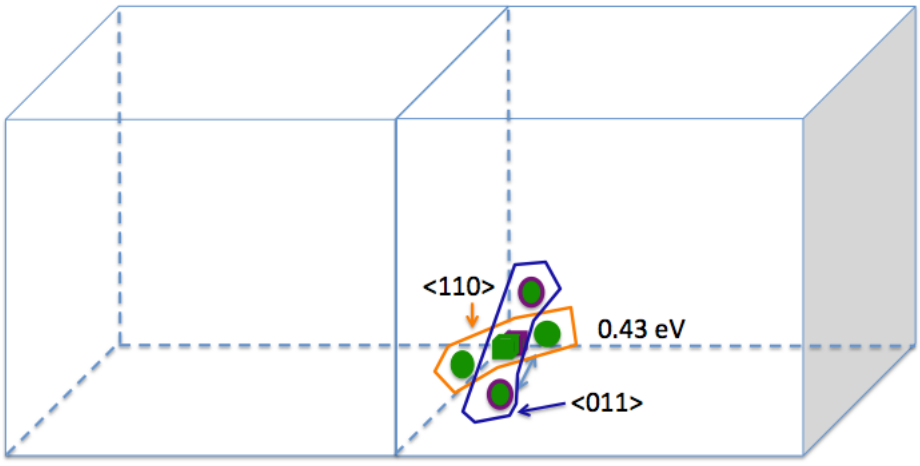

Figure 3.8: Illustration of the reorientation of the Fe $< 110 >$ dumbbell interstitial. The green sphere is the Fe interstitial and the green cube is the Fe vacancy. The purple outline represents the configuration after transition.

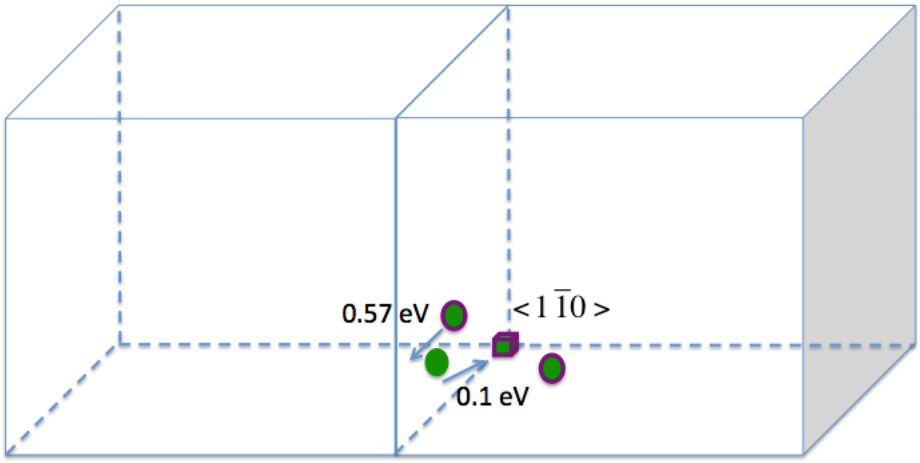

Figure 3.9: The transition of the Fe tetrahedral interstitial to the $< 1\bar{1}0 >$ dumbbell interstitial with the energy barrier of 0.1 eV and the reverse barrier of 0.57 eV. The green sphere is the Fe interstitial and the green cube is the Fe vacancy. The purple outline indicts the configuration after transition.

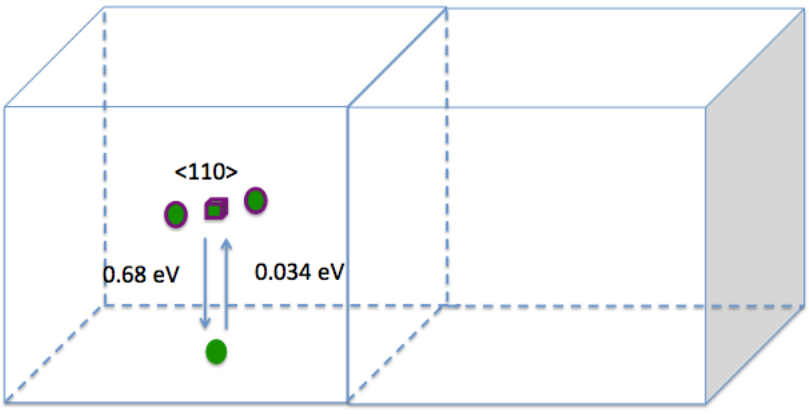

Figure 3.10: The transition of the Fe octahedral interstitial to the $< 110 >$ dumbbell interstitial with the energy barrier of 0.034 eV and the reverse barrier of 0.68 eV. The green sphere is the Fe interstitial and the green cube is the Fe vacancy. The purple outline indicts the configuration after transition.

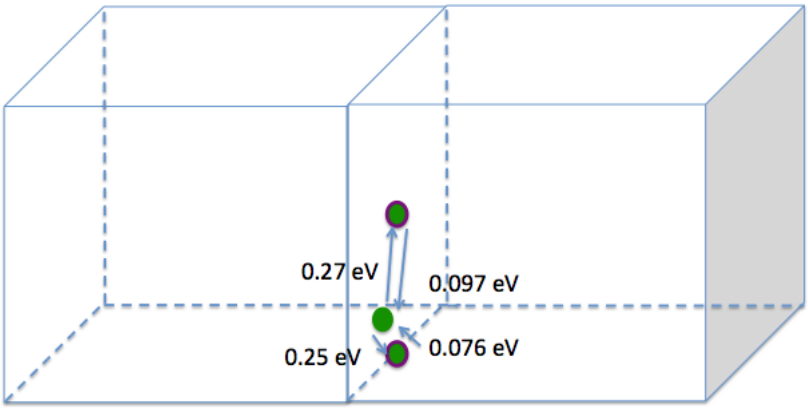

Figure 3.11: Two transitions of the Fe tetrahedral interstitial to the octahedral interstitial. The green sphere is the Fe interstitial and the green cube is the Fe vacancy. The purple outline indicts the configuration after transition.

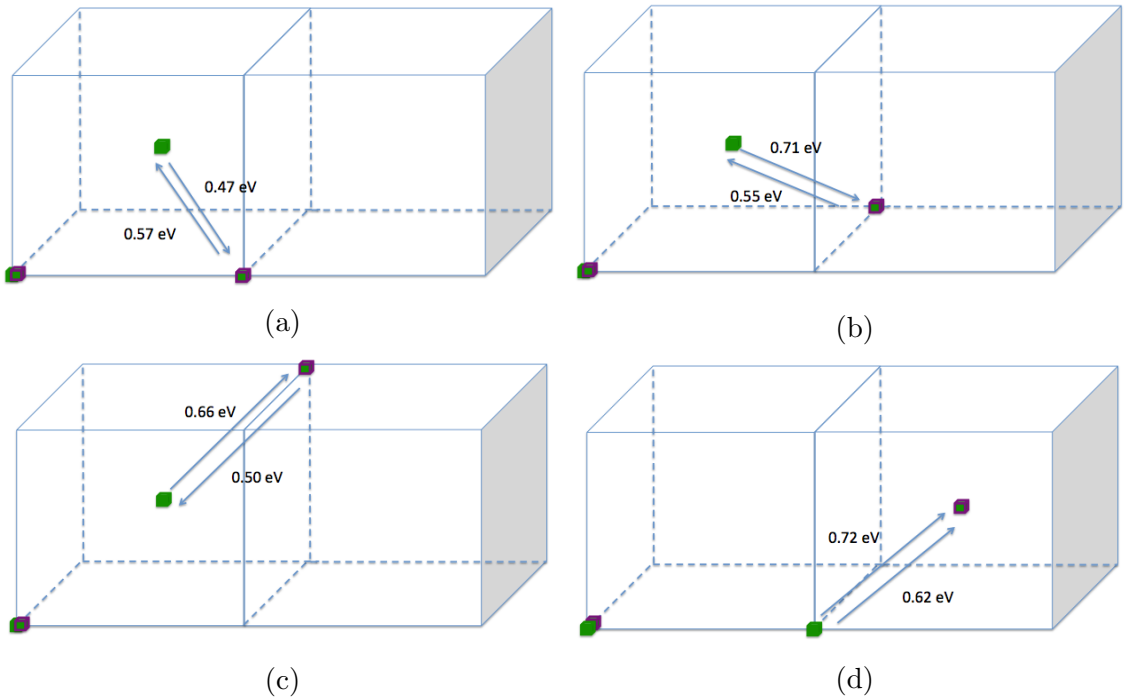

Figure 3.12: Illustration of the diffusion of two vacancies. The green sphere is the Fe interstitial and the green cube is the Fe vacancy. The purple outline indicts the configuration after transition. (a) The diffusion between the Fe divacancy and two vacancies in second neighbour. (b) The diffusion between the Fe divacancy and two vacancies in third neighbour. (c) The diffusion between the Fe divacancy and two vacancies in fifth neighbour. (d) The diffusion between two vacancies in second neighbour and fourth neighbour.

3.5 He substitutional atoms with vacancies nearby

3.5.1 He substitutional with a vacancy nearby

The He atom favours the substitutional site but the energy barrier to be overcome to form this from an interstitial position is very high. It was calculated as 6.76 eV. It is therefore useful to understand the stability of the He substitutional atom with some vacancies near by. After the minimisation, the He substitutional atom is stable with a vacancy located in first neighbour. If the vacancy sits in the second neighbour position, a direct swap between the He and vacancy can occur within nanoseconds at room temperature. However, the vacancy is energetically favourable to be in the first neighbour position (see Figure 3.13).

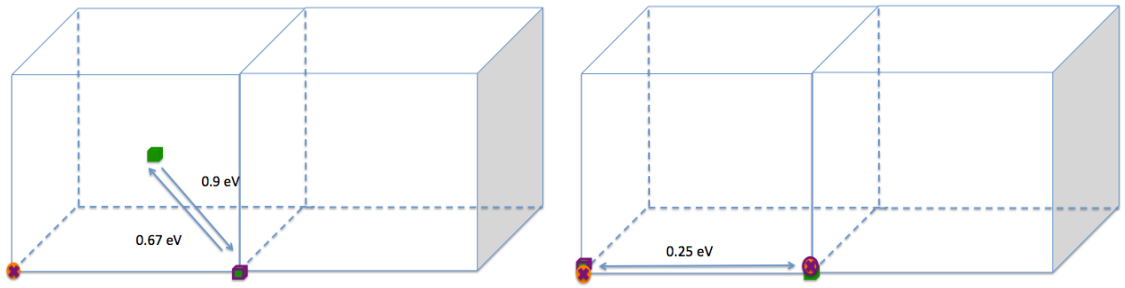

Figure 3.13: Illustration of the diffusion of the He substitutional atom with an Fe vacancy nearby. The green cube is the Fe vacancy. The orange sphere represents the He atom. The purple outline shows the configuration after transition. The cross sign inside indicts the substitutional atom. (a) The vacancy diffuses from first neighbour to the second neighbour. (b) The He substitutional atom swaps with the vacancy in second neighbour site.

3.5.2 He substitutional with two vacancies nearby

An He substitutional atom with two vacancies has also been investigated. Some typical transitions are shown in Figure 3.14. The lowest energy configuration that the He and vacancies tend to form is a He_1V_3 cluster which is an isosceles triangle consisting of 3 vacancies where one sits as the first neighbour of the other two and the remaining two are second neighbours with the He in the centre of the triangle. This cluster is stable since

no successful transitions have been found in KMC searches and if we use the NEB method to check the barrier of its diffusion, it is over 5 eV.

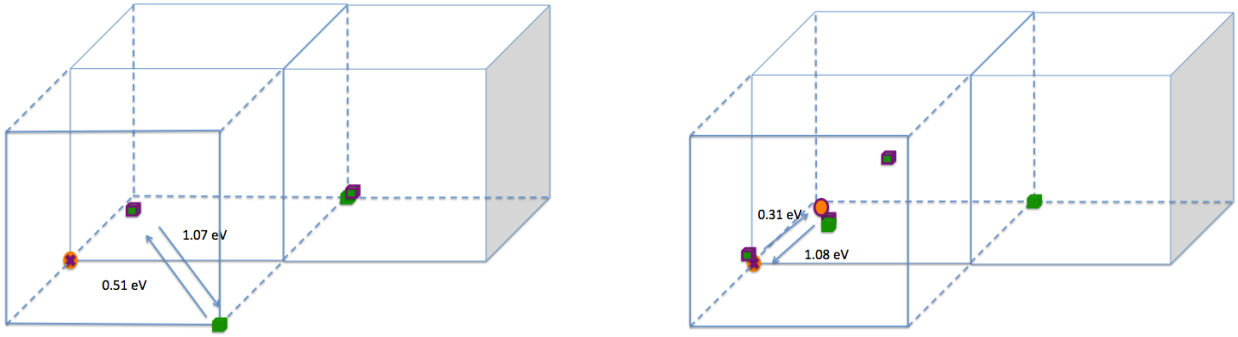

(a) (b)

Figure 3.14: Illustration of the transition of He substitutional atom with 2 vacancies. The green cube is the Fe vacancy. The orange sphere represents the He atom. The purple outline shows the configuration after transition. The cross sign inside indicts the substitutional atom. (a) One vacancy diffuse to the first neighbour of the He and the other remains with the energy barrier of 0.51 eV and the reverse barrier of 1.07 eV. (b) The transition of the He substitutional atom with two vacancies nearby to the triangle structure of He_1V_3 with the energy barrier of 0.31 eV and the reverse barrier of 1.08 eV.

Next we will focus on how an He interstitial cluster can evolve into bubbles.

3.6 Helium clustering and Bubble Formation

As in the last section, we only show the results using Gao's potential. Although we also used Stoller's potential with similar results.

To investigate how helium atoms can form clusters or bubbles, first we randomly distribute helium interstitials into a pure bcc Fe system and evolve the system using MD. This is similar to the methodology employed by Yang *et al.* [85]. Different concentrations of helium atoms are selected for comparison. The temperature of the system is set at 500K. The system is then evolved for up to 5 ns.

From Figure 3.15, we can see that most of the helium atoms accumulate into clusters over nanosecond time scales. Furthermore, the system is observed to change very little between 4 and 5 ns. We find that isolated helium atoms are highly mobile and aggregate into clusters. Some typical He clusters and bubbles are labelled in Figure 3.15. Here we define a bubble as

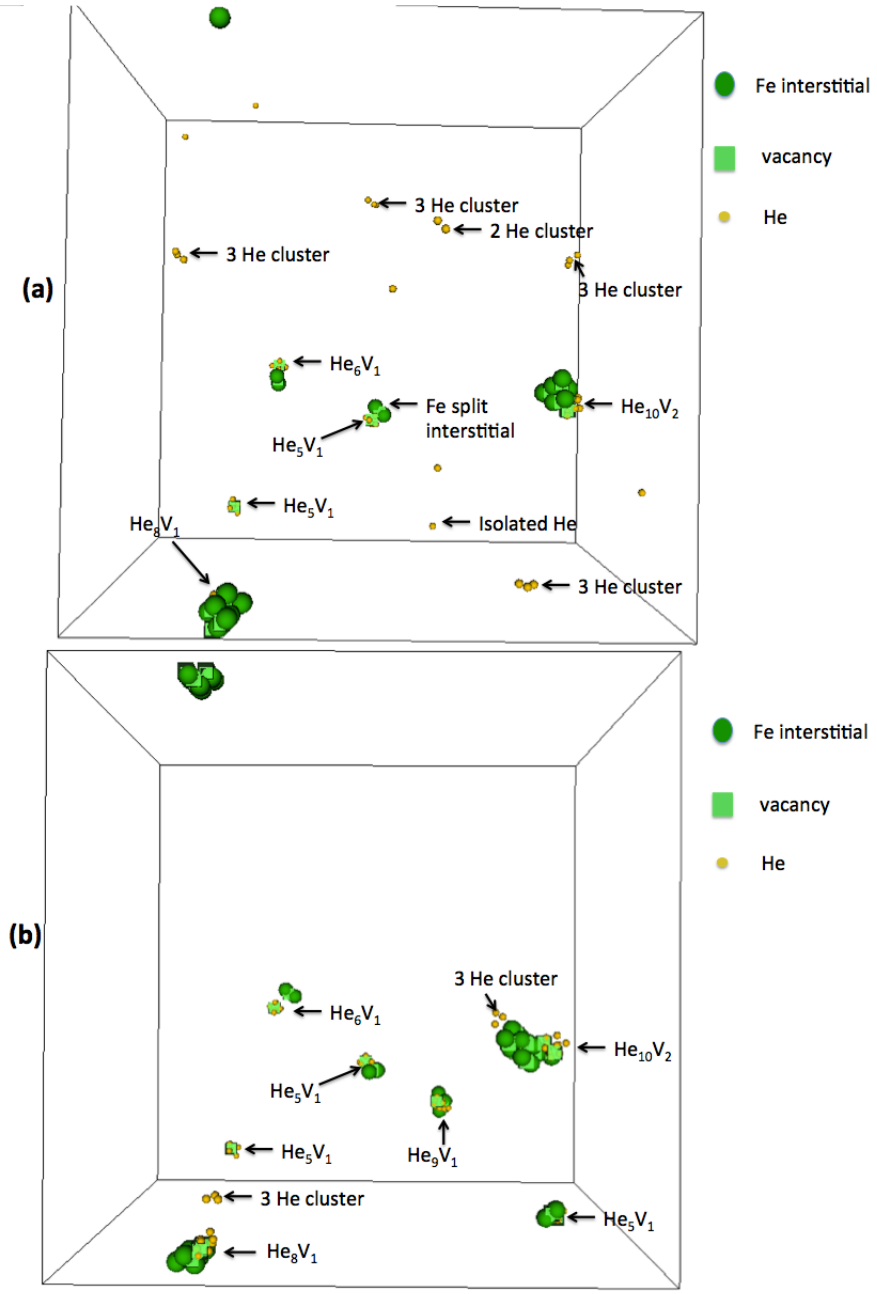

Figure 3.15: The MD simulation of the bcc Fe system at 500 K with randomly distributed He (0.1 % concentration) after (a) 1 ns and (b) 5 ns.

an He cluster with an associated vacancy. We can see the helium clusters with a size bigger than 3 can evolve into the helium bubbles. As found by Yang *et al.*, after a trap mutation process happened, the configuration becomes stabilised.

The resultant isolated He and small He clusters diffuse to form large clusters or bubbles. Larger He complexes form by 5 ns. e.g. there is an $He_{10}V_2$ complex in Figure 3.15 (a) and Figure 3.15 (b). In addition, we can see Fe split interstitials around He_5V_1 and He_6V_1 in (a) and (b) of Figure 3.15.

We also find the concentration of the helium in the Fe system plays a non-negligible role on the formation of the He clusters and bubbles. As the concentration increases, large He bubbles (containing more than 10 He and multiple vacancies) appear within 1 ns (see Figure 3.16).

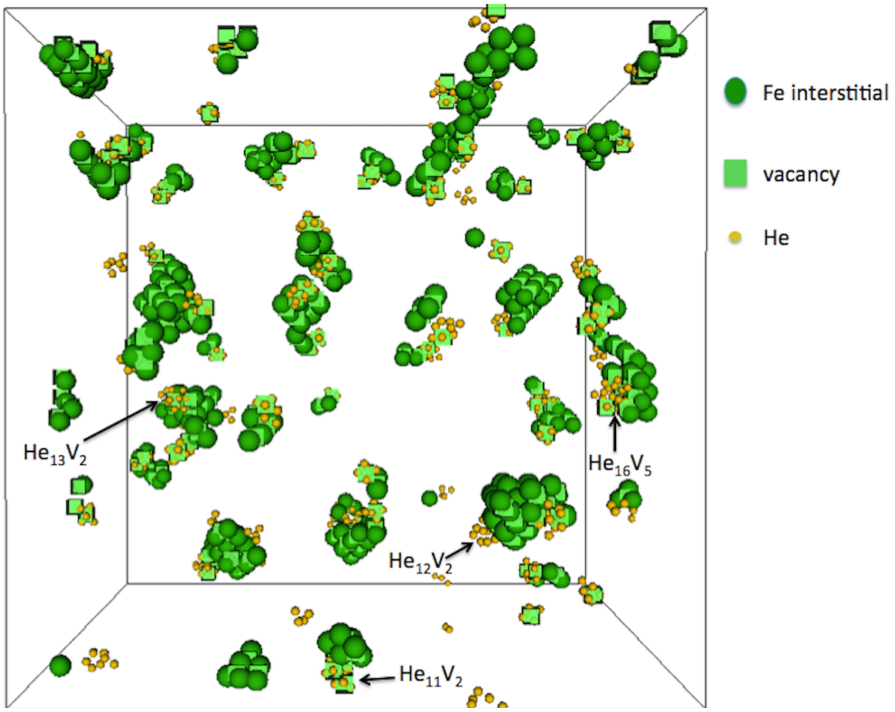

Figure 3.16: The MD simulation of the bcc Fe system at 500 K with randomly distributed He (1% concentration) at 1 ns.

The energy barrier for a single interstitial helium to diffuse is calculated as 0.06 eV. This shows that single helium is highly mobile at 500 K. Interstitial He diffusion occurs along the pathway from one tetrahedral site to its neighbouring tetrahedral site (shown in Figure 3.17).

In fact, by calculating the formation energy, single helium prefers to be substitutional rather than interstitial, but this require that the vacancy is prepared for He to be substitutional so that the He atom will instantly fall into the site since the energy barrier for an helium interstitial to occupy the site, emitting an Fe dumbbell is 6.76 eV as shown in Table 3.4. Thus an isolated He produced by a nuclear reaction would actually form as a tetrahedral interstitial in the first instance.

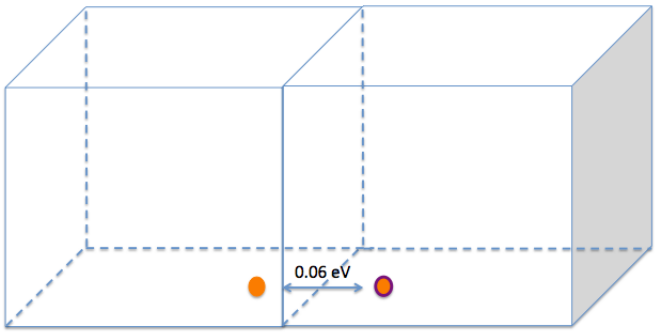

Figure 3.17: The diffusion of an He tetrahedral interstitial in the bcc Fe system. The orange sphere represents the He atom in the initial state. The purple outline indicts the configuration after transition.

The He complexes that form from clustering at 500 K contain fewer vacancies than the He bubbles whose energies are plotted in Figure 3.4. For these bubble sizes that are optimum at 0 K, larger energy barriers need to be overcome to form them. This point is discussed in more details in the next section.

Typical energy barrier (eV)	He	He_2	He_3	He_4	He_5
To diffuse	0.06	0.12	0.2	0.48	-
To take over one vacancy with ejecting an Fe interstitial	6.76	5.65	4.52	0.3	0

Table 3.4: The typical energy barrier for He clusters to diffuse, to eject an Fe atom into an interstitial site and to take over one vacancy.

The energy barriers of some typical transitions observed in the MD simulations have been calculated and these are summarised in Table 3.4. 0 eV implies the event takes place directly after the minimisation of the configuration. Diffusion of He clusters is found for clusters containing 2-4 He, but the mobility of the cluster reduces as the size increases.

The diffusion of the He_2 cluster is shown in Figure 3.18. These diffusion events of the He_2 cluster are found by the saddle searches and the barriers are checked with the NEB method.

Figure 3.18: The diagram to show the diffusion of the cluster of 2 He with an energy barrier of 0.12 eV in $< 110 >$ direction and rotation with 0.09 eV in bcc Fe system. The orange sphere represents the He atom in the initial state. The purple outline indicts the final state after transition.

When the size reaches 5 He, an Fe atom displaces into an interstitial position and the cluster becomes pinned. The displacement of an Fe atom can also happen for the cluster of 4 He but recombination can also occur. The typical energy barrier for this is 0.3 eV (i.e. the time scale for a hop at 500 K is about 110 ps) as shown in Figure 3.19. Having attained the shared vacancy position, the cluster can evolve further by forming a split interstitial with an energy barrier of 0.55 eV. The two-stage reverse process needs to overcome barriers of 0.4 eV and 0.013 eV respectively (see Figure 3.19). This phenomenon of Fe ejection observed in MD simulation was never observed for clusters of size < 4 since the energy barriers are too high (see Table 3.4).

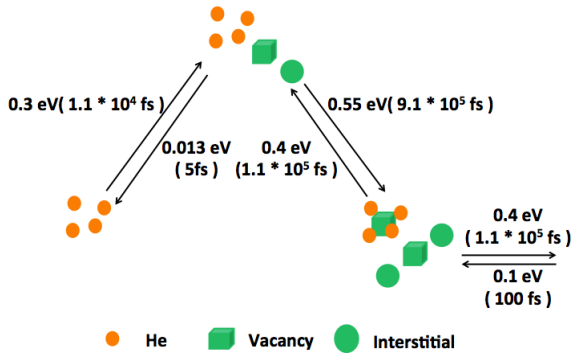

Figure 3.19: Typical transitions for He_4 at 500 K.

As noted, the He_5 clusters can spontaneously eject an Fe atom into an interstitial position

(see Figure 3.20). This shows the vacancy-free cluster is no longer the lowest energy state. Different from the situation for the He_4 cluster, it needs only 0.13 eV (i.e. the time scale for a hop at 500 K is about 2 ps) to take over this vacancy and form an Fe split interstitial. On the other hand, the energy barrier for the Fe interstitial to recombine back into the cluster is 0.4 eV, which is larger than the barrier to diffuse in the Fe lattice. (i.e. the time scale for a hop at 500 K is about 1.1 ns), which implies that the He_5 cluster prefers to evolve into an He bubble. When an He_5 cluster has created a vacancy and a split interstitial, the He_5V_1 system is observed to be stable over MD time scales and the cluster of 5 He atoms becomes the seed point of He bubble formation at 500 K.

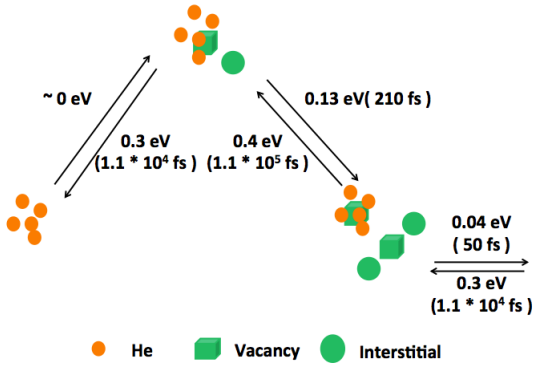

Figure 3.20: Typical transitions for He_5 at 500 K.

The binding energy $E_{binding}$ of the small clusters was also calculated as defined below, in order to study the stability of these clusters.

$$E_{binding} = E_{system} - E_{Fe} \cdot N_{Fe} - E_{He} \cdot N_{He}, \tag{3.4}$$

where E_{He} is the formation energy of a helium tetrahedral interstitial and E_{Fe} is the cohesive energy of Fe, N_{Fe} and N_{He} is the number of Fe and He atoms in the system.

The binding energies of the smallest He clusters are shown in Table 3.5.

	He_2	He_3	He_4	He_5
Binding Energy per He atom	-0.125 eV	-0.236 eV	-0.317 eV	-0.37 eV

Table 3.5: The binding energy of the He clusters for the lowest energy configurations

The negative value means that it is energetically favourable for helium to be in the cluster rather than stay isolated. The increasing binding energy per He atom shows stronger stability for larger He clusters. The small binding energy for the He_2 cluster and He_3 cluster implies the possibility of separation and thus we have examined the migration barriers for the separation of the small He clusters (see Table 3.6).

Separation	He_2	He_3	He_4
$He + He$	0.3 eV		
$He + He_2$		0.48 eV	
$He + He_3$			0.6 eV

Table 3.6: The energy barrier for the small He clusters to separate

He interstitials can amalgamate into the small clusters (< 4 He) in different ways. All of the barriers calculated were less than 0.2 eV, thus indicating that it is kinetically favourable for the small He clusters to remain intact rather than separate. However, separation is also possible at 500 K over MD time scales.

3.7 Helium Bubble Growth

3.7.1 Collision Cascades

To study radiation damage, collision cascades simulations are carried out by imparting an atom usually called the Primary Knock-on Atom (PKA) with a given kinetic energy in a certain direction. The system is then evolved using MD.

The system is first thermalised before a cascade event is initiated. We choose a value of 500 K for the system temperature. After that a cascade is initiated near a bubble, by imparting 1 keV energy to a PKA. 1 keV is chosen because it is sufficiently large to cause well separated vacancies and interstitials and generate good statistics but not so large that the computations become infeasible.

To analyse the results of cascade simulations it is necessary to define an interaction region close to the bubble. We arbitrarily take this as a shell around the bubble up to the sixth

nearest neighbour distance in the perfect bcc lattice. If an Fe vacancy or interstitial is created in this region, the cascade is defined as having interacted with the bubble. Figure 3.21 illustrates this idea.

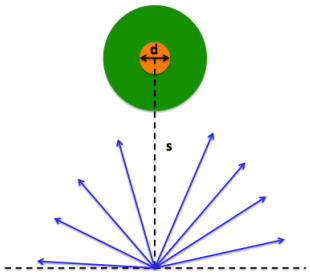

Figure 3.21: The red region represents the He bubble and the green region defines the volume where we are interested in observing damage. d is the diameter of the bubble, s is the distance between the centre of the bubble and the position of the primary knock-on atom (PKA). The trajectories of the cascades are chosen over the half sphere.

The probability of the cascade to cause damage in the interaction region is dependent on three factors: d, s and the direction of the cascade. For each chosen value of s and each bubble size, 8000 1 keV collision cascades were initiated in order to generate good statistics.

To investigate the mechanism by which an He bubble may be enlarged, we examine the increase/decrease in Fe vacancies in the bubble by averaging over all generated cascades. In this section, we compare the two interatomic potentials defined in Section 2.1.3.

The procedure is shown in Figures 3.22 and 3.23 with some typical positions and directions of the cascades for three different sizes of He bubble. Figures 3.22 and 3.23 also gives the cone angle within which the generated cascades will cause defects to form in the bubble interaction region with a probability of 98%.

It can be seen that for the larger bubbles, no interaction with the cascade will occur if the PKA is generated more than 6 nm from the bubble. For the small bubble this distance drops to 4.4 nm. By targeting the trajectories within the cones, statistics can be obtained without the necessity for lots of redundant trajectory calculations which produce no damage near the bubble.

Calculations were performed using both potentials and these showed consistent results

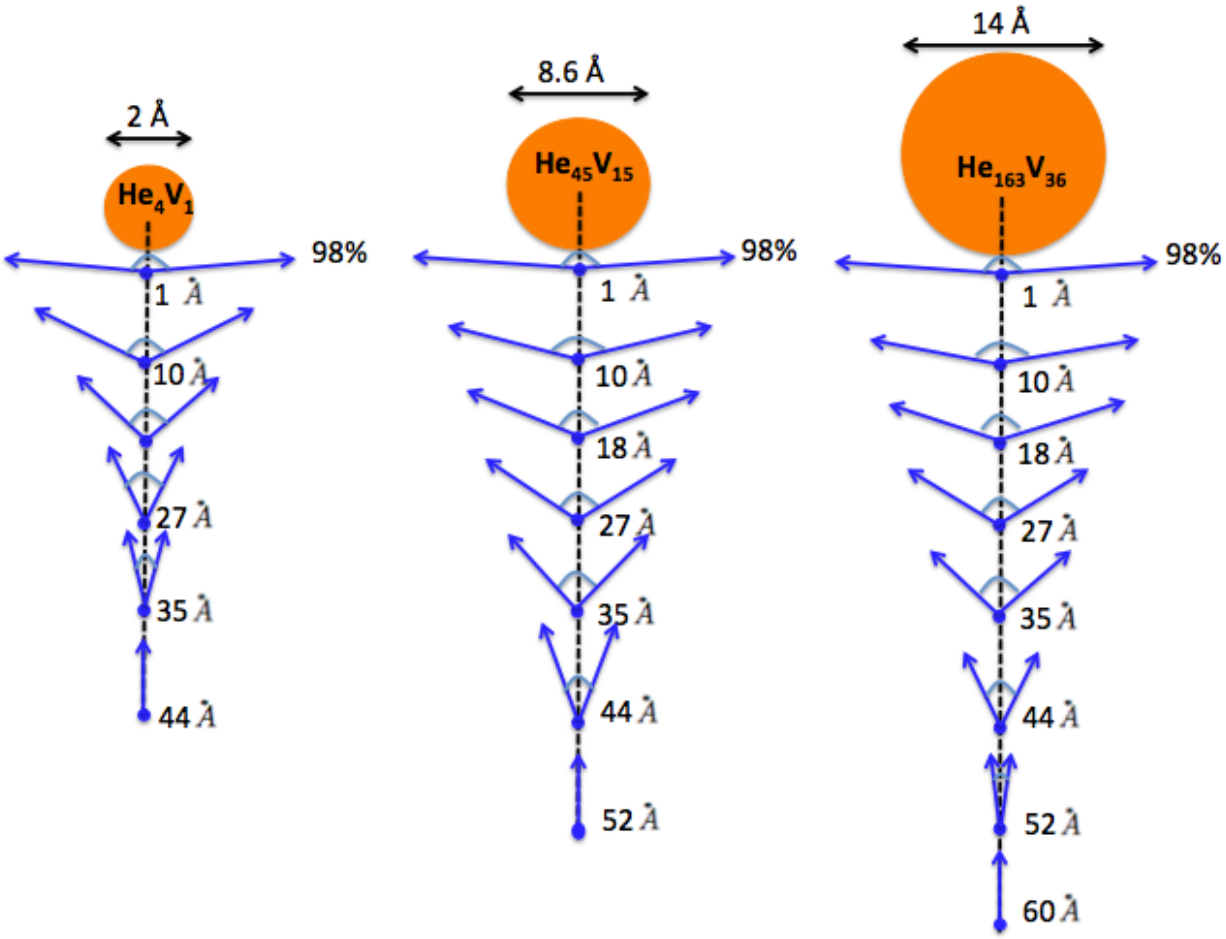

Figure 3.22: Gao's potential: Representations of the cones for collision cascades that have a 98% probability of interacting with the helium bubble. Different lines represent the cone angle as a function of separation and bubble size.

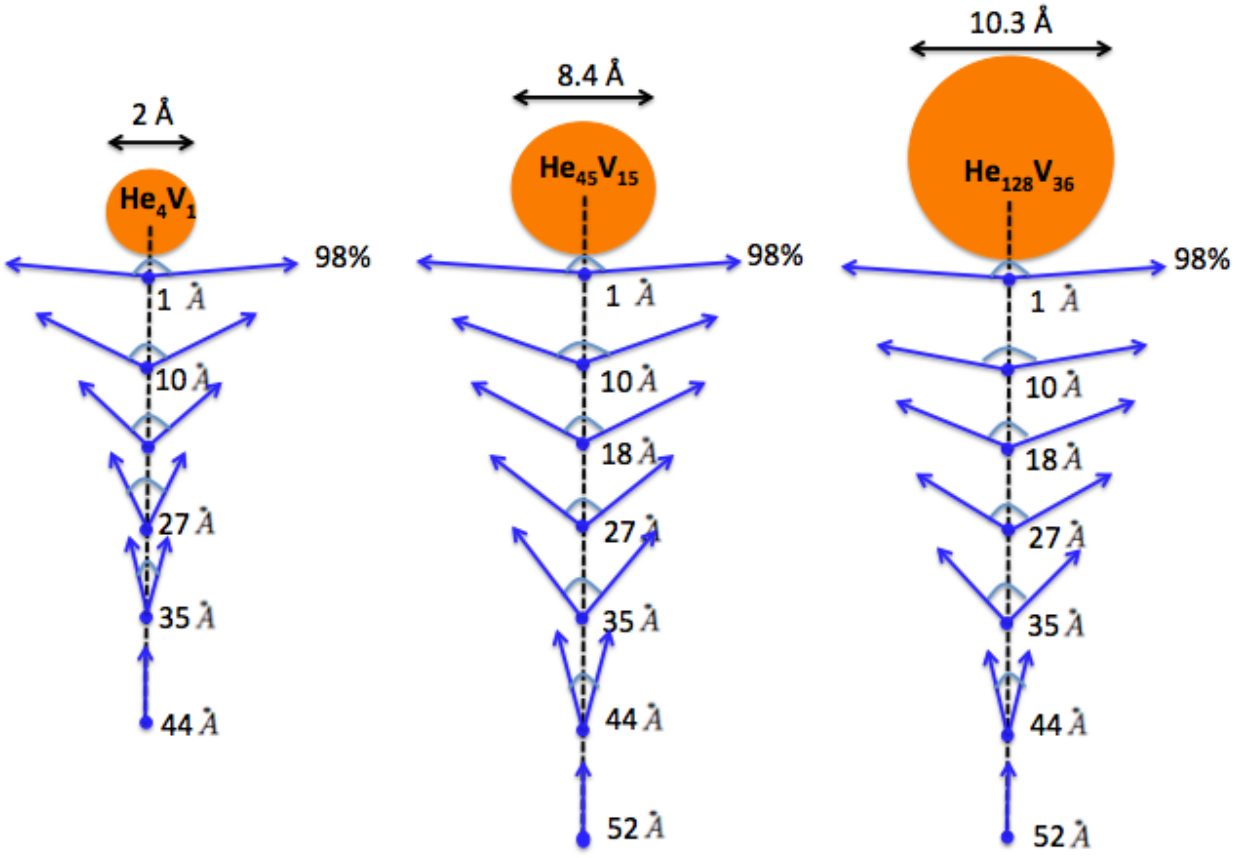

Figure 3.23: Stoller's potential: Representations of the cones for collision cascades that have a 98% probability of interacting with the helium bubble. Different lines represent the cone angle as a function of separation and bubble size.

for the interactions between bubbles and cascades.

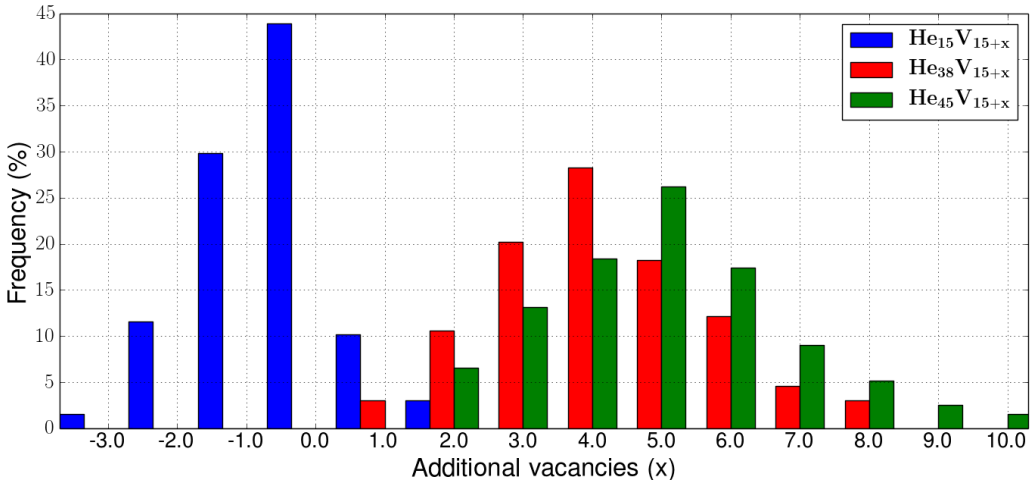

Figure 3.24: Gao's potential: Frequency of capture/loss of vacancies during the collision cascade for a system containing 15 vacancies. The three sets of results show three cases of (1) below the ideal He-to-vacancy ratio, (2) at the optimal (from Figure 3.4) ratio and (3) above the ideal ratio.

Figures 3.24 and 3.25 show how the number of vacancies in the cluster changes, for the three sizes of He-vacancy clusters, where the initial number of vacancies is kept constant at 15. As might be expected, at a low He-to-vacancy ratio, emission of vacancies is clearly favoured. This changes at the optimal (from Figure 3.4) He-to-vacancy ratio, where the bubble absorbs vacancies. Above the optimal (from Figure 3.4) ratio, vacancy capture becomes more favoured. Figure 3.26 shows a typical example of the processes which occur in a typical collision cascade. Therefore, radiation provides a process for an He bubble to be enlarged by attracting vacancies or emitting Fe interstitials. As might be expected, both Fe-He potentials demonstrate this conclusion with the Gao potential, showing the effect more strongly than the Stoller's potential.

3.7.2 Energy barriers for isolated He to join an existing bubble

Considering the behaviour of helium bubbles under radiation damage and the formation energy of bubbles, we decided to use Gao's potential to investigate the details of the various mechanisms involved.

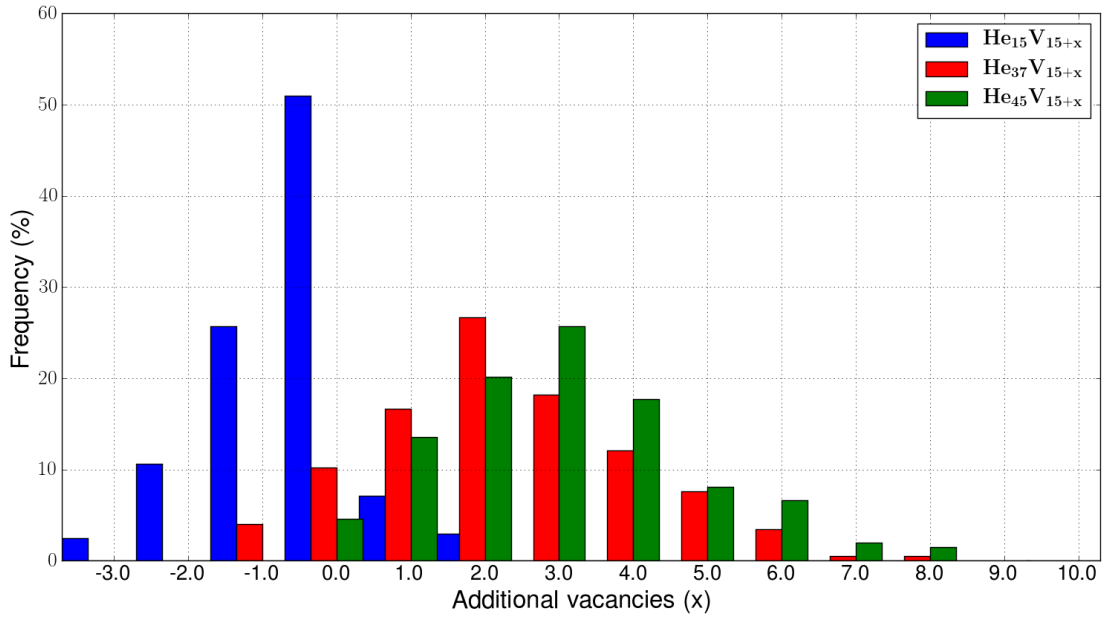

Figure 3.25: Stoller's potential: Frequency of capture/loss of vacancies during the collision cascade for a system containing 15 vacancies. The three sets of results show three cases of (1) below the ideal He-to-vacancy ratio, (2) at the optimal (from Figure 3.4) ratio and (3) above the ideal ratio.

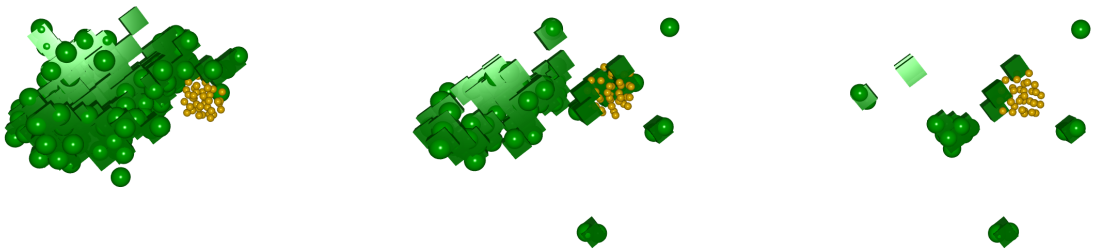

Figure 3.26: Gao's potential: Three frames in the MD simulation of a collision cascade near an $He_{38}V_{15}$ complex. The left image is after 100 fs, just as the cascade reaches the bubble; the centre image is after 1200 fs when the cascade has passed into the bubble and the right figure is the state after 10 ps, which shows the vacancies (green cubes in the figure) absorbed by the He bubble (the small yellow spheres). Split Fe interstitials can also be observed.

In order to gain an understanding of He accumulation into bubbles, a study was carried out to investigate the energetics of the barriers for He to diffuse into or outwards from an existing bubble from an interstitial site near an existing bubble. To achieve that, we classified He interstitials according to the distance between the interstitial and the surface of a bubble as given in Table 3.7. For each position, at least 20 different positions of interstitials are investigated and 4000 saddle point searches are carried out.

Neighbour (N)	1	2	3	4	5	6
Distance Å	1.0-1.9	1.9-2.8	2.8-3.5	3.5-4.2	4.2-5.1	5.1-6.0

Table 3.7: Classification of He interstitials with respect to the distance from an He bubble.

The average migration energy barriers were calculated for the He interstitials diffusing towards He bubbles of different sizes. The initial positions of the interstitial He atoms were varied from 1 to 6 nearest neighbour (N) distance from the edge of the bubble and the summarised data is presented in Table 3.8.

Typically, He interstitial jumps occur to adjacent N positions, e.g. if an He interstitial is initially positioned at 6N, then diffusion occurs by jumping to 5N, then from 5N to 4N and so on, until from 1N the He interstitial joins the bubble configuration. Therefore in Table 3.8 we give migration barriers for jumping to adjacent N position in the direction towards the bubble.

A barrier of 0 eV accounts for the cases when He interstitials instantaneously join the He bubble, during equilibration (i.e. the barrier is less than 0.01 eV). It usually occurs in the systems which consist of He bubbles which have a fairly low He-to-vacancy ratio (typically less than $3:1$). This suggests that bubbles with a low He-to-vacancy ratio have a strong tendency to attract He interstitials that are in their vicinities.

An opposite behaviour was also observed for the cases of bubbles with a high He-to-vacancy ratio ($\geq 4:1$). As can be seen in Table 3.8, with a growing He-to-vacancy ratio the migration barrier heights to jump towards a bubble increase, suggesting a loss of attraction to He interstitials. To investigate this effect and to complement the previous results, a similar

Typical energy barrier (eV)	Diameter (Å)	1 N	2 N	3 N	4 N	5 N	6 N
He_nV_5 ($n < 20$)	<6.3	0	0	0	0	0	0
$He_{20}V_5$	6.5	0	0	0	0.05	0.06	0.09
He_nV_9 ($n < 27$)	<7.5	0	0	0	0	0	0
$He_{27}V_9$	7.6	0	0	0	0	0	0.019
$He_{36}V_9$	8.4	0.004	0.006	0.016	0.04	0.06	0.08
He_nV_{15} ($n < 30$)	<7.6	0	0	0	0	0	0
$He_{30}V_{15}$	7.8	0	0	0	0.02	0.055	0.033
$He_{38}V_{15}$	8.0	0	0	0.03	0.018	0.1	0.099
$He_{45}V_{15}$	8.6	0	0.031	0.035	0.048	0.13	0.126
$He_{60}V_{15}$	9.8	0.006	0.02	0.087	0.087	0.08	0.08
He_nV_{25} ($n < 50$)	<7.8	0	0	0	0	0	0
$He_{50}V_{25}$	7.9	0	0	0.04	0.039	0.044	0.047
$He_{75}V_{25}$	8.8	0	0	0.013	0.027	0.034	0.10
$He_{98}V_{25}$	10.4	0.012	0.02	0.094	0.362	0.056	0.046
$He_{100}V_{25}$	10.4	0.016	0.12	0.132	0.27	0.21	0.18
He_nV_{36} ($n < 72$)	<10.2	0	0	0	0	0	0
$He_{72}V_{36}$	10.3	0	0	0.005	0.013	0.013	0.051
$He_{108}V_{36}$	11.4	0	0	0.004	0.039	0.036	0.017
$He_{144}V_{36}$	13	0	0	0.65	0.091	0.098	0.051
$He_{163}V_{36}$	14	0	0	2.54	1.6	0.27	0.1
$He_{98}V_{98}$	10.5	0	0.01	0.06	0.058	0.06	0.052
$He_{196}V_{98}$	12	0	0.029	0.07	0.024	0.023	0.02
$He_{294}V_{98}$	13.8	0	0.013	0.07	0.11	0.033	0.05
$He_{392}V_{98}$	16.2	0	1.62	0.71	0.3	0.15	0.047
$He_{169}V_{169}$	11	0	0.0065	0.01	0.046	0.06	0.05
$He_{338}V_{169}$	12.5	0	0.008	0.086	0.062	0.066	0.056
$He_{507}V_{169}$	16.5	0	0	1.70	0.33	0.170	0.036
$He_{676}V_{169}$	20	0	0	2.42	0.99	0.40	0.26

Table 3.8: A summary of migration barriers (eV) of He interstitials diffusing towards He bubbles of different configuration. The first column specifies the bubble size, where the following columns represent the initial He interstitial position as specified in Table 3.7.

study was performed by checking the migration barriers of He interstitials in the direction away from the bubble. This is summarised in Table 3.9.

Typical energy barrier (eV)	1 N	2 N	3 N	4 N	5 N	6 N
$He_{27}V_9$	-	-	-	-	-	2.109
$He_{36}V_9$	1.8	0.01	0.02	0.06	0.08	0.12
$He_{30}V_{15}$	-	-	-	1.9	0.061	0.041
$He_{38}V_{15}$	-	-	2.0	0.007	0.046	0.045
$He_{45}V_{15}$	-	2.2	0.01	0.001	0.064	0.052
$He_{60}V_{15}$	2.2	0.01	0.007	0.069	0.02	0.05
$He_{50}V_{25}$	-	-	2.74	0.041	0.068	0.051
$He_{75}V_{25}$	-	-	2.45	0.14	0.17	0.16
$He_{98}V_{25}$	2.96	0.13	0.127	0.007	0.015	0.016
$He_{100}V_{25}$	2.39	0.014	0.016	0.022	0.015	0.012
$He_{72}V_{36}$	-	-	2.2	0.008	0.019	0.076
$He_{108}V_{36}$	-	-	2.6	0.009	0.006	0.007
$He_{144}V_{36}$	-	-	0.11	0.025	0.07	0.04
$He_{163}V_{36}$	-	-	0.001	0.005	0.009	0.003
$He_{98}V_{98}$	-	3.4	0.09	0.064	0.062	0.061
$He_{196}V_{98}$	-	2.66	0.039	0.021	0.02	0.02
$He_{294}V_{98}$	-	2.645	0.045	0.018	0.025	0.026
$He_{392}V_{98}$	-	0.023	0.066	0.02	0.034	0.021
$He_{169}V_{169}$	-	3.53	0.03	0.056	0.065	0.06
$He_{338}V_{169}$	-	3.53	0.086	0.051	0.06	0.047
$He_{507}V_{169}$	-	-	0.027	0.012	0.014	0.007
$He_{676}V_{169}$	-	-	0.02	0.012	0.006	0.006

Table 3.9: A summary of migration barriers (eV) of He interstitials diffusing away from the He bubble. The first column specifies the bubble size and the following columns represent the initial He interstitial position as specified in Table 3.7.

He interstitials move from 1N to 2N, from 2N to 3N and so on as given in Table 3.9. The "-" accounts for the cases when no valid migration processes of He interstitials were observed because of instantaneously joining the bubble in these cases.

Table 3.9 also shows indications of a region around He bubble where an He atom is repulsed by a bubble by having a migration barrier to jump away from it lower than the barrier to jump towards the bubble. This is especially clear when bubbles have a high He-to-vacancy ratio ($\geq 4:1$).

The data also indicates that even though the bubbles may have a ratio above the optimal (from Figure 3.4) configuration, they still can be enlarged in size, since most of the barriers are only slightly higher compared to the He interstitial migration barrier in pure Fe. See, e.g. the $He_{38}V_{15}$ case. For the cases with a high ratio, the migration barrier to move away from the bubble is lower than the one to jump towards it, as in $He_{45}V_{15}$ case. Once the He interstitial joins into the bubble, it cannot leave the bubble because of the huge barrier. It is noticed that in Table 3.8, the barrier for $He_{36}V_9$ is higher than $He_{27}V_9$ but the ones for $He_{60}V_{15}$ is slightly lower than $He_{45}V_{15}$. This may well be due to the round off error during averaging the statistics of the calculations. As we only take the transition for He diffusion to the surface of the bubble into account, it may cause a bit of variation of the results. In any event the barriers in both the latter cases are so small that an He in the neighbourhood is likely to join the bubble.

If the bubbles are enlarged up to 25 vacancies, even with the optimal ratio or above, the additional He could still diffuse into the bubble but the maximum barrier here increases to 0.3 eV, which is more than 3 times of the one in bubbles containing 15 vacancies.

Further, if we investigate the bubbles with 36 vacancies, for the lower He-to-vacancy ratio ($< 2:1$), jumping into the bubble happens instantaneously for the He interstitial at 6th neighbour. For the bubbles with ratios between $2:1$ and $3:1$, it is kinetically favourable for additional He to join as the migration barrier is lower than the diffusion barrier in pure Fe. However, the barrier to jump away becomes lower than the barrier to jump in when the ratio is more than $3:1$. When the bubble attains a $4:1$ ratio, there is a big energy barrier for He to jump towards the bubble from the 3rd neighbour. This is even more clear when the bubble reaches the optimal (from Figure 3.4) configuration. In these cases, it is kinetically favourable for the He interstitial to stay outside the bubble. Similar conclusions can also be drawn for the larger He bubbles e.g. He_nV_{98} and He_nV_{169} in Tables 3.8 and 3.9. In the case of He_nV_{98}, only when the He-to-vacancy ratio is $1:1$, well below optimal (from Figure 3.4), is it more favourable for the He atom to diffuse towards the bubble than to diffuse away.

In summary, for the bubbles with the diameter $<\approx$ 11 Å, it is kinetically possible to absorb additional He, even when the He-to-vacancy ratio is above optimal (from Figure 3.4), but the He interstitial becomes less likely to jump towards the bubble when the diameter $>\approx$ 9 Å and the He-to-vacancy ratio $\geq 3:1$. Isolated He diffusion into bubbles with a diameter $>$ 13 Å and the He-to-vacancy ratio $> 4:1$ occurs only very infrequently at room temperature.

One of the reasons that the larger bubbles find it more difficult to absorb He is the strain and distortion introduced into the Fe lattice. We can calculate the volume of material around a bubble in which the Fe atoms are displaced from their lattice sites by using a Voronoi algorithm. If we (arbitrarily) calculate this region as the region in which the atoms are displaced by at least one third of the nearest neighbour distance, Figure 3.27 shows that this volume increases non-linearly with bubble size.

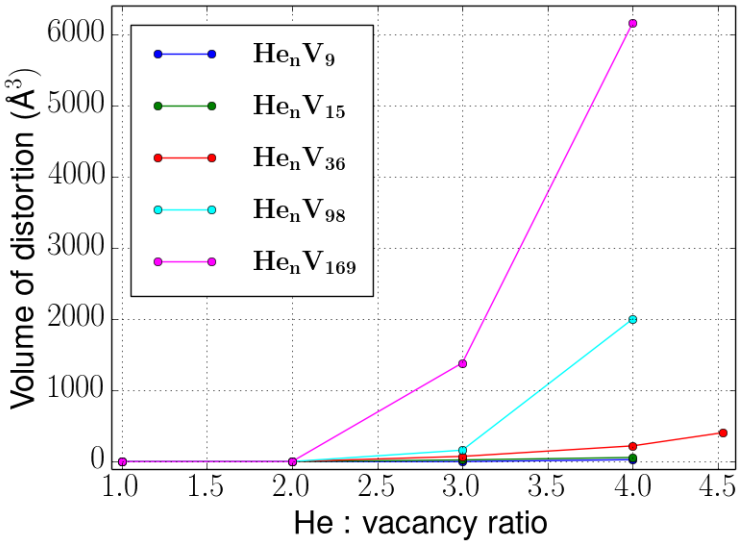

Figure 3.27: The volume of distortion as a function of the number of helium atoms for different sizes of He_nV_m clusters. For the $He_{163}V_{36}$ bubble, the volume of 400 Å^3 corresponds to an annular region around the bubble of between 2 and 3 Å in width.

Figure 3.28 shows the strained region for bubbles containing 36 vacancies. The region is not spherical in shape but as with Figure 3.27 it indicates that the strained region grows rapidly with increasing bubble size so there appears to be a direct correlation between the lat-

tice strain and the energy barriers for isolated He to diffuse into the bubble. This calculation is in agreement with the conclusion of Morishita's work [87].

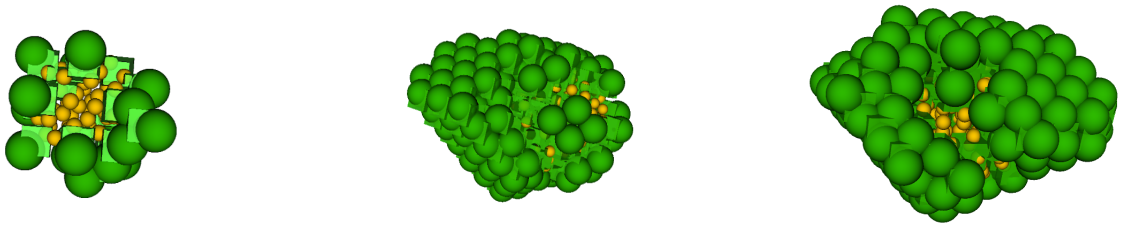

Figure 3.28: The distortion around the bubble $He_{60}V_{15}$, $He_{144}V_{36}$ and $He_{163}V_{36}$.

3.8 Conclusions

Single helium atoms prefer to be substitutional rather than interstitial but the energy barrier for this to occur is large. Thus an isolated He atom injected into a bcc Fe lattice would be expected to settle at a tetrahedral site. The He interstitial can diffuse quickly in the bcc Fe system with a pathway between adjacent tetrahedral sites. These highly mobile He interstitials lead to He clustering. He_n, $n = 1, 2, 3$ clusters are also mobile over MD time scales at 500 K but a cluster of 5 He can eject an Fe interstitial and become the seed point for less mobile bubbles. These less mobile bubbles can initially continue to grow through the attraction of He_n, $n = 1, 2, 3$ clusters. The optimal (from Figure 3.4) He-to-vacancy ratio has been determined and it has been shown how bubbles can also absorb additional vacancies produced by irradiation to reduce the lattice strain around the bubble, which would reduce the energy barriers and allow more He to join.

The energy barriers for a diffusing He atom to join an existing bubble have been shown to increase rapidly as the size of the bubble increases and the strained region around the bubble increases in size. Thus the Ostwald ripening process becomes kinetically limited as the size of the bubble grows. These results are in good agreement with experimental work [73] in pure Fe which show that bubbles of between 1 and 2 nm in diameter are preferentially formed at room temperature.

Chapter 4

Argon Bubble Formation and Growth in bcc Fe

4.1 Introduction

In this chapter argon bubbles in bcc Fe are studied using the same methodology as in Chapter 3 with He. Before discussing the modelling, a review of a few experimental papers is presented.

Microstructural evolution of P92 ferritic/martensitic steel irradiated by Ar^+ ion beams at doses from 0.6 to 230 displacements per atom (dpa) at room temperature was investigated with a conventional transmission electron microscope technique by Jin *et al.* [99]. They showed that the carbide particles became partly amorphous at an irradiation dose of 2.3 dpa and were almost completely amorphous at the dose of 11.5 dpa. With the irradiation dose increasing, the irradiation induced segregation and depletion became more severe, which would influence the mechanical properties of the steel.

Klimenkov [100] presents the results of a quantitative evaluation of Ar gas inside nano-bubbles formed during the preparation of ODS steel. The investigated bubbles with sizes from 4-5 nm to 38 nm show a good stability in the thin TEM foil (see Figure 4.1). It was

found that the Ar concentration inside the bubbles decreases with the increasing bubble size. Below 1373 K the bubbles remain very stable, as they retain Ar inside during TEM investigations. Other materials have also shown that Ar bubbles can form.

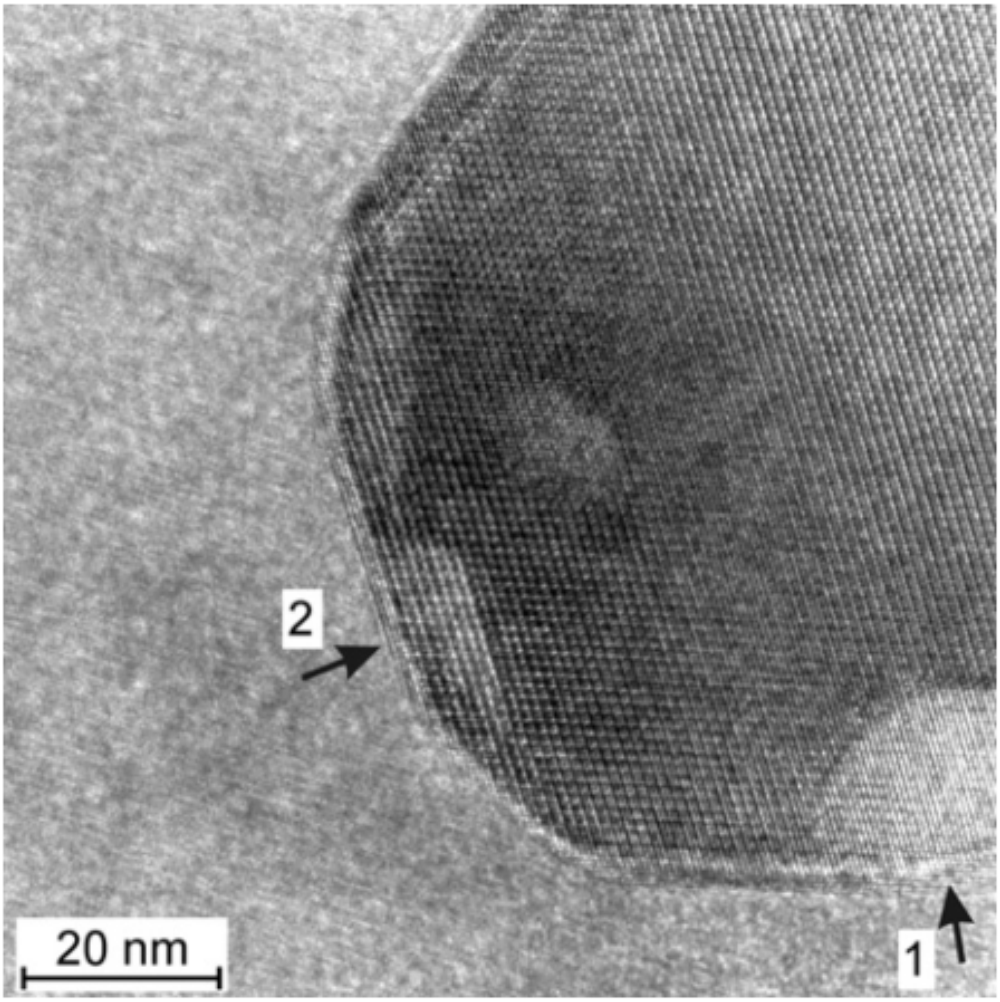

Figure 4.1: HRTEM micrograph of an ODS particle with marked Ar bubbles. The image is taken from 4.1. The larger bubbles normally have a spherical or semi-spherical shape (arrow 1), whereas the small bubbles often exhibit a faceted shape (arrow 2). This image indicates that an ODS particle may have two or even more Ar bubbles at the interface.

Tyagi, Nandedkar and Krishan [101] investigated helium and argon ion damage in metallic glasses at room temperature. In the case of argon irradiation, blisters disappear at high doses, flaking was not observed and sputtering seemed to be the main process of surface erosion. In contrast, blistering and flaking was found due to helium irradiation. Argon bubbles were nearly 5 to 10 times the size of helium bubbles (The diameters of He bubbles range from 20

- 50 Å, whereas Ar bubbles vary from 100 - 500 Å).

Sakamoto *et al.* [102] have investigated Ar ion irradiation effects on the physical properties of Au/Fe multilayers (MLs). The Au/Fe MLs prepared in the different batches under the same condition show different physical properties, which have been observed by conversion electron Mössbauer spectroscopy (CEMS). The 400 keV Ar ion irradiation at the dose of $3 \times 10^{13} - 2.56 \times 10^{16}$ ions/cm^2 induces a change of the magnetic and structural properties of the Au/Fe MLs, depending on the as-deposited state and the ion dose. They conclude that the Ar ion irradiation induces an atomic mixture at the layer boundaries and causes further breaks of Fe layers, resulting in the change in the magnetic properties being detected sensitively by the CEMS.

Swijgenhoven *et al.* [9] deal with the observation of surface and subsurface damage of Metglas 2826 MB ($Fe_{38}Ni_{40}Mo_4B_{18}$) during 5 keV Ar^+-ion bombardment at room temperature. They have shown that argon gas bubbles with a diameter between 2 nm and 4 nm can form in an amorphous alloy. Once a bubble nucleus is formed, it will grow further by capturing argon atoms and additional vacancies. The presence of gas bubbles in the surface layer results in macroscopic deformation of the surface.

From the experimental references, we could deduce that argon atoms tend to form larger bubbles than helium during irradiation but with more limited experimental data than for He. In this chapter, the results of a study both on the statics of small argon-vacancy clusters in bcc iron and their interaction with nearby collision cascades are presented, which will provide insight into how an argon bubble forms and grows. We also investigate the energy barriers that need to be overcome before growth by diffusion can occur.

4.2 Potential

For simulating the argon-vacancy clusters in the bcc iron system, we use the Lennard-Jones potential for the Ar-Ar interaction, ZBL potential for Ar-Fe and the same Ackland-Mendelev

potential used in helium-vacancy cluster in bcc Fe system for Fe-Fe here (see Section 2.1.3).

4.3 Formation Energy

The formation energy of the argon-vacancy clusters Ar_nV_m is calculated using the Monte Carlo algorithm, which was introduced in Section 3.3. First, we calculate the formation energy of several defects in the system. The calculation implies the argon atom is energetically favourable to be located in the substitutional site while the tetrahedral interstitial is more stable than the octahedral. Further, different from He in bcc Fe, an Ar substitutional atom is stable with an Fe dumbbell interstitial in the vicinity.

Fe cohesive energy	vacancy formation energy	Ar substitutional formation energy	Ar tetrahedral formation energy	Ar octahedral formation energy
4.013 eV	1.72 eV	12.20 eV	16.82 eV	17.61 eV

Table 4.1: The formation energy of defects for Ar in bcc Fe.

Figure 4.2 shows the formation energy of the Ar_nV_m clusters at 0 K from Equations 3.1, 3.2 and 3.3. Each curve is with the fixed number of vacancies, which implies that all the bubbles locating on the same curve have preformed vacancies before the Ar is inserted. To ensure the results can be compared on a similar scale, the figure shows the formation energy per vacancy. It is clear that there is an optimal (lowest formation energy per vacancy) Ar-to-vacancy ratio for each curve (calculated with a fixed number of vacancies). The optimum bubble size is given by the minima on the curves in Figure 4.2. It can be seen that the optimum ratio is always around 1 : 1 ratio, which is different from the optimal ratio found for helium. Further, each curve stops at the final point because the bubble will be no longer stable to hold more argon with the given number of vacancies; in other words, adding extra argon will cause the bubble to push the neighbouring Fe atoms into interstitials thus adding more vacancies into the bubble. This is shown schematically for the 5 vacancy case in Figure 4.3.

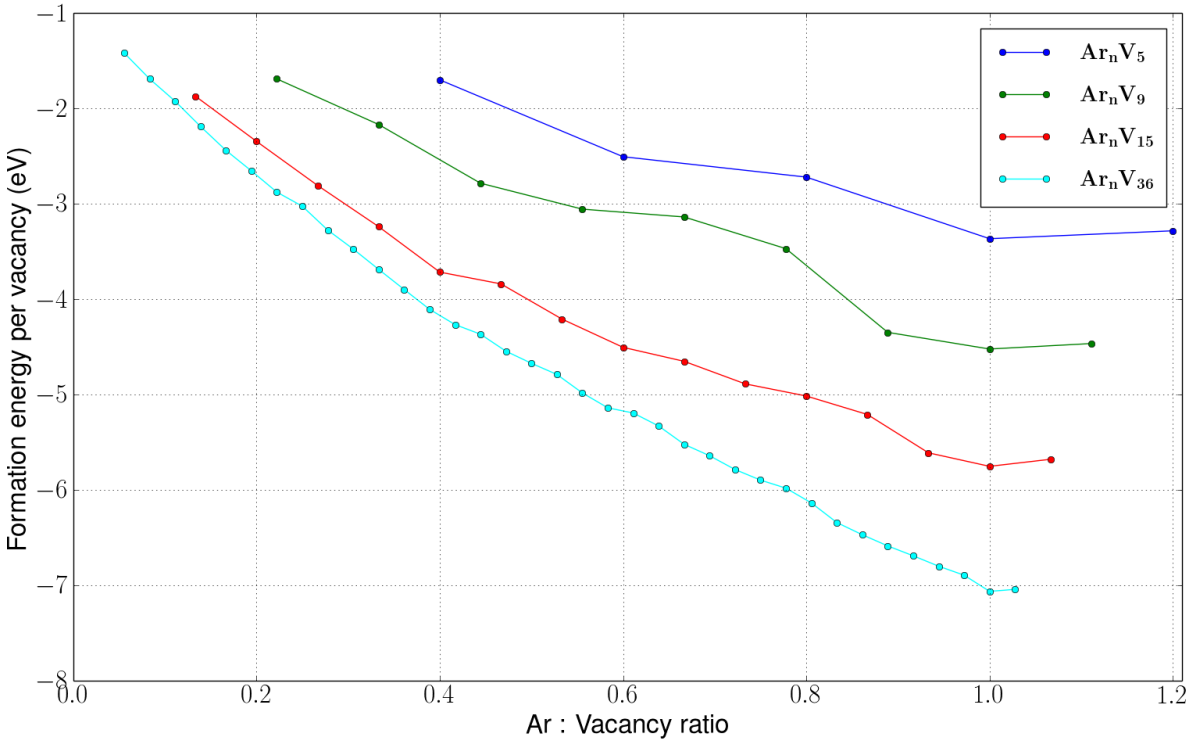

Figure 4.2: The formation energy as a function of the number of argon atoms for different sizes of Ar_nV_m clusters.

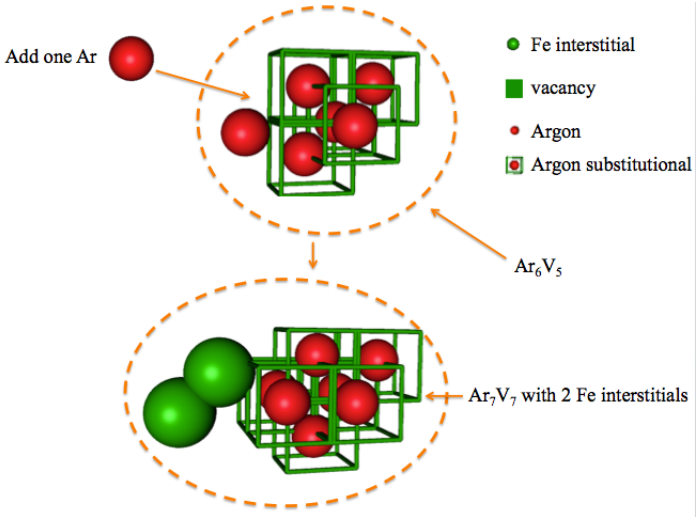

Figure 4.3: Illustration of the effect of adding an Ar atom to an Ar_6V_5 bubble.

4.4 Argon clustering and Bubble Formation

4.4.1 Random inserted Ar in bcc Fe

To investigate how argon atoms can form clusters or bubbles, first we randomly distribute argon interstitials into a pure bcc Fe system and evolve the system using MD, which is the same process as done for He in Chapter 3.3. Different concentrations of argon atoms are selected for comparison. The temperature of the system is set at 500K. The system is then evolved for up to 5 ns.

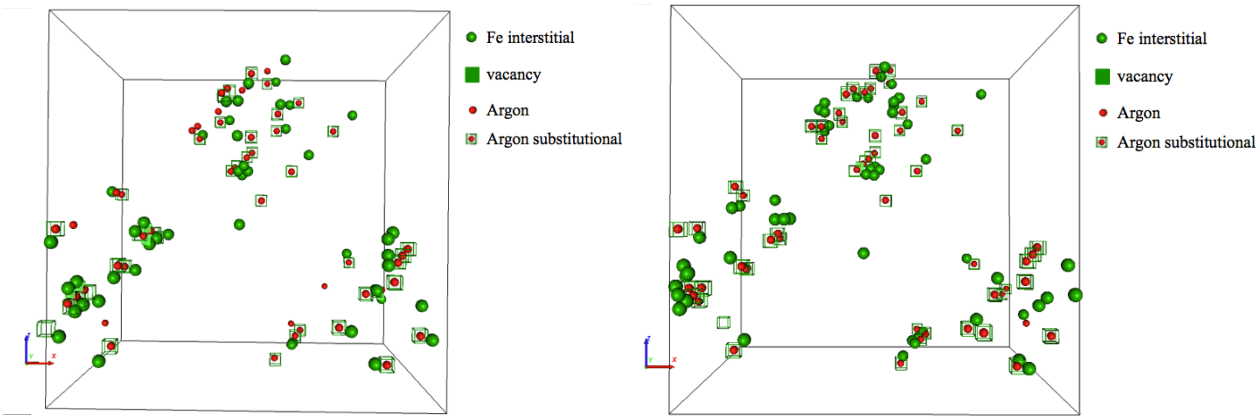

(a) (b)

Figure 4.4: The MD simulation of the bcc Fe system with randomly distributed Ar (0.1 % concentration) at (a) 10 ps and (b) 1 ns.

From Figure 4.4, we can see that there are no isolated interstitials but a large number of substitutional Ar and some small Ar clusters after one nanosecond. The trap mutation process dominates the movement of Ar atoms. The resulting configuration becomes stable over a nanosecond time scale at 500 K. No diffusion of Ar substitutionals into neighbour units has been found.

The energy barrier for a single argon interstitial to diffuse is calculated as 0.3 eV (shown in Figure 4.5). This shows that single argon is not especially mobile at 500 K compared to He. Diffusion occurs along the pathway from one tetrahedral site to its neighbouring tetrahedral site. In fact, from Table 4.1, single argon prefers to be substitutional rather than

interstitial and since the energy barrier for one argon interstitial to occupy the site of an Fe atom emitting an Fe dumbbell is only 0.07 eV but the reverse barrier is up to 1.4 eV. An isolated Ar interstitial would become a substitutional within MD time scales. After turning into substitutional, it is unlikely to move back to interstitial. The Fe dumbbell is favoured to be bound by the Ar substitutional atom in the its first neighbour (see Figure 4.6), with the energy barriers for the dumbbell to diffuse away, being larger than the reverse barrier.

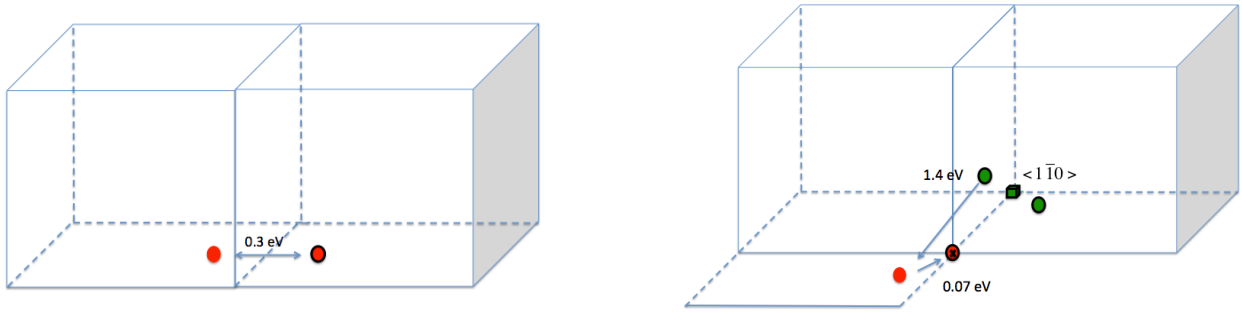

(a) (b)

Figure 4.5: The diagram to show the diffusion from the Ar tetrahedral site in bcc Fe system. The red sphere represents the Ar. The black outline shows the configuration after transition. The green sphere is the Fe interstitial and the green cube is the Fe vacancy. The cross sign inside indicts the substitutional atom. (a) The transition of the Ar tetrahedral interstitial to its neighbouring tetrahedral site with the forward and reverse barrier of 0.3 eV. (b) The transition of the Ar tetrahedral interstitial to the Ar substitutional with the $<1\bar{1}0>$ Fe dumbbell interstitial with the energy barrier of 0.07 eV and the reverse barrier of 1.4 eV.

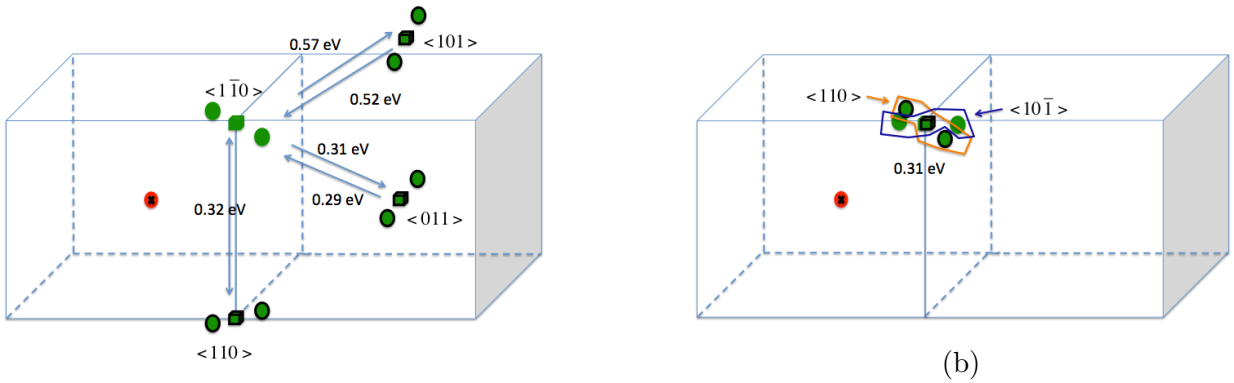

(a) (b)

Figure 4.6: Illustration of (a) the diffusion and (b) the reorientation of the Fe dumbbell interstitial with the Ar substitutional atom. The red sphere represents the Ar. The black outline shows the configuration after transition. The green sphere is the Fe interstitial and the green cube is the Fe vacancy. The cross sign inside indicts the substitutional atom.

4.4.2 Ar substitutional in bcc Fe

In this section, all the transition barriers and end states were calculated by saddle point searches from the initial state without any assumption about the final state.

4.4.2.1 Ar substitutional with a vacancy nearby

In order to diffuse, an Ar substitutional atom has to become interstitial. However the barriers for these events are high. It is therefore instructive to see what happens in the presence of a nearby vacancy. After minimisation, the Ar substitutional atom is not stable with the vacancy located in the first neighbour. It will instantaneously turn into the Ar split vacancy shape (i.e. 2 vacancies in each other's first neighbour with Ar sitting in the middle of them), which is different from He since the He substitutional atom is stable with a vacancy in the first neighbour (see Figure 3.13). The free vacancy is favoured to migrate towards the Ar atom (see Figures 4.7a and 4.7b). Once the vacancy comes to the second neighbour, a swap between this vacancy and substitutional will appear with a much smaller barrier than He in bcc Fe (see Figure 4.7c). Then it can evolve into the split vacancy configuration (see Figure 4.7d) or it can directly form it with the vacancy moving from the further neighbour such as the 4th neighbour as shown in Figure 4.7e. It was found that the split vacancy configuration can diffuse with a high barrier at 1.89 eV (see Figure 4.7f).

4.4.2.2 Ar substitutional with two vacancies nearby

An Ar substitutional atom with two neighbouring vacancies has also been investigated. Some typical transitions are shown in Figure 4.8. The lowest energy configuration that the Ar and two vacancies tend to form is an Ar_1V_3 cluster which is an isosceles triangle consisting of 3 vacancies with one sitting in first neighbour of the other two and the remaining two as second neighbours with the Ar in the centre of the triangle (see Figure 4.8c). The two vacancies in fourth neighbour or closer could drag the Ar substitutional atom from its site with a low energy barrier (see Figures 4.8 and 4.7). The split vacancy shape could form

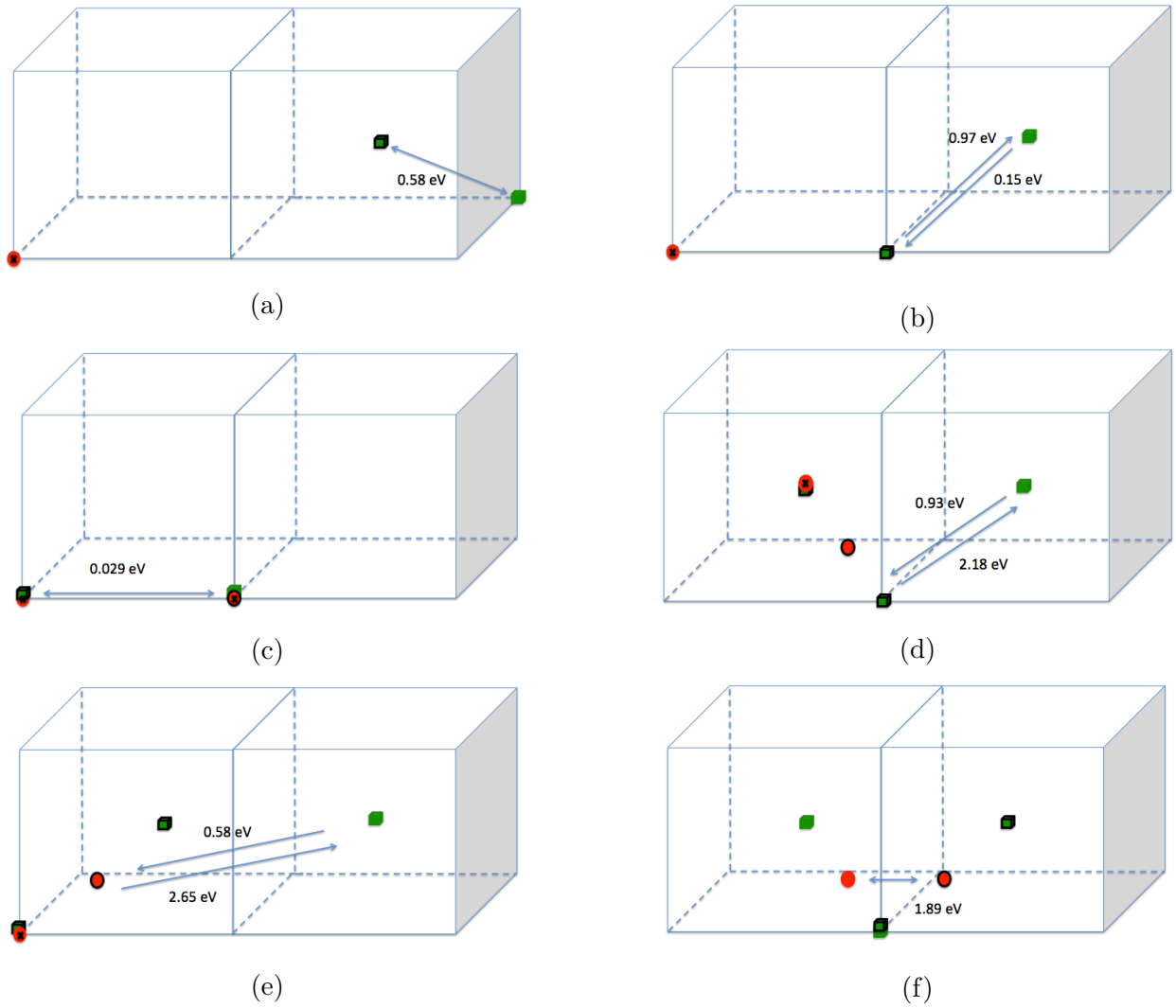

Figure 4.7: The diagram to show the transitions from the initial Ar substitutional atom with a vacancy in bcc Fe system. The red sphere represents the Ar. The black outline shows the configuration after transition. The green cube is the Fe vacancy. The cross sign inside indicts the substitutional atom. The vacancies shown as green cube without outline disappear after the transition. (a) The diffusion of the 8th neighbour vacancy towards an Ar substitutional atom to its 4th neighbour with the forward and reverse barrier of 0.58 eV. (b) The diffusion of the 4th neighbour vacancy to 2nd neighbour towards the Ar substitutional atom with the barrier of 0.15 eV and the reverse barrier of 0.97 eV. (c) A swap between an Ar substitutional atom and the vacancy in second neighbour with the forward and reverse barrier of 0.029 eV. (d) An Ar substitutional atom with one vacancy in second neighbour moves to form a split vacancy configuration leaving a vacancy in the original site. The forward barrier is 0.93 eV and the reverse barrier is 2.18 eV. (e) The initial configuration shown in (b) can directly form the split vacancy shown in (d) but without the intermediate step. The forward barrier is 0.58 eV and the reverse barrier is 2.65 eV. (f) The diffusion of the Ar split vacancy with the forward and reverse barrier of 1.89 eV.

with another vacancy nearby (see Figures 4.8a and 4.8d) or the system could directly go to the triangle configuration (see Figure 4.8c). Once the split vacancy shape with one vacancy nearby formed, it will also evolve directly into the Ar_1V_3 cluster (see Figure 4.8b) or make it through first exchanging into an Ar substitutional atom with two vacancies in its first neighbour (see Figures 4.8e and 4.8f). The Ar_1V_3 cluster can diffuse as shown in Figure 4.9, but the barrier for diffusion is very high at 1.82 eV. In all these cases shown in Figure 4.8, the lowest energy configuration is the Ar interstitial in the centre of a vacancy triangle.

In summary both the split vacancy complex and the Ar_1V_3 triangle complex give mechanisms by which an Ar atom can diffuse through the lattice but the barriers are very high. The isolated Ar interstitial becomes substitutional and although the reverse pathway is lower than the vacancy diffusion mechanisms, the likelihood is that another substitutional Ar will be formed due to the low energy barrier to form the substitutional. As a result it seems more likely that Ar bubble growth in Fe occurs through collision cascade effects rather than direct diffusion. These are examined in the next section.

4.5 Argon Bubbles and Irradiation

4.5.1 Collision Cascades

To study radiation damage, collision cascades are initiated near an existing bubble as was done for the bubbles in Section 3.7. It can be seen from Figure 4.10 that for the larger bubbles, no interaction with a 1 keV cascade will occur if the PKA is generated more than 5.2 nm from the bubble. For the small bubble this distance drops to 4.4 nm. By targeting the trajectories within the cones, good statistics can be obtained without the necessity for lots of redundant trajectory calculations which produce no damage near the bubble.

Figure 4.11 shows how the number of vacancies in the cluster changes, for the three sizes of Ar-vacancy cluster, where the initial number of vacancies is kept constant at 15. At a low Ar-to-vacancy ratio, maintaining the ratio is clearly favoured, which is different from He

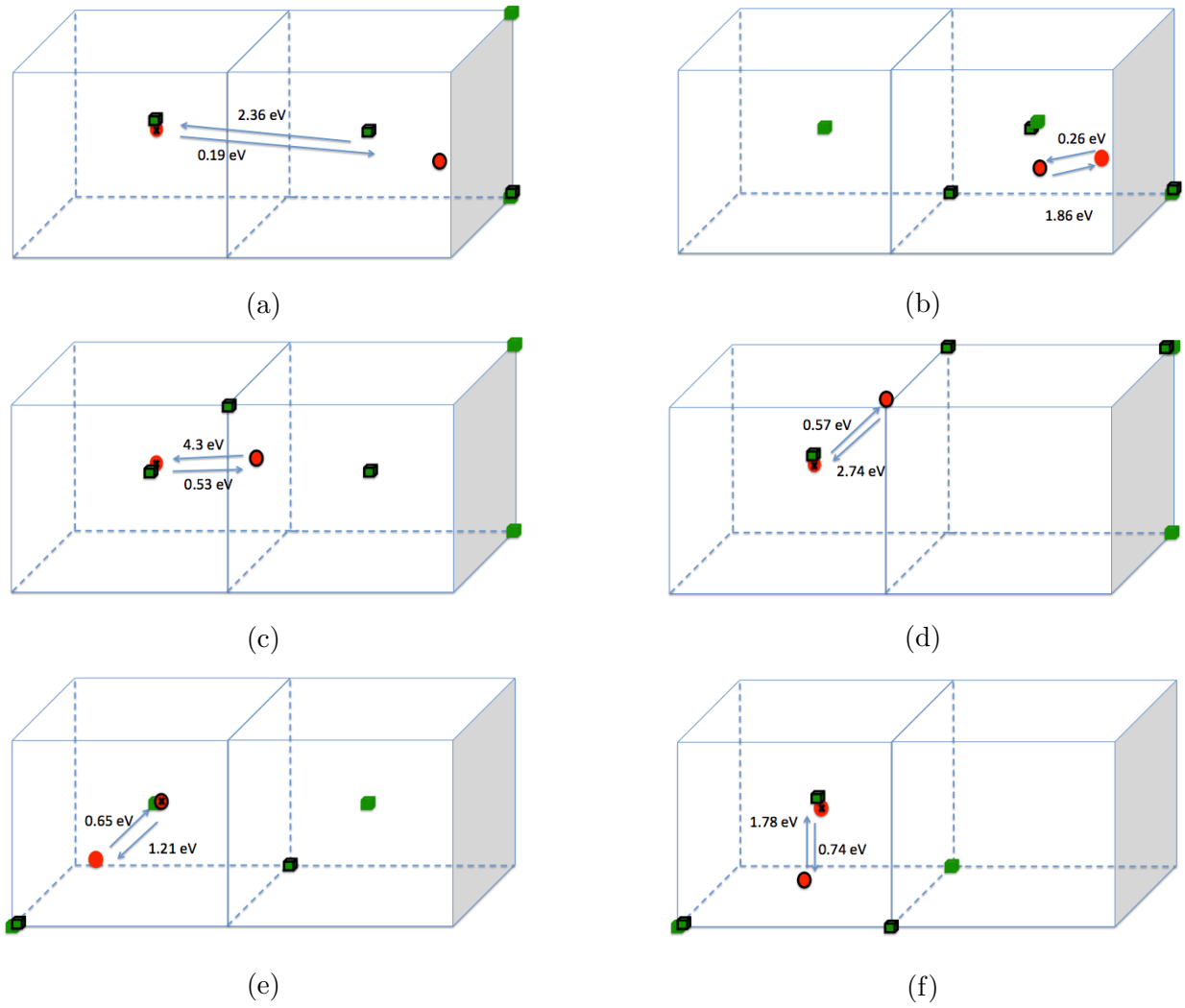

Figure 4.8: Illustration of the transitions from the initial Ar substitutional atom with 2 vacancies. The red sphere represents the Ar. The black outline shows the configuration after transition. The green cube is the Fe vacancy. The cross sign inside indicts the substitutional atom. The vacancies shown as green cube without outline disappear after the transition. (a) An Ar substitutional atom with 2 vacancies in the 4th neighbour position moves to form a split vacancy configuration leaving a vacancy in the original site. The forward barrier is 0.19 eV and the reverse barrier is 2.36 eV. (b) The configuration that occurs after the transition shown in (a) forms a vacancy triangle with the Ar interstitial at its centre. The forward barrier is 0.26 eV and the reverse barrier is 1.86 eV. (c) The initial configuration shown in (a) can directly form the vacancy triangle system shown in (b) but without the intermediate step. The forward barrier is 0.53 eV and the reverse barrier is 4.3 eV. (d) A similar transition to that shown in (a) when the Ar substitutional atom forms a different split vacancy configuration. The forward barrier is 0.57 eV and the reverse barrier is 2.74 eV. (e) The configuration shown at the end of (a) evolves into an Ar substitutional atom with 2 Fe vacancies in the first neighbour. The forward barrier is 0.65 eV and the reverse barrier is 1.21 eV. (f) The Ar substitutional atom with 2 vacancies in the first neighbour evolves into an Ar interstitial in the centre of a vacancy triangle. The forward barrier is 0.74 eV and the reverse barrier is 1.78 eV.

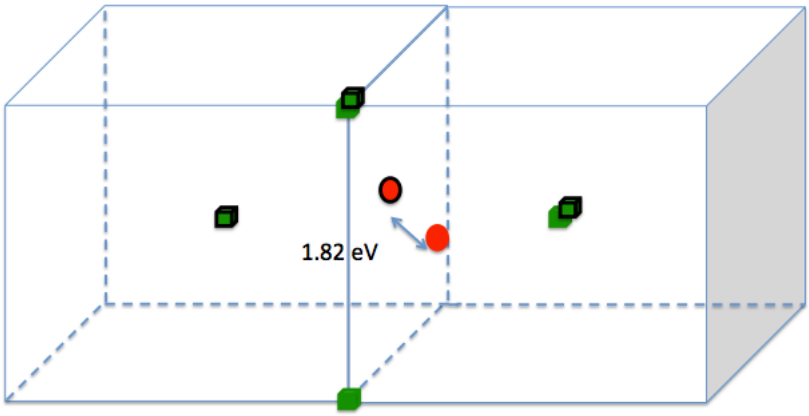

Figure 4.9: The diffusion of Ar triangle cluster Ar_1V_3 with the forward and reverse barrier of 1.82 eV.

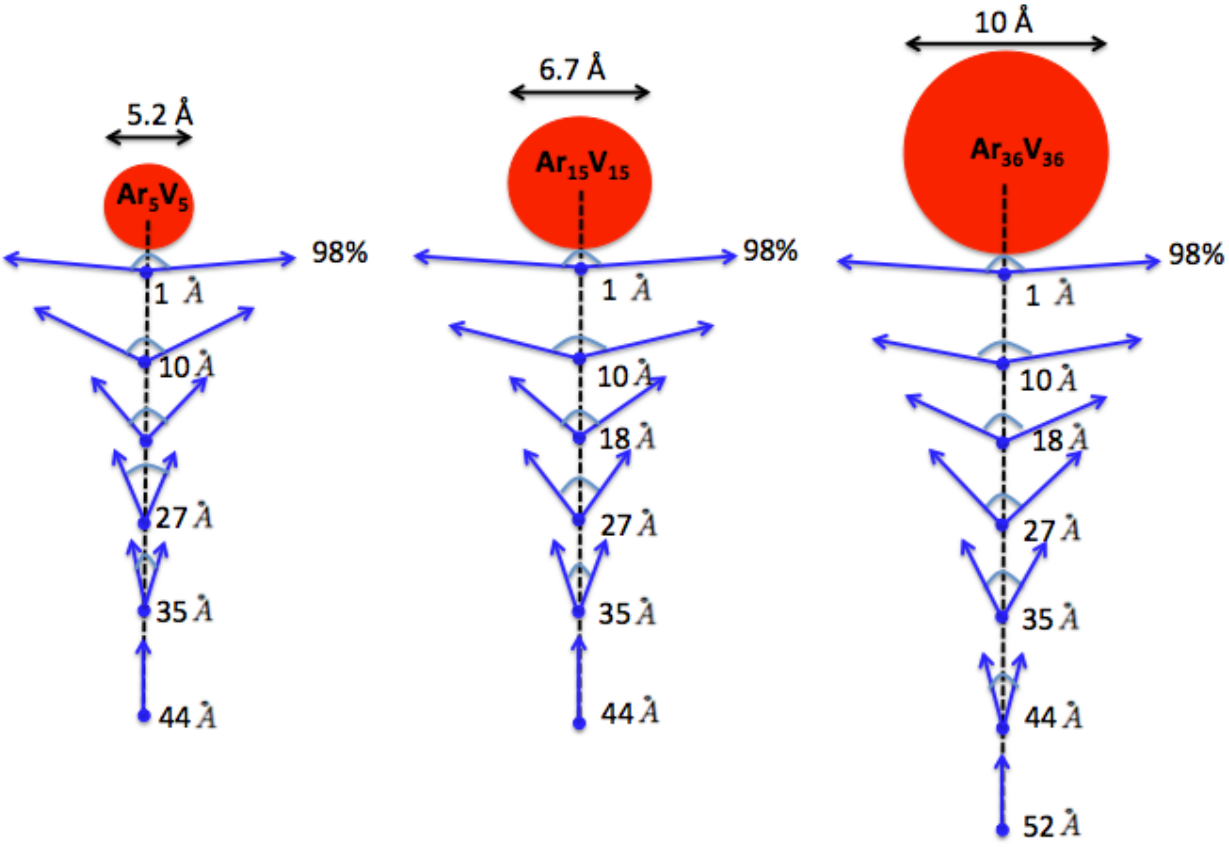

Figure 4.10: Representations of the cones for collision cascades that have a 98% probability of interacting with the argon bubble. Different lines represent the cone angle as a function of separation and bubble size, using the same method in Section 3.7.1.

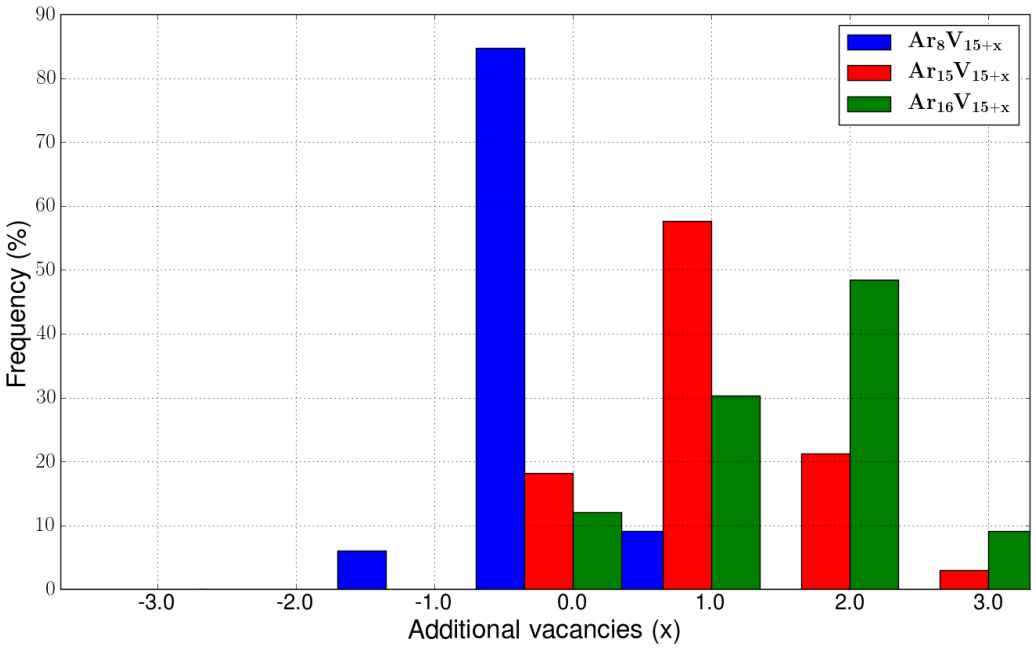

Figure 4.11: Frequency of capture/loss of vacancies during the collision cascade for a system containing 15 vacancies. The three sets of results show three cases of (1) below the ideal Ar-to-vacancy ratio, (2) at the optimal (from Figure 4.2) ratio and (3) above the ideal ratio.

where He bubbles can easily capture Fe atoms. This changes at the optimal (from Figure 4.2) Ar-to-vacancy ratio, where the bubble expels Fe atoms (i.e. absorbs vacancies). Above the optimal (from Figure 4.2) ratio, vacancy capture becomes more favoured. Therefore, radiation provides a process for an Ar bubble to be enlarged by expelling Fe atoms or by attracting nearby vacancies.

4.5.2 Energy barriers for isolated Ar to join an existing bubble

In order to gain an understanding of Ar accumulation into bubbles, a study was carried out to investigate the energetics of the barriers for Ar to diffuse into or outwards from an existing bubble from an interstitial site near an existing bubble. To achieve that, we classified Ar interstitials according to the distance between the interstitial and the surface of a bubble as given in Table 4.2. For each neighbour, at least 20 different positions of interstitials are investigated and 4000 saddle point searches are carried out.

Neighbour (N)	1	2	3	4	5	6
Distance Å	1.0-1.9	1.9-2.8	2.8-3.5	3.5-4.2	4.2-4.9	4.9-5.5

Table 4.2: Classification of Ar interstitials with respect to the distance from an Ar bubble.

Migration energy barriers were calculated for the Ar interstitials diffusing towards Ar bubbles of different sizes. The initial positions of the interstitial Ar atoms were varied from 1 to 6 nearest neighbour (N) distant from the edge of the bubble and the summarised data is presented in Table 4.3.

Typical energy barrier (eV)	Diameter (Å)	1 N	2 N	3 N	4 N	5 N	6 N
Ar_3V_5	3.0	0	0	0	0	0	0.007
Ar_5V_5	5.2	0	0	0	0	0	0.07
Ar_6V_5	5.3	0	0	0	0	0	0.07
Ar_5V_9	3.8	0	0	0	0	0	0.006
Ar_9V_9	5.4	0	0	0	0	0	0.07
$Ar_{10}V_9$	6.4	0	0	0	0	0	0.07
Ar_8V_{15}	4.9	0	0	0	0	0	0.004
$Ar_{15}V_{15}$	6.7	0	0	0	0	0	0.07
$Ar_{16}V_{15}$	7.4	0	0	0	0	0	0.07
$Ar_{18}V_{36}$	8.1	0	0	0	0	0	0.004
$Ar_{36}V_{36}$	10.0	0	0	0	0	0	0.07
$Ar_{37}V_{36}$	10.5	0	0	0	0	0	0.07

Table 4.3: A summary of migration barriers (eV) of Ar interstitials diffusing towards Ar bubbles of different configurations. The first column specifies the bubble size, where the following columns represent the initial Ar interstitial position as specified in Table 4.2. For each neighbour, at least 20 different positions of interstitials are investigated and 4000 saddle point searches are carried out.

Typically, the Ar interstitial jumps occur to adjacent N positions, e.g. if an Ar interstitial is initially positioned at 6N, then diffusion occurs by jumping to 5N, then from 5N to 4N and so on, until from 1N the Ar interstitial joins the bubble configuration. Therefore in Table 4.2 we give migration barriers for jumping to adjacent N position in the direction towards the bubble.

In Table 4.3, a barrier of 0 eV accounts for the cases when Ar interstitials instantaneously join the Ar bubble, during equilibration (i.e. the barrier is less than 0.003 eV). It usually occurs in the systems which consist of Ar bubbles which have a fairly low Ar-to-vacancy

ratio (typically less than 1 : 1). This suggests that bubbles with a low Ar-to-vacancy ratio have a strong tendency to attract Ar interstitials that are in their vicinities. Further, for the ratio $> 1 : 1$, although the barrier for additional Ar to join the bubbles is small, this extra Ar will make the bubble emit Fe split interstitials so that the number of vacancies in the bubble will increase, which means the previous configuration has been changed. Considering that it is 0.07 eV for the isolated Ar interstitial atom to become substitutional, it is more favoured for the nearby Ar interstitial to join the bubble rather than become substitutional. Further, we have checked the energy barrier for the bubble with a 1 : 1 ratio to absorb an additional Ar located in the 6th neighbour substitutional site is more than 1 eV but for the Ar substitutional atom within the 5th neighbour (the 5th neighbour is included), it goes to be attached by the existing bubble with leaving the vacancy in the original site after the minimisation. This suggests the existence of a capture zone around an existing Ar bubble which extends to 5th neighbour position. Table 4.4 shows also that even at the 6th neighbour position the interstitial migration barriers away from the bubble are much higher than in the perfect lattice.

To investigate this effect and to complement the previous results, a study was performed by checking the migration barriers of Ar interstitials in the direction away from the bubble. This is summarised in Table 4.4.

Ar interstitials move from 1N to 2N, from 2N to 3N and so on as given in Table 4.4. The "-" accounts for the cases when no valid migration processes of Ar interstitials were observed because of instantaneously joining the bubble in these cases (see Table 4.3). Comparing the barrier for the Ar to join the bubble (see Table 4.3) with that to leave the bubble (see Table 4.4), interstitial Ar atoms favour joining the bubble, but if the Ar-to-vacancy ratio is above optimal, after joining the bubble, the extra Ar will change the configuration of bubbles with emission of Fe interstitials.

Moreover, we have also examined some large bubbles containing more than 90 vacancies, whose diameter is more than 1.2 nm. The additional Ar will still join the bubble if the Ar-

Typical energy barrier (eV)	1 N	2 N	3 N	4 N	5 N	6 N
Ar_3V_5	-	-	-	-	-	2.4
Ar_5V_5	-	-	-	-	-	2.2
Ar_6V_5	-	-	-	-	-	2.2
Ar_5V_9	-	-	-	-	-	2.3
Ar_9V_9	-	-	-	-	-	2.2
$Ar_{10}V_9$	-	-	-	-	-	2.2
Ar_8V_{15}	-	-	-	-	-	1.9
$Ar_{15}V_{15}$	-	-	-	-	-	1.7
$Ar_{16}V_{15}$	-	-	-	-	-	1.7
$Ar_{18}V_{36}$	-	-	-	-	-	1.9
$Ar_{36}V_{36}$	-	-	-	-	-	1.7
$Ar_{37}V_{36}$	-	-	-	-	-	1.7

Table 4.4: A summary of migration barriers (eV) of Ar interstitials diffusing away from the Ar bubble. The first column specifies the bubble size and the following columns represent the initial Ar interstitial position as specified in Table 4.2. For each neighbour, at least 20 different positions of interstitials are investigated and 4000 saddle point searches are carried out.

to-vacancy ratio is below optimal, which means there are extra vacancies for Ar to locate to. However, when the ratio reaches the optimal, instead of joining the bubble, the Ar interstitials from the 5th neighbour outwards are kinetically favourable to become substitutional with emitting Fe interstitials since the barrier is around 0.07 eV whereas to join the bubble needs more than 1 eV.

In summary, for the bubbles with the diameter < 1.1 nm, it is kinetically possible to absorb additional Ar, even when the Ar-to-vacancy ratio is above optimal (from Figure 4.2), but the Ar interstitial becomes less likely to jump towards the bubble with the Ar-to-vacancy ratio above the optimal when the diameter $>\approx 1.2$ nm. Instead of that, isolated Ar interstitials will become substitutional in the neighbourhood of the bubbles with the optimal ratio or above if the diameter is more than 1.2 nm. Thus enlargement of the bubble appears to be driven either by irradiation or vacancy capture.

4.6 Conclusions

Single argon atoms prefer to be substitutional rather than interstitial and the energy barrier to form the substitutional as 0.07 eV means this occurs generally at room temperature, which is totally different from He in bcc Fe. Thus an isolated Ar atom injected into a bcc Fe lattice would be expected to settle at a substitutional site. The optimal (from Figure 4.2) Ar-to-vacancy ratio has been determined as 1 : 1 and it has been shown how bubbles can also absorb additional vacancies produced by irradiation to reduce the lattice strain around the bubble, which would reduce the energy barriers and allow more Ar to join. The energy barriers for an interstitial Ar atom to join an existing bubble are tiny, and especially within the fifth neighbour, joining occurs instantaneously. A mechanism for isolated Ar to diffuse in bcc Fe in the absence of a nearby bubble is through a vacancy driven process but the energy barrier for this to occur is very high.

Chapter 5

Xenon Bubbles in bcc Fe

5.1 Introduction

TEM observations of Xe-implanted iron and molybdenum thin films were carried out by Dinhut and Denanot [103]. They have detected solid Xe bubbles at room temperature. Based on the measured lattice parameters and the atomic volume values, the fcc structure is shown to be the most probable structure for the solid bubbles in both materials.

Templier *et al.* [104] studied xenon precipitation in bulk aluminium using TEM in order to avoid the superposition of several different phenomena. At room temperature, TEM diffraction patterns show that xenon is a solid crystallized with an fcc structure.

Gavarini *et al.* [105] investigated xenon migration behaviour in titanium nitride by implanting 800 keV Xe^{++} ions in sintered samples at an ion fluence of 5×10^{15} cm^2. Annealing was performed at temperatures ranging from 1673 to 1923 K for 1 and 3 h. Xenon concentration profiles were studied by Rutherford backscattering spectrometry (RBS) using 2.5 MeV α-particles. The mean activation energy corresponding to the diffusion component was found to be 2.2 ± 0.3 eV (i.e. 2.2 eV implies the time scale for a hop at 1923 K is about 58 ns with a prefactor of 10^{13}).

Overall, the experimental references imply that the Xe atoms are only mobile at high

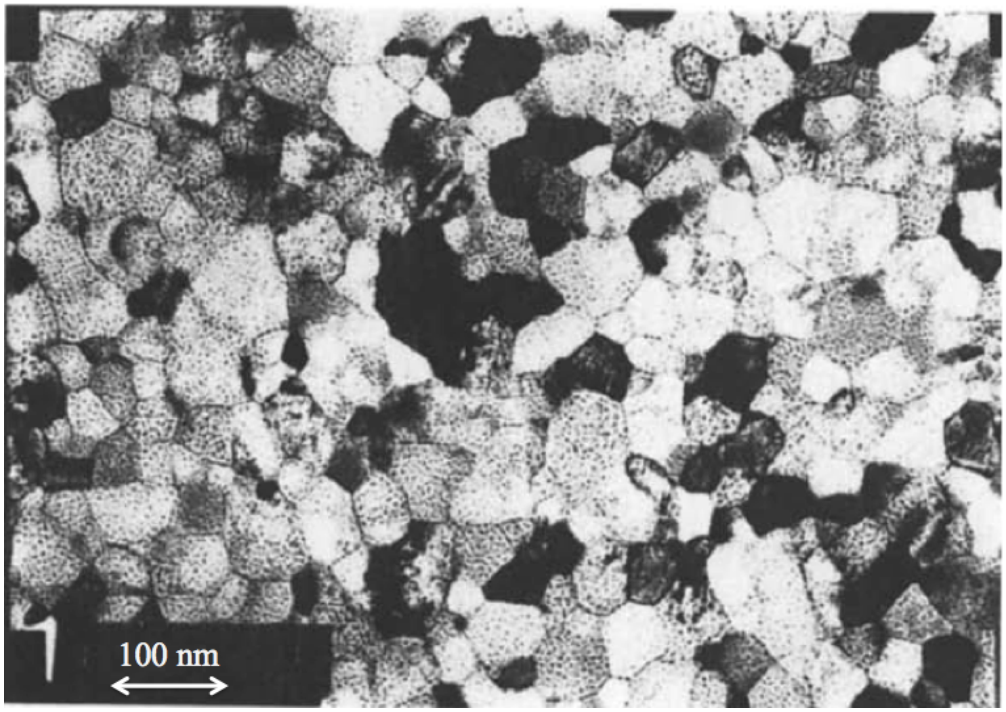

Figure 5.1: Electron diffraction patterns and bright fields of iron thin films after 2×10^{16} Xe ion/cm^2 implantation. The image is taken from [103]. The Xe bubbles appear as small black dots in the grains.

temperature. In this chapter, the results of a study both on the statics of small xenon-vacancy clusters in bcc iron and their interaction with nearby collision cascades are presented, which will provide insight into how a xenon bubble forms and grows. We also investigate the structure of small Xe clusters in Fe and the energy barriers that need to be overcome before growth by diffusion can occur.

5.2 Potential

For simulating the xenon-vacancy clusters in the bcc iron system, we use the Lennard-Jones potential for Xe-Xe interaction, ZBL potential for Xe-Fe and the same Ackland-Mendelev potential used in helium-vacancy cluster in bcc Fe system for Fe-Fe here (see Section 2.1.3).

5.3 Formation Energy

The formation energy of the xenon-vacancy clusters Xe_nV_m is calculated using the Monte Carlo algorithm, which is introduced in Section 3.3.

First, we list the formation energy of several defects in the system. The calculations implies it is energetically favourable for the xenon atom to locate in the substitutional site while the tetrahedral interstitial is more stable than the octahedral.

Fe cohesive energy	vacancy formation energy	Xe substitutional formation energy	Xe tetrahedral formation energy	Xe octahedral formation energy
4.013 eV	1.72 eV	15.45 eV	20.15 eV	20.43 eV

Table 5.1: The formation energy of defects for Xe in bcc Fe.

Before the calculations, we have checked the lattice parameter of Xe bubbles. In pure fcc bubbles, the lattice parameter is 6.262 Å, while when embedded in bcc Fe matrix, it comes to 5.67 Å for fcc Xe bubbles consistent with the experiment results [103].

Figure 5.2 shows the formation energy of the Xe_nV_m clusters at 0 K from Equations 3.1, 3.2 and 3.3. Each curve is with a fixed number of vacancies, which implies that all the bubbles have preformed vacancies before Xe is inserted. To ensure the results can be compared on a similar scale, the figure shows the formation energy per vacancy. It is clear that each curve reveals an optimal (lowest formation energy per vacancy) Xe-to-vacancy ratio (calculated with a fixed number of vacancies). The optimum bubble size is given by the minima on the curves in Figure 5.2. It can be seen that the optimum ratio is varying between 0.6 : 1 and 0.8 : 1. Further, each curve stops at the final point because the bubble is no longer stable to hold more xenon with the given number of vacancies; in other words, adding extra xenon will cause the bubble to push the neighbouring Fe atoms into interstitials with increasing the number of vacancies in the bubbles, similar to Ar as shown in Figure 4.3.

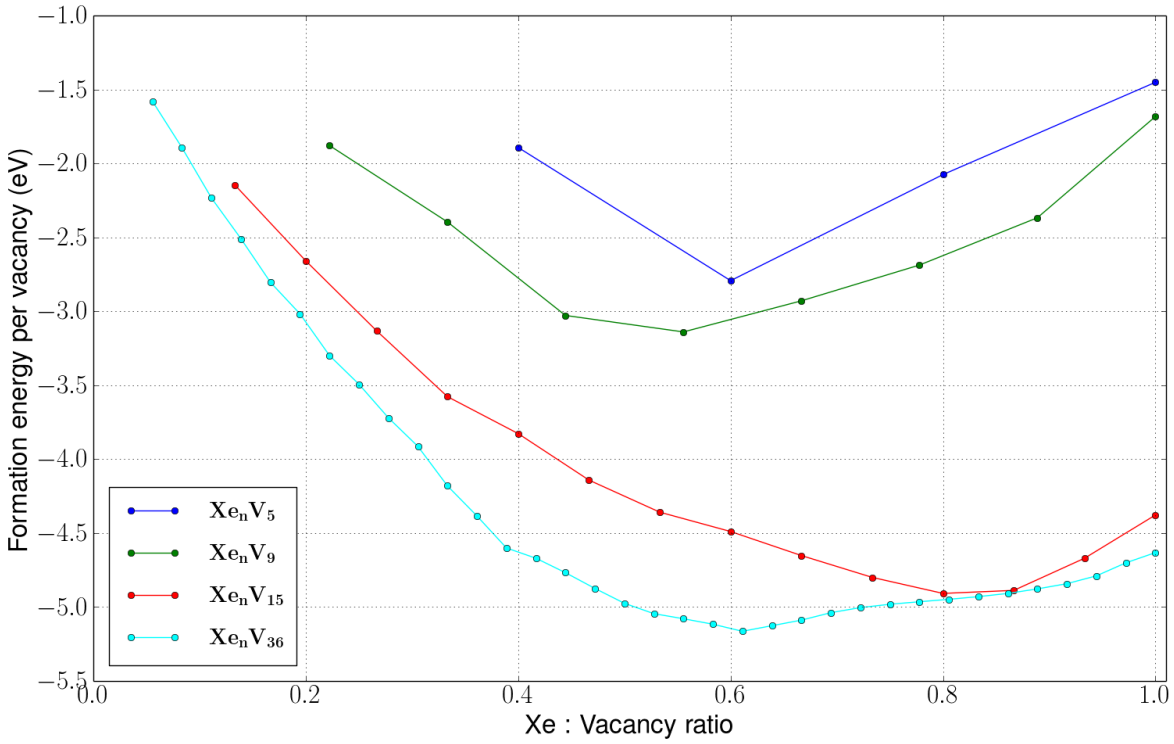

Figure 5.2: The formation energy as a function of the number of xenon atoms for different sizes of Xe_nV_m clusters.

5.4 Diffusion mechanisms

In this section, all the transition barriers and end states were calculated by saddle point searches from the initial state without any assumption about the final state.

5.4.1 Xe tetrahedral interstitial

For xenon, the barrier for a single interstitial to diffuse to another interstitial site is found as 0.5 eV (see Figure 5.3). Instead of diffusing into an interstitial site, it is kinetically favourable for Xe to become substitutional with a smaller barrier of 0.15 eV; for the barrier to be reversed, it is 1.83 eV.

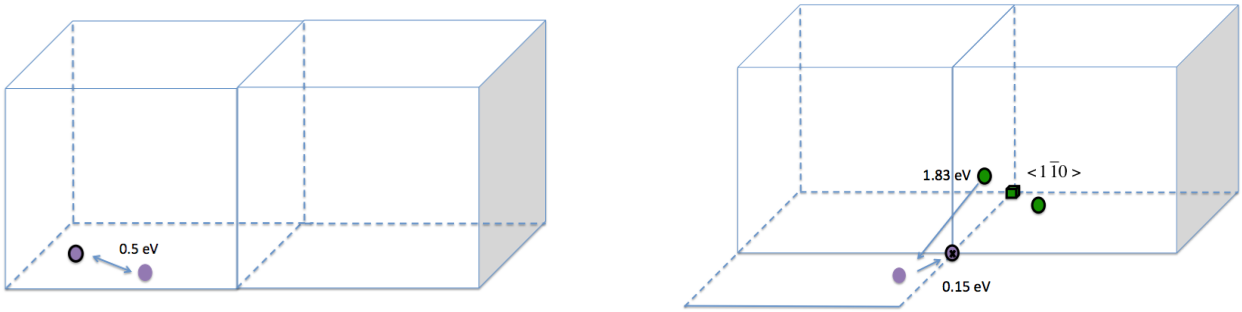

(a) (b)

Figure 5.3: The transitions from the initial Xe tetrahedra interstitial in bcc Fe system. The purple sphere represents the Xe atom. The black outline shows the configuration after transition. The green sphere is the Fe interstitial and the green cube is the Fe vacancy. The cross sign inside indicts the substitutional Xe atom. (a) The transition of the Xe tetrahedral interstitial to its neighbouring tetrahedral site with the forward and reverse barrier of 0.5 eV. (b) The transition of the Xe tetrahedral interstitial to the Xe substitutional with the Fe dumbbell interstitial with the energy barrier of 0.15 eV and the reverse barrier of 1.83 eV.

5.4.2 Xe substitutional with an Fe dumbbell interstitial

Different from He in bcc Fe, the Xe substitutional atom is stable with the Fe dumbbell interstitial as its neighbour. Diffusion of a substitutional Xe atom to enlarge a bubble is possible within MD time scales and Xe shows even less mobility than the Ar atom in bcc Fe. Figures 5.4 and 5.5 show that it is slightly energetically favourable for the Fe dumbbell to

be located close to the Xe substitutional atom but the difference between the forward and reverse barrier is small.

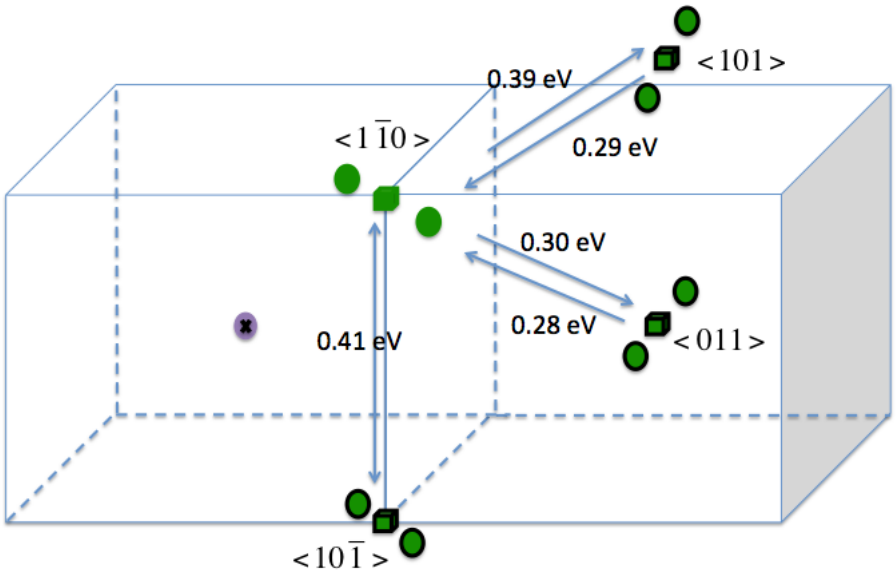

Figure 5.4: Illustration of the diffusion of the Fe dumbbell interstitial with a Xe substitutional atom. The purple sphere represents the Xe atom. The black outline shows the configuration after transition. The green sphere is the Fe interstitial and the green cube is the Fe vacancy. The cross sign inside indicts the substitutional atom.

5.4.3 Xe substitutional with a vacancy nearby

Similar to Section 4.4.2.1, we have also checked the case where the Xe substitutional atom locates with one free vacancy to see the mobility of Xe. We find the same conclusion as with Ar, namely that the Xe substitutional is not stable with the vacancy located in first neighbour. It will instantaneously turn into the Xe split vacancy shape. The split vacancy configuration is stable during MD time scales and would diffuse with a high barrier 2.03 eV, which relates to what Gavarini *et al.* found in TiN [105].

Different from the Ar substitutional atom which is stable with a vacancy in the second neighbour, Xe would form a split vacancy configuration where Xe locates at the octahedral interstitial site with the two vacancies as each other's second neighbour. This can evolve into the split vacancy shown in Figure 5.6. The transition barriers are shown in Figure 5.7.

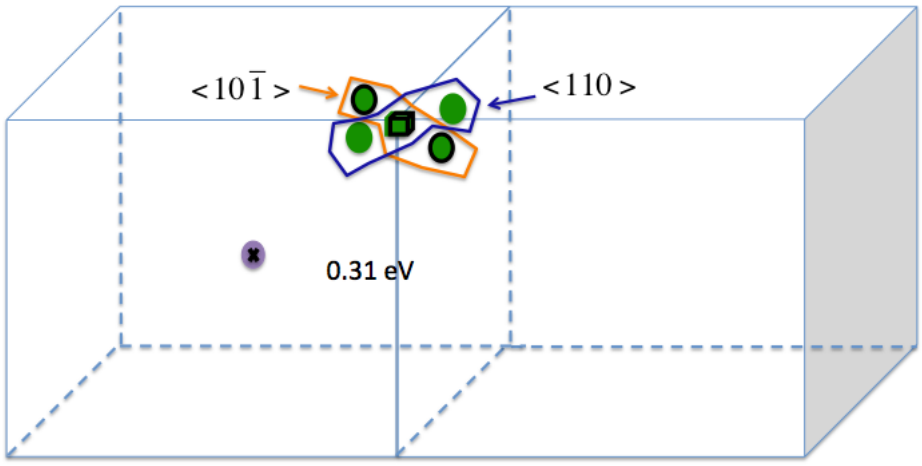

Figure 5.5: Illustration of the diffusion of the Fe dumbbell interstitial with a Xe substitutional atom. The purple sphere represents the Xe atom. The black outline shows the configuration after transition. The green sphere is the Fe interstitial and the green cube is the Fe vacancy. The cross sign inside indicts the substitutional atom.

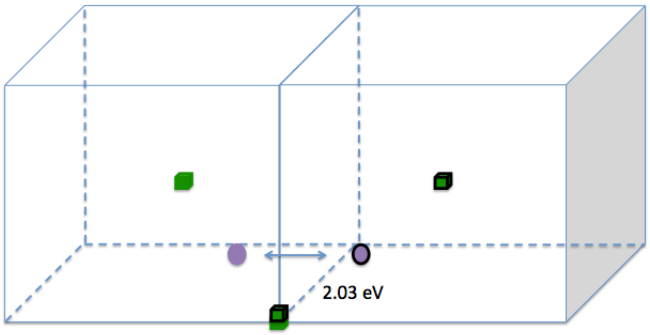

Figure 5.6: Illustration of the diffusion of the Xe split vacancy in bcc Fe with the forward and reverse barrier of 2.03 eV. The purple sphere represents the Xe atom. The black outline shows the configuration after transition. The green cube is the Fe vacancy. The cross sign inside indicts the substitutional atom.

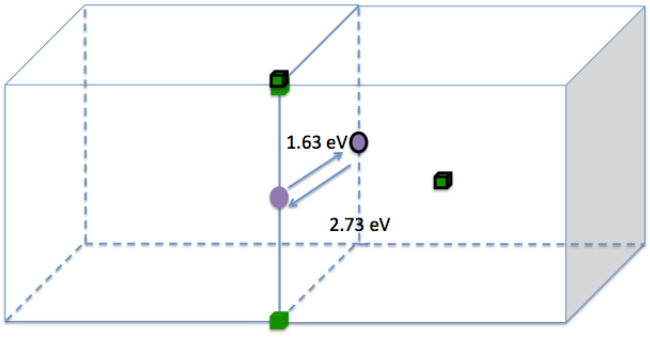

Figure 5.7: The diffusion between two kinds of the Xe split vacancies in bcc Fe system. The purple sphere represents the Xe atom. The black outline shows the configuration after transition. The green cube is the Fe vacancy. The cross sign inside indicts the substitutional atom.

The free vacancy is favoured to move towards the Xe atom (see Figure 5.8a). Once it comes within the fourth neighbour, it will evolve into one of the two split vacancy configurations (see Figures 5.8d, 5.8c and 5.8b). Typical transitions are illustrated in Figure 5.8.

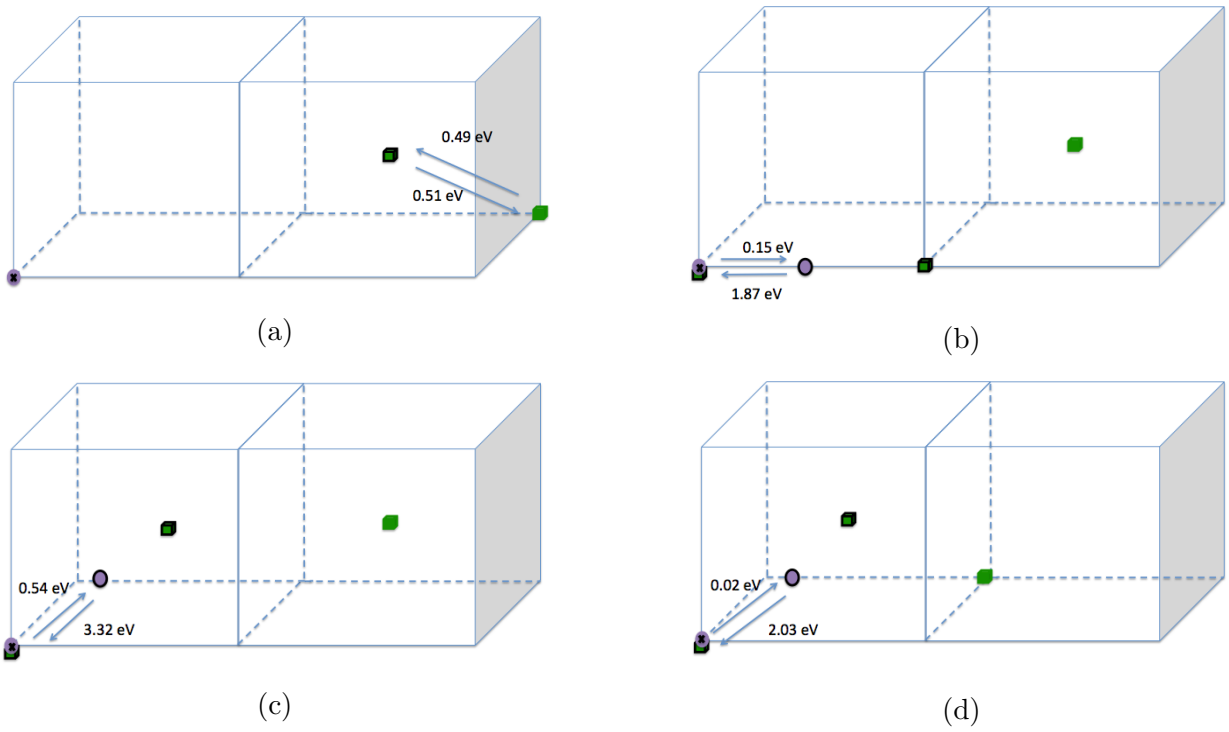

Figure 5.8: The transitions from the initial Xe substitutional atom with a vacancy in bcc Fe system. The purple sphere represents the Xe atom. The black outline shows the configuration after transition. The green cube is the Fe vacancy. The cross sign inside indicts the substitutional atom. (a) The diffusion of the 8th neighbour vacancy towards a Xe substitutional atom to its 4th neighbour. The forward barrier is 0.49 eV and the reverse barrier is 0.51 eV. (b) The transition of Xe substitutional with a vacancy in fourth neighbour to Xe split vacancy in Figure 5.7. The forward barrier is 0.15 eV and the reverse barrier is 1.87 eV. (c) The transition of Xe substitutional with a vacancy in fourth neighbour to Xe split vacancy in Figure 5.6. The forward barrier is 0.54 eV and the reverse barrier is 3.32 eV. (d) The transition of Xe substitutional with a vacancy in third neighbour to Xe split vacancy in Figure 5.6. The forward barrier is 0.02 eV and the reverse barrier is 2.03 eV.

5.4.4 Xe substitutional with two vacancies nearby

If two vacancies are located around a Xe substitutional atom, some typical transitions are shown in Figure 5.9. The lowest energy configuration the Xe and two vacancies tend to form is a Xe_1V_3 cluster like the isosceles triangle as we found with Ar. Two vacancies in

fourth neighbour or closer could drag the Xe substitutional atom into an interstitial site. It works similarly to the case with Ar but with lower energy barriers (see Figures 5.9 and 4.8). The split vacancy shape with another vacancy nearby could be formed (see Figures 5.9a and 5.9d) or the triangle configuration (see Figure 5.9c). Once the split vacancy shape with one vacancy nearby formed, it will also evolve directly into the Xe_1V_3 cluster (see Figure 5.9b) or through exchanging the Xe substitutional atom with two vacancies in its first neighbour (see Figures 5.9e and 5.9f). The Xe_1V_3 cluster can diffuse with a high barrier as 2.06 eV (i.e. the time scale for a hop at 500 K is over 1.8 years), see Figure 5.10.

Compared with one Ar substitutional atom with a vacancy nearby (see Figures 4.7 and 4.8), Xe has a lower energy barrier to form the Xe_1V_2 or Xe_1V_3 clusters. Therefore, diffusion of a Xe atom to enlarge a bubbles is more unlikely than Ar. Xe atoms are favoured to become substitutional and attract free vacancies in the system to form small bubbles locally rather than diffuse. Xe atoms show more attraction to Fe vacancies than Ar and He. When a Xe atom becomes substitutional, vacancies close by can assist it to diffuse but only with large barriers. Similar to Ar in bcc Fe, Xe bubble growth occurs more likely through irradiation rather than direct diffusion. This is examined in the next section.

5.5 Xenon Bubble Growth

5.5.1 Collision Cascades

Figure 4.10 shows that for the larger bubbles, no interaction with a 1 keV cascade will occur if the PKA is generated more than 6 nm from the bubble. For the small bubble this distance drops to 4.4 nm. By targeting the trajectories within the cones shown in the figure, good statistics can be obtained without the necessity for lots of redundant trajectory calculations which produce no damage near the bubble.

Figure 5.12 shows how the number of vacancies in the cluster changes, for the three sizes of Xe-vacancy cluster, where the initial number of vacancies is kept constant at 15.

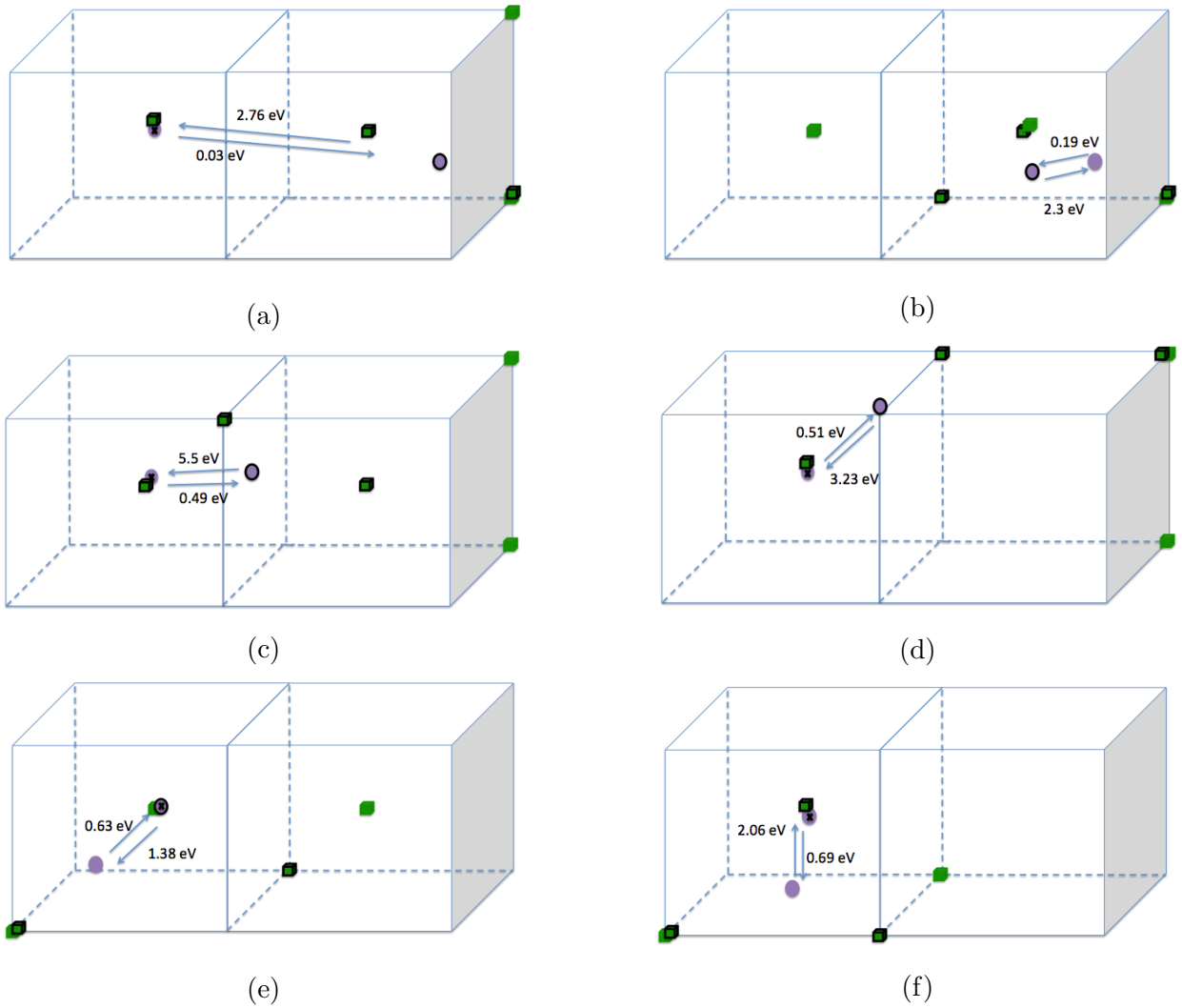

Figure 5.9: The transition of the Xe substitutional atom with two vacancies in bcc Fe system. The purple sphere represents the Xe atom. The black outline shows the configuration after transition. The green cube is the Fe vacancy. The cross sign inside indicts the substitutional atom. (a) One vacancy move with Xe moving from the substitutional site to form the Xe split vacancy with the forward barrier of 0.03 eV and the reverse barrier of 2.76 eV. (b) The transition of the Xe split vacancy with the vacancy nearby to Xe_1V_3 with the forward barrier of 0.19 eV and the reverse barrier of 2.3 eV. (c) The Xe substitutional atom with two vacancies directly turns into the triangle shape with the forward barrier of 0.49 eV and the reverse barrier of 5.5 eV. (d) One vacancy move with Xe moving from the substitutional site to form the Xe split vacancy with the forward barrier of 0.51 eV and the reverse barrier of 3.23 eV. (e) The Xe split vacancy with the vacancy nearby turns into a Xe substitutional atom with two vacancies in the first neighbour with the forward barrier of 0.63 eV and the reverse barrier of 1.38 eV. (f) The Xe substitutional atom with two vacancies as first neighbours evolves into the triangle shape with the forward barrier of 0.69 eV and the reverse barrier of 2.06 eV.

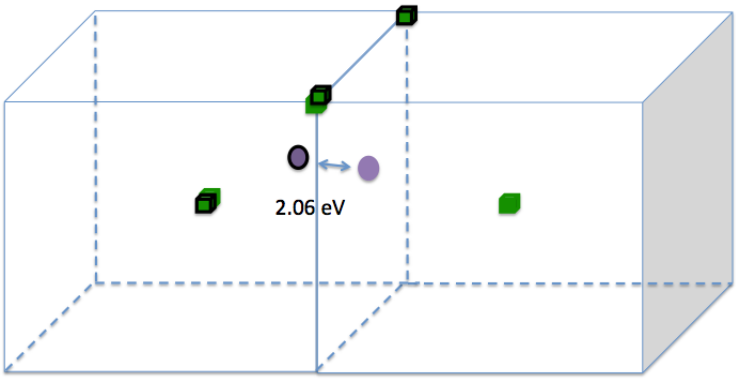

Figure 5.10: The diffusion of Xe triangle cluster Xe_1V_3 with the forward and reverse barrier of 2.06 eV.

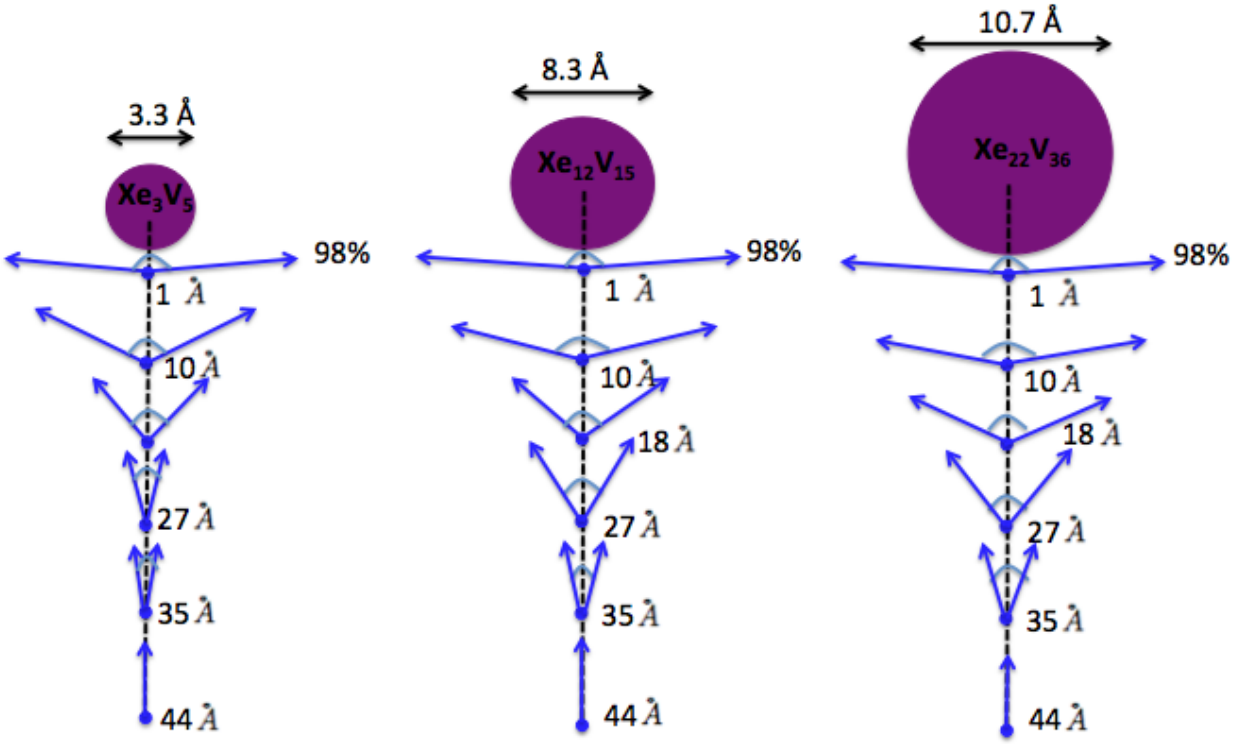

Figure 5.11: Representations of the cones for collision cascades that have a 98% probability of interacting with the xenon bubble. Different lines represent the cone angle as a function of separation and bubble size, using the same method as in Section 3.7.1.

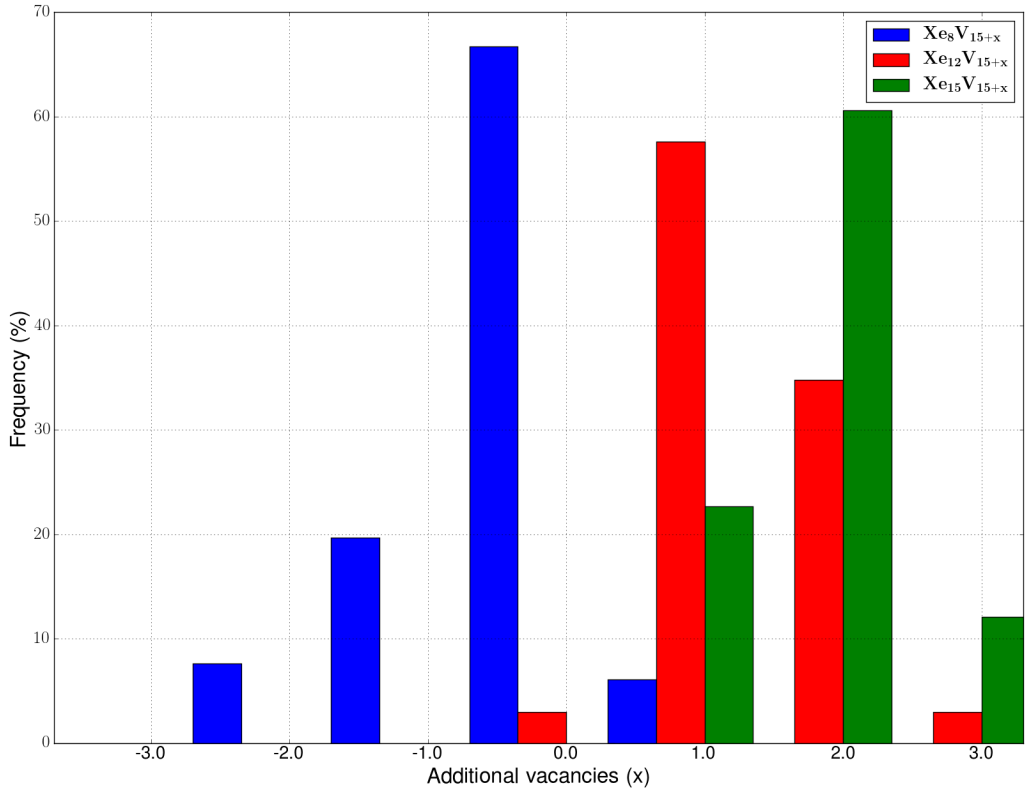

Figure 5.12: Frequency of capture/loss of vacancies during the collision cascade for a system containing 15 vacancies. The three sets of results show three cases of (1) below the ideal Xe-to-vacancy ratio, (2) at the optimal (from Figure 5.2) ratio and (3) above the ideal ratio.

As might be expected, the conclusion is similar to Ar in bcc Fe. At a low Xe-to-vacancy ratio, retaining vacancies is clearly favoured. This changes at the optimal (from Figure 5.2) Xe-to-vacancy ratio; even if the bubble contains extra vacancies at the optimal ratio, the bubble can absorb vacancies. Above the optimal (from Figure 5.2) ratio, vacancy capture (ejection of Fe interstitials) becomes more favoured. Therefore, radiation provides a process for a Xe bubble can be enlarged by emitting Fe interstitials.

5.5.2 Energy barriers for isolated Xe to join an existing bubble

Similar calculations are computed for xenon using the same method in Section 3.7.2. The migration energy barriers were calculated for the Xe interstitials diffusing towards Xe bubbles of different sizes. The initial positions of the interstitial Xe atoms were varied from 1 to 6 nearest neighbour (N) distance from the edge of the bubble.

The calculations show that Xe interstitials instantaneously join the Xe bubble, during equilibration. It occurs in the systems no matter whether the Xe-to-vacancy ratio is below or above the optimal ratio. Further, for the 1 : 1 ratio, the extra Xe will make the bubble emit one Fe split interstitial to maintain the 1 : 1 ratio.

Moreover, we have also examined the bubbles containing more than 90 vacancies, whose diameter is more than 1.5 nm. The additional Xe located within the 6th neighbour distance will still join the bubble if the Xe-to-vacancy ratio is below the 1 : 1 ratio. However, when the ratio reaches 1 : 1, instead of joining the bubble to generate more vacancies, it is kinetically favourable for the Xe interstitial to become substitutional in the 6th neighbour with emission of an Fe split interstitial, rather than join into the bubble because the barrier to join is over 1 eV. Further the potential energy of the system with the large bubbles having the 1 : 1 ratio with the Xe substitutional atom in the 6th neighbour is more than 1 eV lower than the case that this Xe is absorbed.

In summary, for the small Xe bubbles, it is kinetically possible to absorb additional Xe, even when the Xe-to-vacancy ratio is above optimal (from Figure 5.2). When the Xe-to-

vacancy ratio reaches 1 : 1, the additional Xe will join the bubble with emission of an Fe split interstitial. However, the Xe interstitial becomes less likely to jump towards the bubble with the Xe-to-vacancy ratio at the 1 : 1 ratio as the bubble diameter increases.

5.6 Conclusions

Single xenon atoms prefer to be substitutional rather than interstitial and the substitutional can form from the interstitial site in picoseconds at 500 K. Thus an isolated Xe atom injected into a bcc Fe lattice would be expected to settle at a substitutional site. The Xe interstitial can diffuse in the bcc Fe system with a pathway between adjacent tetrahedral sites over nanoseconds at room temperature. The optimal (from Figure 5.2) Xe-to-vacancy ratio has been determined to be between 0.6 : 1 and 0.8 : 1. It has been shown how bubbles can emit Fe interstitials produced by irradiation, which would allow more Xe to join. The energy barriers for a diffusing Xe atom to join an existing bubble are tiny, especially when the diameter of the bubble is less than 1.5 nm, so joining occurs instantaneously within the 6th nearest neighbour region. If the Xe-to-vacancy ratio reaches 1 : 1, an additional Xe within the 6th neighbour will join into the bubble by kicking out an Fe split interstitial to maintain the 1 : 1 ratio. When the bubbles reaches a size of $\sim$ 1.5 nm, the Xe interstitials from the 5th neighbour outwards of bubbles with 1 : 1 ratio become substitutional rather than join the bubble. A mechanism for isolated Xe to diffuse in bcc Fe is due to a vacancy driven process but the energy barrier for this to occur is even higher than Ar in bcc Fe.

Chapter 6

Argon Bubble Formation and Growth in fcc Al

6.1 Introduction

There is ample evidence in the literature that high-energy Ar ion bombardment can damage Al substrates with the formation of subsurface Ar agglomeration [106, 107, 108, 109]. Blackwell *et al.* [16] have successfully carried out modelling work of magnetron sputtering deposited Al and observed subsurface Ar agglomeration.

Cox and Goodhew observed the argon content of selected volumes of each aluminium sample by X-ray analysis in the transmission electron microscope (TEM) [110]. Various large Ar bubbles were found, which are bigger than He bubbles in Fe (see Figures 3.1 and 3.2). One sample with the generation of Ar bubbles ranging from 10 nm to 17 nm is shown in Figure 6.1.

Ortega *et al.* [111] have done calculations using static and dynamic simulation in aluminium using the Ercolessi and Adams potential and Voter and Chen potential to determine point defect energies in the fcc aluminium system. e.g. the isolated vacancy formation energy was calculated as 0.61 eV and the divacancy (two vacancies located in each other's first

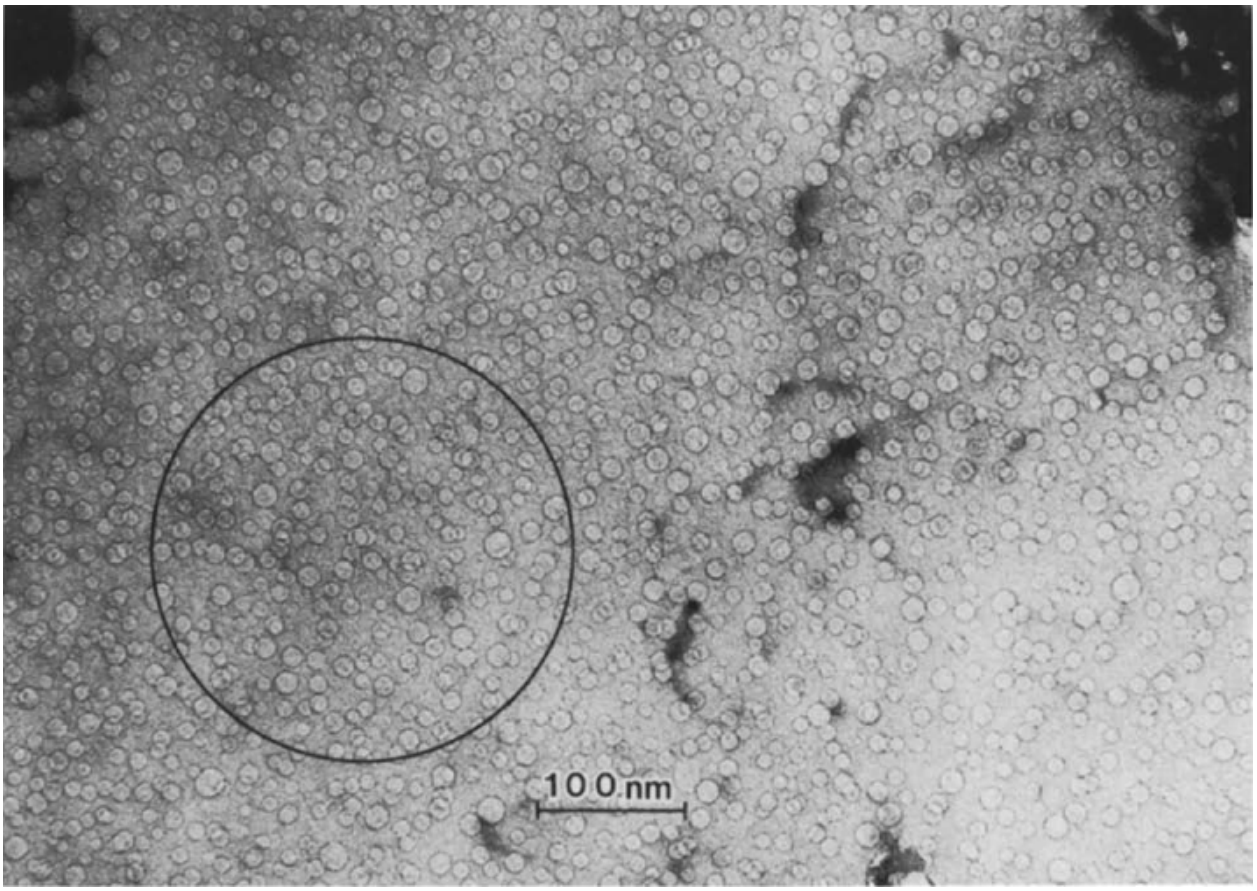

Figure 6.1: Micrograph from an aluminium sample which shows that the argon bubbles are uniformly distributed locally to the analysed region. The image is taken from [110].

neighbour) formation energy was determined as 1.38 eV.

Klaver and Chen [112] showed by DFT calculation that the $< 100 >$ dumbbell is the natural configuration for Al self-interstitials. They also calculated the formation energies of the Al $< 100 >$ dumbbell and octahedral self-interstitial and showed that the difference is no more than a few tenths of an eV.

Stumpf and Scheffler investigated several properties of Al dumbbell interstitials and Al surfaces using density-functional theory. Results of formation energies of surfaces, steps, adatoms and vacancies were reported in [113] and they find a very low energy barrier for Al dumbbell self-diffusion as 0.04 eV.

From the previous findings, the fcc Al system has a lower activation energy for vacancies to migrate in the system than bcc Fe lattice and also for the dumbbell interstitials (see Section 3.4, which gives 0.64 eV for Fe vacancy migration and 0.31 eV for the dumbbell interstitial migration barrier). The Ar bubbles in the fcc Al system appear more mobile.

In this chapter, the results of a study on the statics of small argon-vacancy clusters in fcc aluminium are presented, which will provide insight into how an argon bubble forms and grows. We also investigate the energy barriers that need to be overcome before growth by diffusion can occur and the mechanism of argon bubble formation in fcc Al.

6.2 Potential

For simulating the argon-vacancy clusters in the fcc aluminium system, a Lennard Jones potential modelled the interaction between Ar and the ZBL potential simulated the interaction between both Ar and Al, the Voter and Chen potential [47] is applied for Al, which is the same as used in [16] (see Section 2.1.3).

6.3 Formation Energy

First, we calculate the formation energy of several defects in the fcc Al system using the Voter-Chen potential.

Al cohesive energy	vacancy	divacancy	Al tetrahedral interstitial	Al octahedral interstitial	Al $< 100 >$ dumbbell interstitial	Al $< 110 >$ dumbbell interstitial	Al $< 111 >$ dumbbell interstitial
3.33 eV	0.63 eV	1.24 eV	2.53 eV	2.10 eV	2.06 eV	2.24 eV	2.50 eV

Table 6.1: The formation energy of Al defects in fcc Al.

The calculations in Table 6.1 are in agreement with the Ortega *et al.* results [111]. Results reveal that the $< 100 >$ Al dumbbell interstitial is the most stable configuration. The energy difference between the $< 100 >$ Al dumbbell interstitial and Al octahedral interstitial is tiny, which implies these two states could easily exchange at room temperature within MD time scales.

Ar substitutional	Ar tetrahedral interstitial	Ar octahedral interstitial	Ar substitutional with Al $< 100 >$ dumbbell interstitial in 1st neighbour
4.67 eV	7.07 eV	6.84 eV	6.36 eV

Table 6.2: The formation energy of Ar interstitials in fcc Al.

Table 6.2 shows that a single Ar atom in the fcc Al matrix is energetically favourable to locate as substitutional. The Ar substitutional atom is stable next to an Al dumbbell interstitial.

The formation energy of the argon-vacancy clusters Ar_nV_m in the fcc Al system is calculated using the Monte Carlo algorithm, which was introduced in Section 3.3.

Figure 6.2 shows the formation energy of the Ar_nV_m clusters at 0 K. Vacancies are preformed before Ar is inserted to generate these bubbles. To ensure the results can be compared on a similar scale, the figure shows the formation energy per vacancy. Each curve cannot be continued beyond the final point because the bubble will no longer be stable to

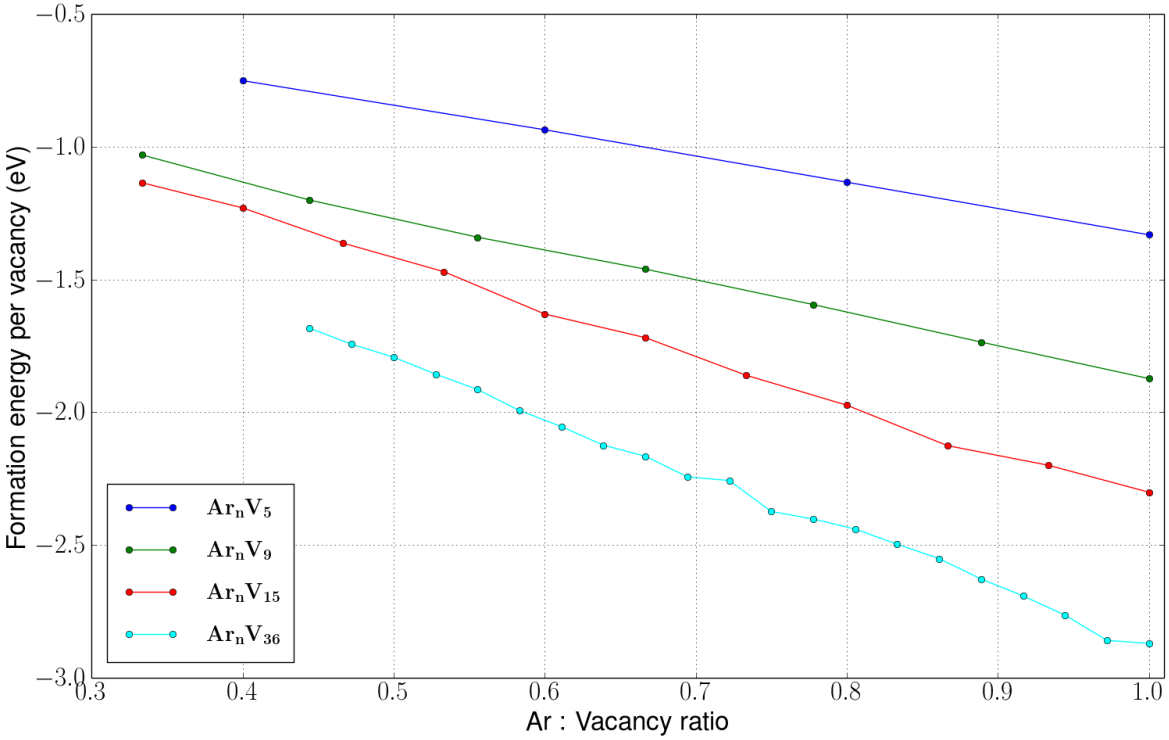

Figure 6.2: The formation energy as a function of the number of argon atoms for different sizes of Ar_nV_m clusters in fcc Al system.

hold more argon with the given number of vacancies; in other words, adding extra argon will push the neighbouring Al atoms into interstitials as shown in Figure 6.3. Each curve reveals the same decreasing trend which terminates at the 1 : 1 ratio. Further, after that, the bubbles will maintain the 1 : 1 ratio even adding extra Ar by emitting an Al dumbbell. This implies the 1 : 1 ratio is the optimal ratio for Ar bubbles in fcc Al lattice.

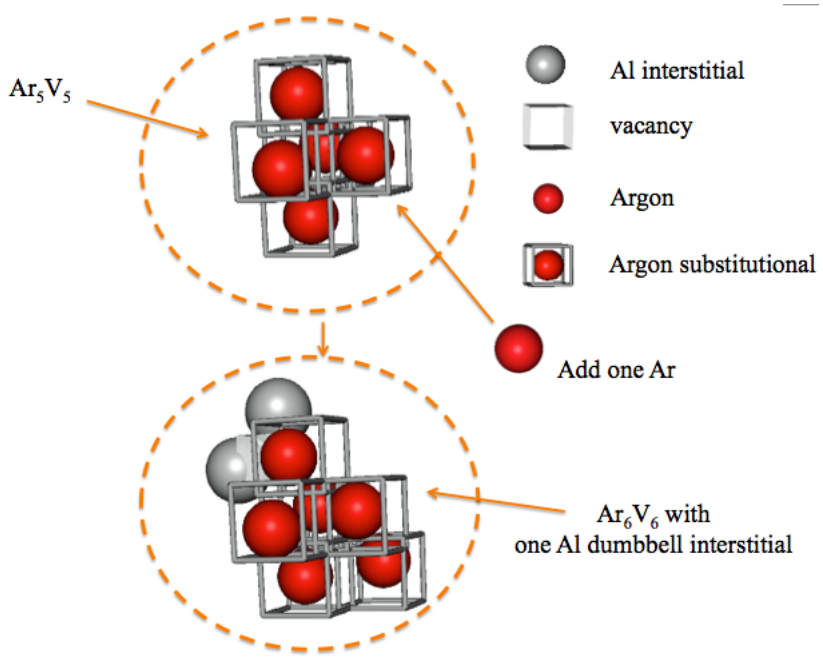

Figure 6.3: Illustration of the addition of adding an Ar atom to an Ar_nV_m bubble in Figure 6.2.

6.4 Diffusion mechanisms

To investigate the mechanism of Ar diffusion, saddle point searches have been done to find the possible transitions and the NEB method has been used to determine the barriers more accurately.

6.4.1 Diffusion of isolated defects in fcc Al without the presence of Ar

Before investigating how argon atoms diffuse in the fcc Al system, it is necessary to understand how an Al vacancy and interstitial diffuse since it will provide a reference to compare the Ar atoms' movement.

The results for the diffusion barriers of a single vacancy, $< 100 >$ dumbbell interstitial and octahedral interstitial to first neighbour and second neighbour positions are as shown in Table 6.3 and illustrated in Figures 6.4, 6.5 and 6.6.

defects	The energy barrier diffuse to 1 N	The energy barrier diffuse to 2 N
isolated vacancy	0.31 eV	> 5 eV
$< 100 >$ dumbbell interstitial	0.037 eV	0.098 eV
octahedral interstitial	0.05 eV	0.1 eV
octahedral interstitial to dumbbell interstitial	0.06 eV ($< 001 >$)	0.27 eV ($< 010 >$)

Table 6.3: The diffusion barrier of Al defects in fcc Al.

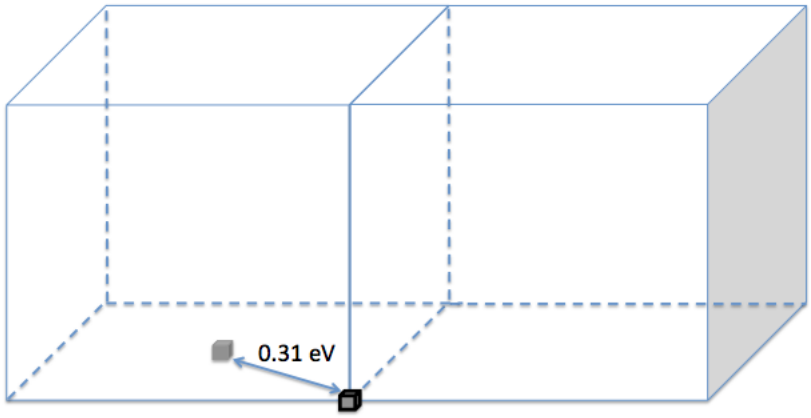

Figure 6.4: Illustration of the diffusion of an isolated Al vacancy with the forward and reverse barriers at 0.31 eV. The grey cube is the Al vacancy. The black outline represents the configuration after transition.

In Table 6.3, the barrier for an isolated Al vacancy to diffuse directly to its second neighbour could not be obtained by saddle point searches. Using the NEB method shows the barrier is more than 5 eV. This means a direct transition to 2nd neighbour is very unlikely.

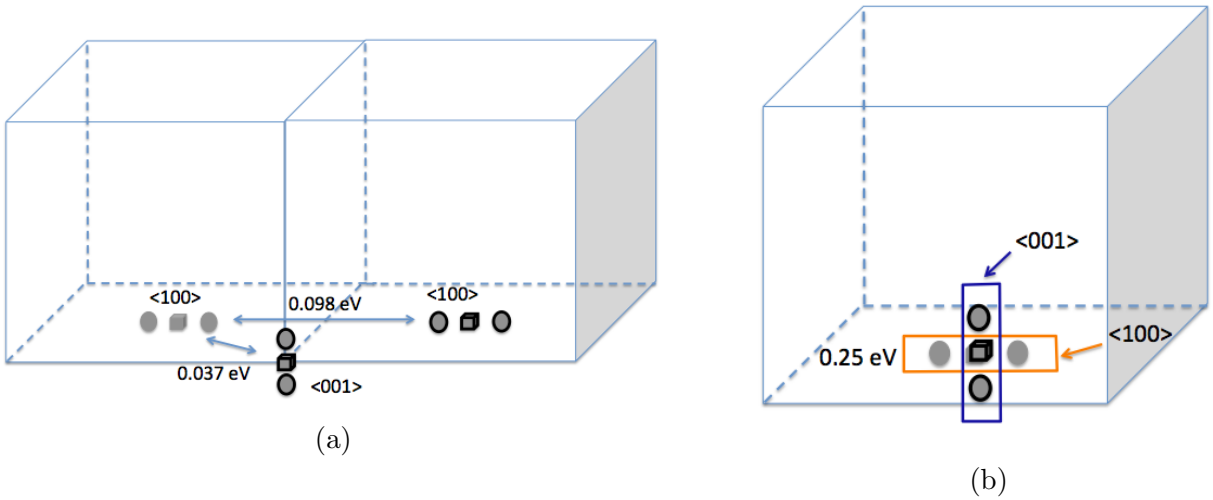

Figure 6.5: Illustration of the diffusion the Al $< 100 >$ dumbbell interstitial. The grey sphere is the Al interstitial and the grey cube is the Al vacancy. The black outline represents the configuration after transition. (a) Two diffusion mechanisms for the Al $< 100 >$ dumbbell interstitial. (b) The reorientation of the Al $< 100 >$ dumbbell interstitial.

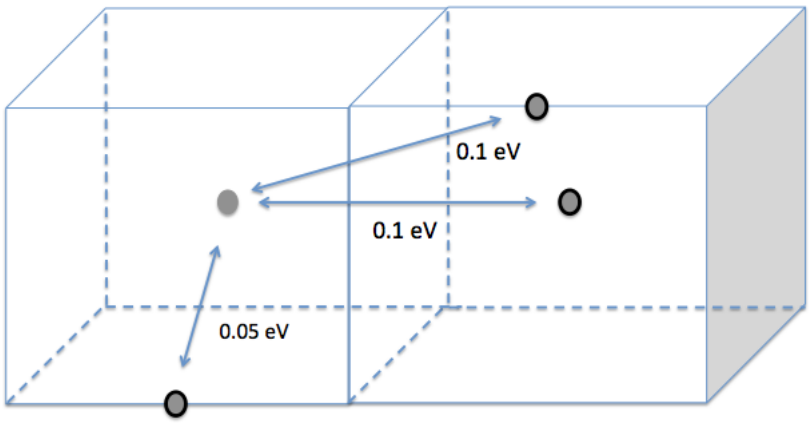

Figure 6.6: Illustration of diffusion of an Al octahedral interstitial. The grey sphere is the Al interstitial and the grey cube is the Al vacancy. The black outline represents the configuration after transition.

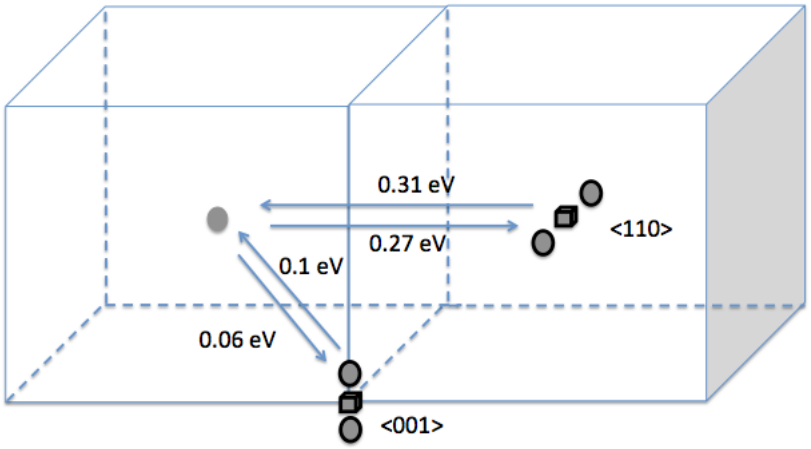

Figure 6.7: Illustration of the transition of Al octahedral interstitial to dumbbell interstitial. The grey sphere is the Al interstitial and the grey cube is the Al vacancy. The black outline represents the configuration after transition.

We have also checked the case of the divacancy. We find that the structure of divacancy allows one of the vacancies to diffuse with a much lower energy barrier than the isolated vacancy, see Figure 6.8.

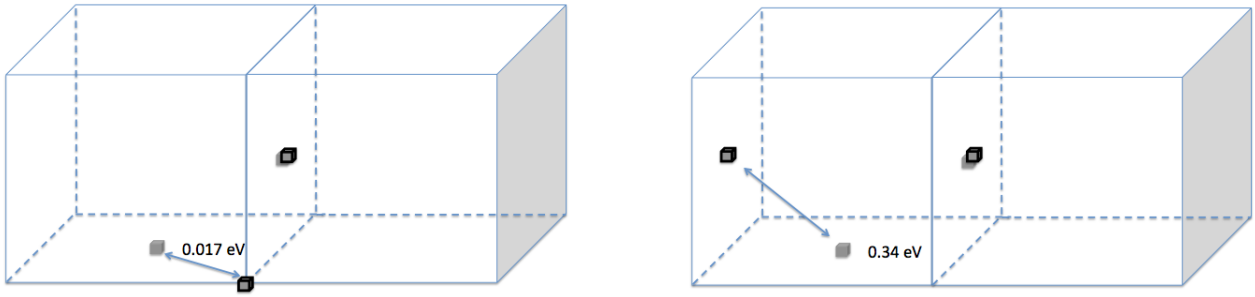

Figure 6.8: Illustration of the diffusion of the Al divacancy. The grey cube is the Al vacancy. The black outline represents the configuration after transition.

It is possible for both vacancies to diffuse within MD time scales. The energy barriers are slightly higher than the one for an isolated vacancy to migrate as shown in Figure 6.9.

A structure has been found with 0.06 eV energy lower than divacancy. The structure is consists of 3 vacancies located at each other's first neighbour site with an Al interstitial at the centre of this regular triangle as shown in Figure 6.10.

Due to the small energy barrier, the divacancy could exchange with the triangle configuration within 10 ps at room temperature and this triangle configuration could also diffuse

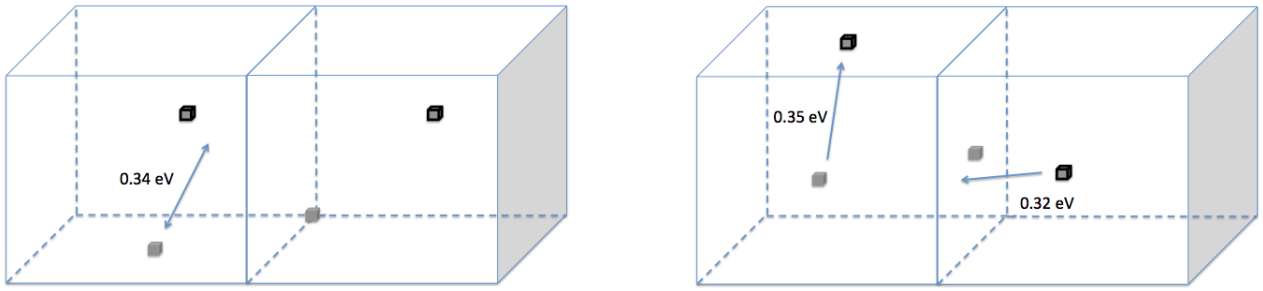

Figure 6.9: Illustration of the diffusion of the Al divacancy. The grey cube is the Al vacancy. The black outline represents the configuration after transition.

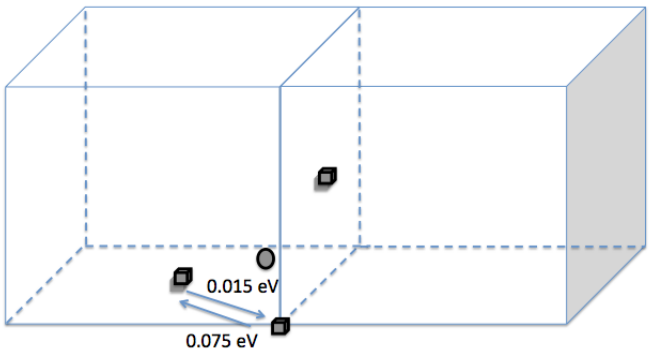

Figure 6.10: Illustration of the transition from the Al divacancy to the triangle cluster. The grey sphere is the Al interstitial and the grey cube is the Al vacancy. The black outline represents the configuration after transition.

within picoseconds time scales (see Figure 6.11). Therefore 2 vacancies diffuse more quickly than an isolated vacancy.

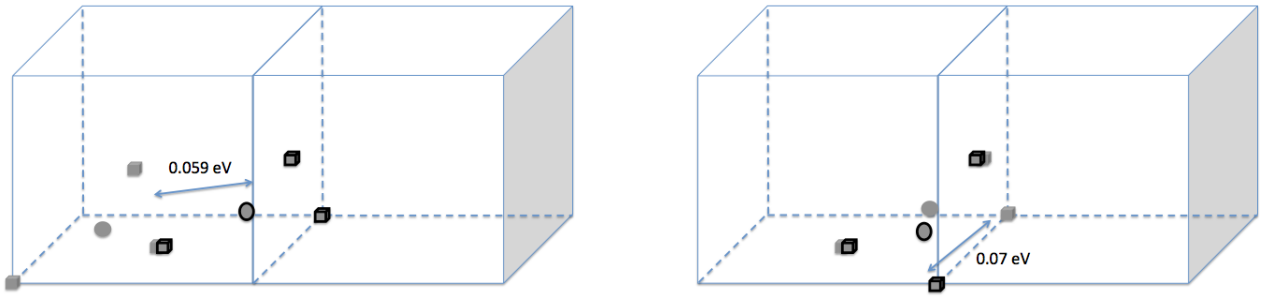

Figure 6.11: Illustration of the diffusion of the Al triangle cluster. The grey sphere is the Al interstitial and the grey cube is the Al vacancy. The black outline represents the configuration after transition.

In summary, Al vacancies and interstitials could diffuse quickly within MD time scales compared with the same defects in the bcc Fe system.

6.4.2 Ar in fcc Al

6.4.2.1 The Ar octahedral interstitial

In the fcc Al lattice, an Ar octahedral interstitial has a lower formation energy than the tetrahedral (see Table 6.2), which is different from the Ar interstitial in the bcc Fe system. The Ar octahedral interstitial could diffuse directly to another octahedral interstitial site with a small barrier 0.057 eV and it could diffuse to a subtetrahedral interstitial (0.5 $\sim$ 0.7 Å to a tetrahedral interstitial) site by forming a crowdion with a barrier of 0.09 eV. If the Ar interstitial goes into the substitutional site with an Al interstitial or Al dumbbell interstitial emitted, the barrier is less than 0.1 eV but the reverse barrier is $\sim$ 0.3 eV, which implies it is more kinetically favourable to become substitutional. The details of the transition is illustrated in Figure 6.12.

Therefore, the Ar interstitial would generally become substitutional. The lowest energy configuration is to form the substitutional Ar with an Al dumbbell interstitial.

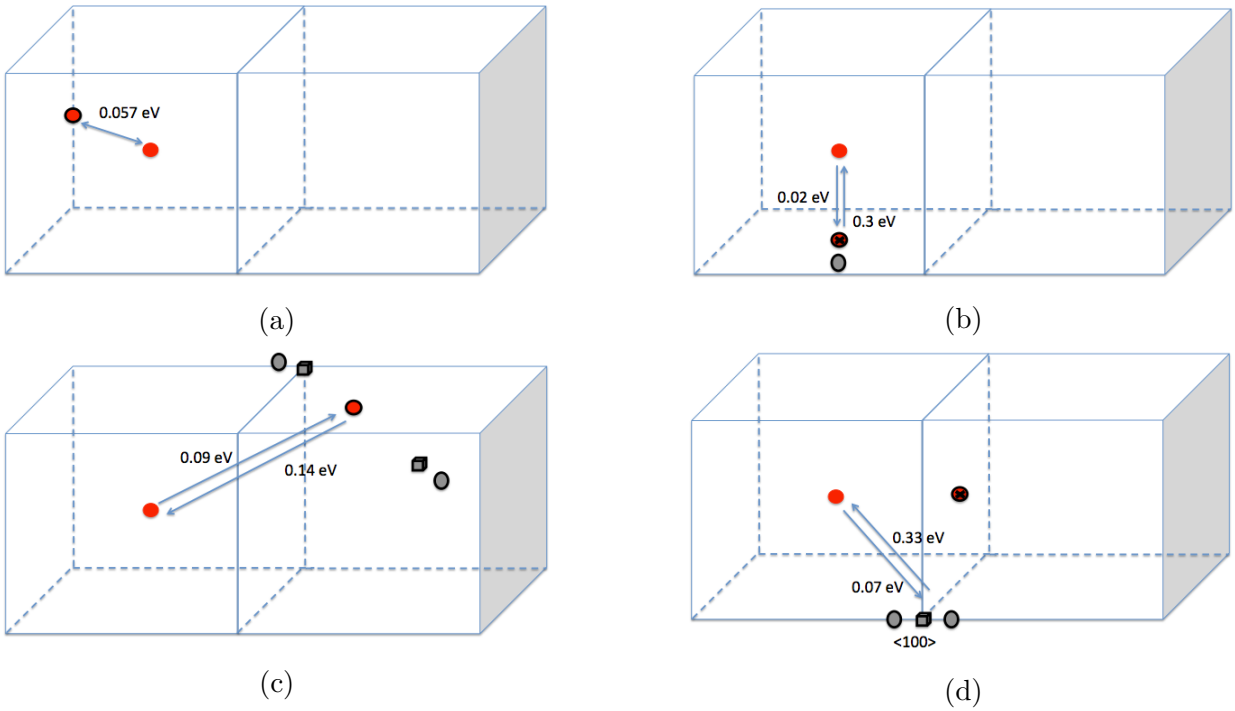

Figure 6.12: Illustration of the diffusion of Ar from the octahedral interstitial site with the associated forward and reverse energy barrier. The grey sphere is the Al interstitial and the grey cube is the Al vacancy. The black outline represents the configuration after transition. The red sphere is the Ar interstitial and the red sphere with the cross sign inside depicts the Ar substitutional atom. (a) The diffusion of the Ar octahedral interstitial to its neighbouring octahedral site with the forward and reverse energy barrier of 0.057 eV. (b) The diffusion of the Ar octahedral interstitial to the Ar substitutional with the Al interstitial with the energy barrier of 0.02 eV and reverse barrier 0.3 eV. (c) The diffusion of the Ar octahedral interstitial to the subtetrahedral interstitial with the crowdion structure with the energy barrier of 0.09 eV and reverse barrier 0.14 eV. (d) The diffusion of the Ar octahedral interstitial to the Ar substitutional with the Al dumbbell interstitial with the energy barrier of 0.07 eV and reverse barrier 0.33 eV.

6.4.2.2 The Ar interstitial with crowdion structure

As shown in Figure 6.12 and Figure 6.13a, the Ar interstitial with the crowdion structure can exchange with the Ar octahedral interstitial and the whole configuration could also diffuse with a small barrier of 0.1 eV (see Figure 6.13b). But an even lower energy transition is for an Ar to become substitutional with an Al dumbbell interstitial (0.07 eV). The details of the transition are illustrated in Figures 6.12d and 6.13a.

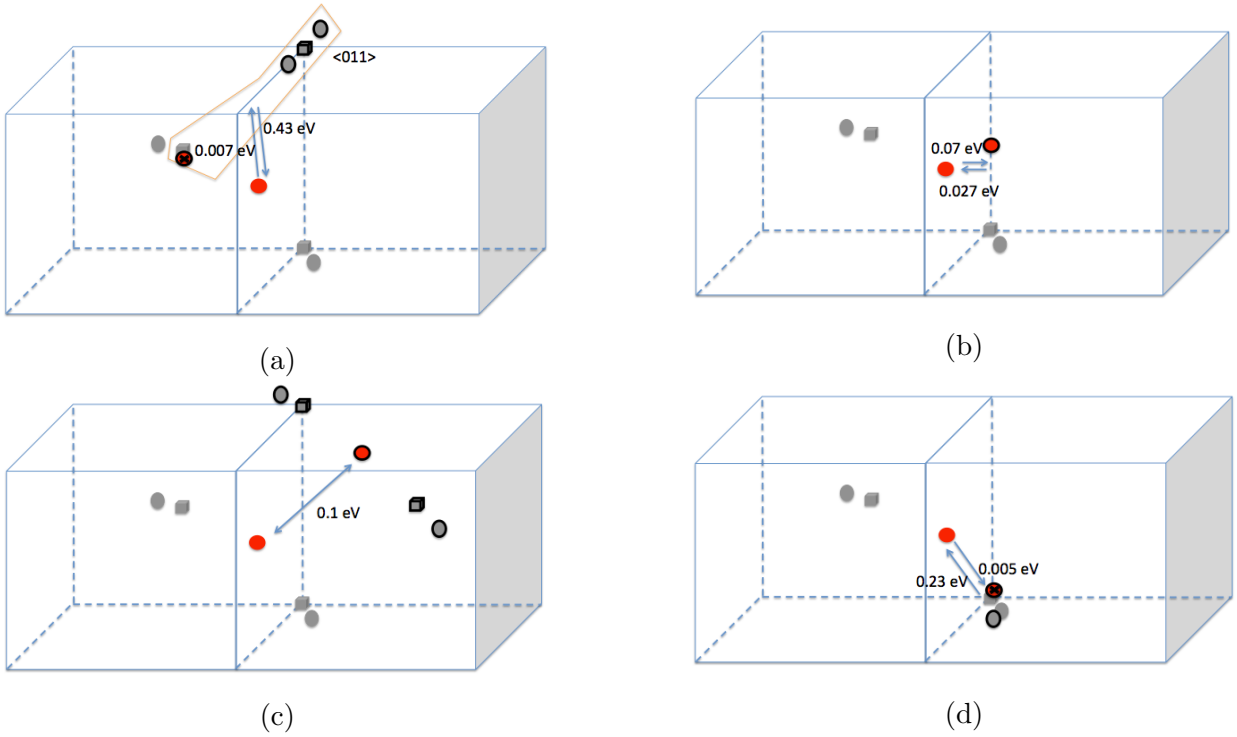

Figure 6.13: Illustration of the diffusion of the Ar interstitial from the crowdion initial position. The grey sphere is the Al interstitial and the grey cube is the Al vacancy. The black outline represents the configuration after transition. The red sphere is the Ar interstitial and the red sphere with the cross sign inside depicts the Ar substitutional atom. (a) The diffusion of the Ar subtetrahedral interstitial with the crowdion structure to the Ar octahedral interstitial with the energy barrier of 0.07 eV and reverse barrier 0.027 eV. (b) The diffusion of the Ar subtetrahedral interstitial with the crowdion structure with the forward and reverse barrier of 0.1 eV. (c) The diffusion of the Ar subtetrahedral interstitial with the crowdion structure to the Ar substitutional with the Al dumbbell interstitial with the energy barrier of 0.007 eV and reverse barrier 0.43 eV. (d) The diffusion of the Ar subtetrahedral interstitial with the crowdion structure to the Ar substitutional with the energy barrier of 0.005 eV and reverse barrier 0.23 eV.

6.4.2.3 Ar substitutional

Since the Ar substitutional atom is more stable than the interstitial and can easily form, it is necessary to understand transitions with an Al interstitial or dumbbell interstitial close by. The details of some transitions are illustrated in Figures 6.14 and 6.15.

6.4.2.3.1 Ar substitutional with Al dumbbell interstitial

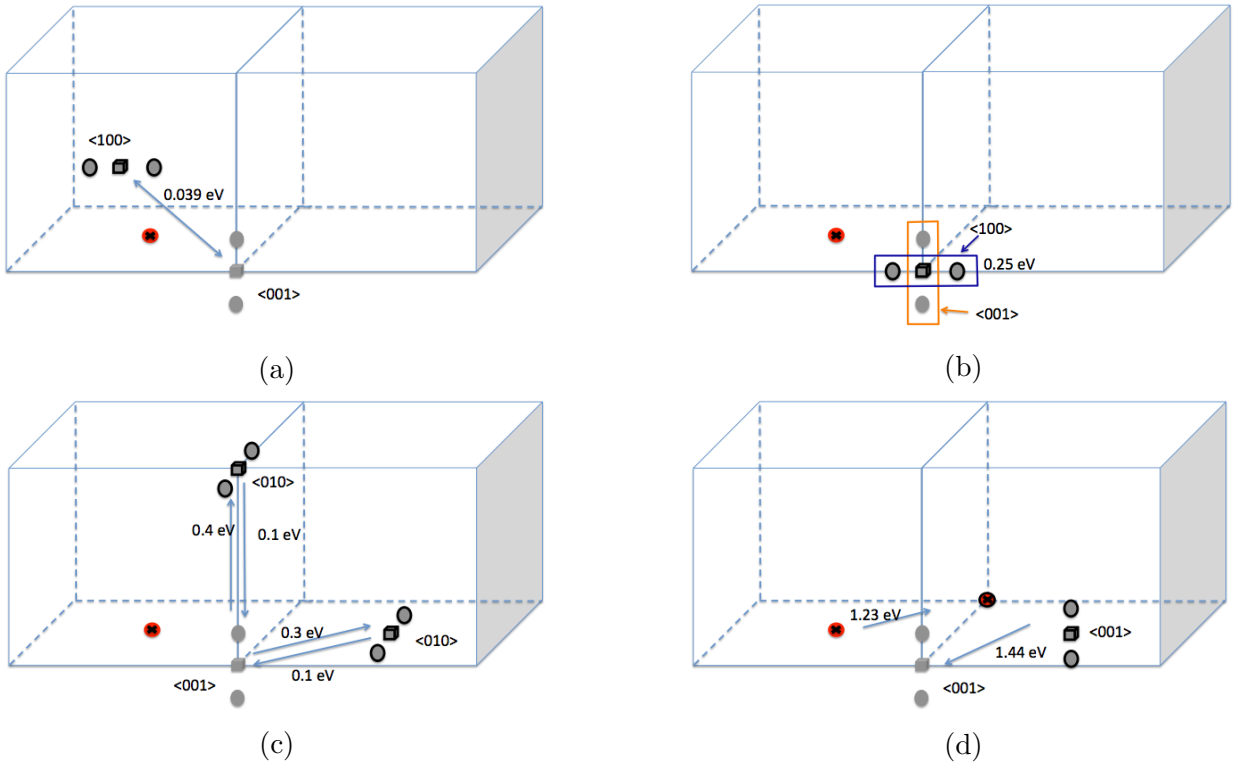

Figure 6.14: Illustration of the diffusion of the Al dumbbell interstitial with an Ar substitutional atom. The grey sphere is the Al interstitial and the grey cube is the Al vacancy. The black outline represents the configuration after transition. The red sphere is the Ar interstitial and the red sphere with the cross sign inside depicts the Ar substitutional atom. (a) Barriers for the reorientation of the dumbbell Al interstitial at different first neighbour cites of the Ar substitutional atom. (b) Barriers for the reorientation of the dumbbell Al interstitial at the same first neighbourhood of the Ar substitutional atom.. (c) Diffusion of the Al dumbbell interstitial away from the Ar substitutional atom. (d) Concerted joint motion of the Al dumbbell interstitial together with the Ar substitutional atom.

Figures 6.14a and 6.14c show that a dumbbell interstitial close to an Ar substitutional atom can diffuse away within nanoseconds at 500 K but it is kinetically favourable to surround the substitutional Ar atom in the first neighbour. Figure 6.14d shows that the joint

motion of an Ar substitutional with an Al dumbbell interstitial cannot occur within MD time scales at room temperature, but the Al split interstitial could easily diffuse away from the Ar substitutional as the barriers are low.

6.4.2.3.2 Ar substitutional with nearby Al interstitial

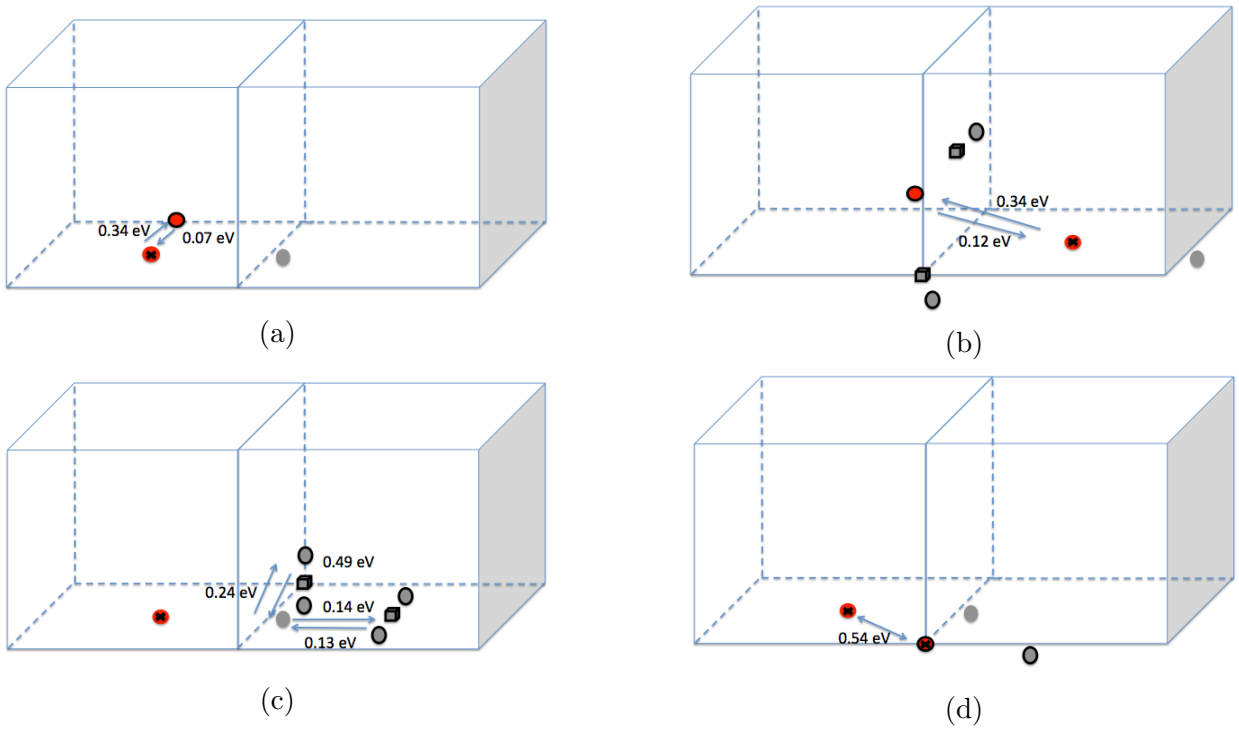

Figure 6.15: Illustration of the transition from an Ar substitutional atom with the Al interstitial. The grey sphere is the Al interstitial and the grey cube is the Al vacancy. The black outline represents the configuration after transition. The red sphere is the Ar interstitial and the red sphere with the cross sign inside depicts the Ar substitutional atom. (a) The diffusion of the Ar substitutional with the Al interstitial to the Ar octahedral interstitial with the energy barrier of 0.34 eV and reverse barrier 0.07 eV. (b) The diffusion of the Ar substitutional with the Al interstitial to the Ar subtetrahedral interstitial with the crowdion structure with the energy barrier of 0.34 eV and reverse barrier 0.12 eV. (c) Diffusion of the Al interstitial away from the Ar substitutional into dumbbell interstitial. (d) Concerted joint motion of the Al interstitial together with the Ar substitutional.

When close to the Ar substitutional atom, the Al interstitial can evolve into the dumbbell interstitial in the first or second neighbour position, see Figure 6.14c. The barrier to turn the Al interstitial into an Al dumbbell interstitial in the second neighbour is lower than for the first neighbour. However, if we compare the migration barrier of Al interstitial or

dumbbell interstitial in a pure fcc Al system (see Table 6.3), with the presence of Ar, the barriers are higher. The Ar substitutional atom could also return to an interstitial site within nanoseconds. It is possible for the Ar substitutional to diffuse with Al interstitial over nanoseconds (see Figure 6.15d) but the initial configuration is unlikely to arise because it is less favourable than the dumbbell configuration.

In summary, a substitutional Ar atom with an Al dumbbell interstitial is the lowest energy configuration for Ar but for this configuration to move, the energy barrier is very high as shown in Figure 6.14d.

6.4.2.3.3 Isolated Ar substitutional

So far, it is clear that the isolated Ar atom is favoured to become substitutional with a bounded Al dumbbell interstitial in its first neighbour position. Although the dumbbell interstitial is not favoured to diffuse away from the Ar, it is still possible to happen within nanoseconds at room temperature. Hence we want to investigate the stability and mobility of an isolated Ar substitutional.

It was found that the Ar substitutional atom can not move to the interstitial site within the 3rd octahedral neighbouring positions (using the octahedral interstitial site is because the Ar octahedral interstitial gets a lower energy than the tetrahedral interstitial, see Table 6.2). The reason is that the configuration of the Ar interstitial with a vacancy within the 3rd neighbour is not stable after minimisation. In other words, the Ar atom will instantaneously occupy the vacancy within its 3rd neighbour to become substitutional. The substitutional Ar can move to the interstitial site from the 4th neighbour site with leaving the vacancy (see Figure 6.16). However, the energy barrier is more than 2.8 eV. Further, the barrier for the Ar substitutional atom to diffuse to the neighbour substitutional site is over 5 eV.

To investigate the further details, we have also checked the case that an Ar octahedral interstitial atom with a vacancy in different neighbour position for a comparison. If the vacancy sits within the 2nd neighbour position of the Ar interstitial, the Ar atom will

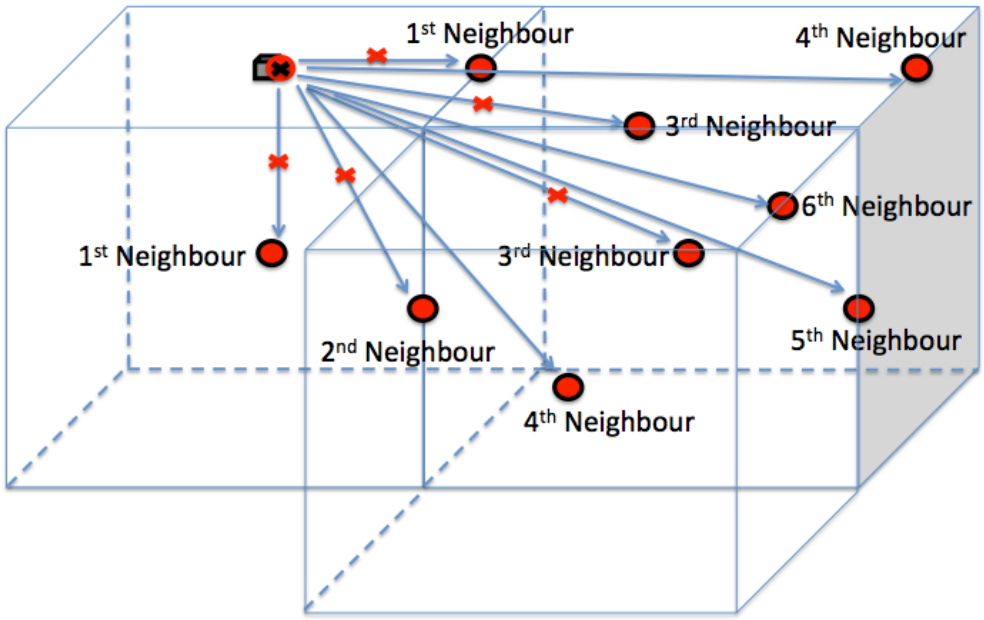

Figure 6.16: Illustration of the possibility of the Ar substitutional atom to become an interstitial Ar leaving a vacancy. The red sphere is the Ar interstitial and the red sphere with the cross sign inside depicts the Ar substitutional atom. The grey cube is the Al vacancy and will disappear afterwards. The black outline represents the configuration after transition. The red cross sign indicts the transition is impossible.

instantaneously move to the vacancy site to become substitutional, which we mentioned above. When the vacancy locates at the the 3rd neighbour position, after minimisation, the vacancy will move to the first neighbour position of the Ar interstitial and the Ar will become substitutional there as shown in Figure 6.17a. When the vacancy sits from the 4th neighbour outwards of the Ar, the Ar atom will become substitutional in the first neighbour of its previous interstitial site as shown in Figure 6.17b. The forward barrier is only 0.04 eV but the reverse barrier is 2.8 eV.

Therefore, the Ar substitutional is found to be unmovable at 500 K rather than diffusion. Additional vacancies are needed for the diffusion of Ar, which will be explained in the following section.

6.4.2.4 Ar substitutional with vacancies nearby

6.4.2.4.1 Ar substitutional with a vacancy nearby

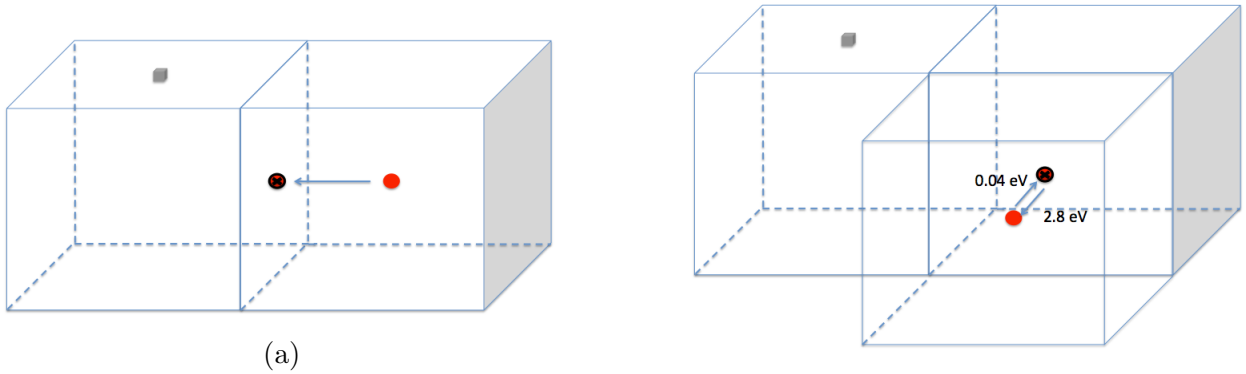

(a) (b)

Figure 6.17: Illustration of the transition from an Ar interstitial atom with a vacancy nearby. The red sphere is the Ar interstitial and the red sphere with the cross sign inside depicts the Ar substitutional atom. The grey cube is the Al vacancy and will disappear afterwards. The black outline represents the configuration after transition. (a) The Ar interstitial atom with a vacancy in the third neighbour position becomes a substitutional Ar in the position of the first neighbour of the previous Ar interstitial site after minimisation. (b) The Ar interstitial atom with a vacancy in the fourth neighbour position becomes a substitutional Ar in the position of the first neighbour of the previous Ar interstitial site. The forward barrier is 0.04 eV and the reverse barrier is 2.8 eV.

After minimisation, an Ar substitutional atom is not stable with a vacancy in the first neighbour position. The configuration will change into a split vacancy shape (i.e. 2 vacancies with the Ar interstitial in the middle of them). The argon substitutional becomes stable with the vacancy located in the second neighbour position or further. The energy for this is 0.7 eV higher than the split vacancy configuration. The details of the transition for the split vacancy is illustrated in Figure 6.18.

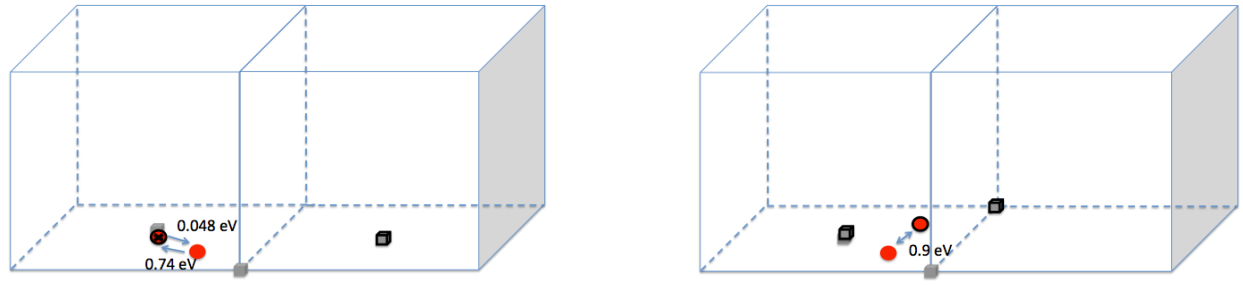

(a) (b)

Figure 6.18: Illustration of the transition from the initial Ar split vacancy. The grey sphere is the Al interstitial and the grey cube is the Al vacancy. The black outline represents the configuration after transition. The red sphere is the Ar interstitial and the red sphere with the cross sign inside depicts the Ar substitutional atom. (a) The diffusion of the Ar substitutional atom with a vacancy in the second neighbour to the Ar split vacancy with the energy barrier of 0.048 eV and reverse barrier 0.74 eV. (b) Diffusion of the Ar split vacancy with the forward and reverse barrier 0.9 eV.

The split vacancy configuration can diffuse with a barrier of 0.9 eV (see Figure 6.18b). A free vacancy close to the substitutional Ar can drag the Ar atom away from the vacancy site to form the split vacancy shape (see Figure 6.18a). Taking the energy barrier of migration energy of Al vacancy into account (see Figure 6.4), the Ar substitutional atom in fcc Al is not as stable as the substitutional Ar in bcc Fe.

6.4.2.4.2 Ar substitutional with 2 vacancies nearby

Two free vacancies can diffuse away from an Ar substitutional atom with a small barrier, or they could form an Al triangle cluster which can also diffuse away with a small barrier. But these transitions are not favoured. The details are shown in Figures 6.19 and 6.20.

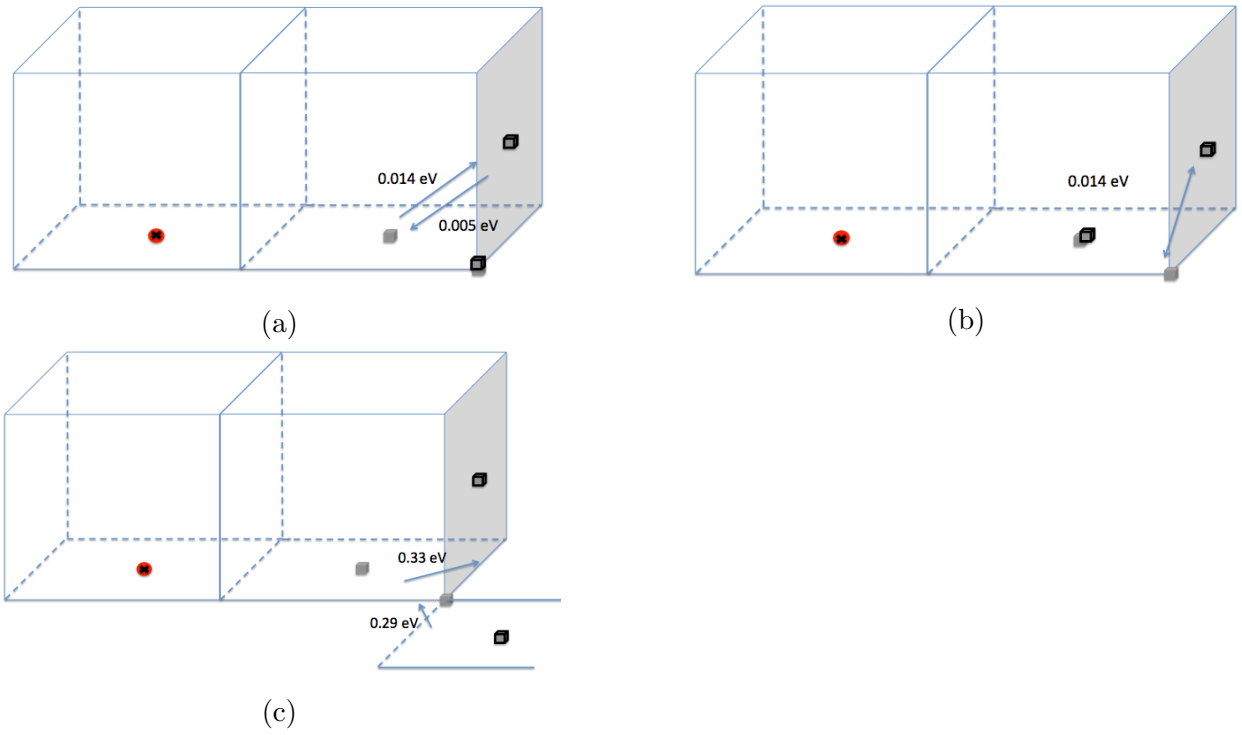

Figure 6.19: Illustration of the diffusion of the 2 vacancies in 2nd and 5th neighbour with an Ar substitutional atom. The grey sphere is the Al interstitial and the grey cube is the Al vacancy. The black outline represents the configuration after transition. The red sphere is the Ar interstitial and the red sphere with the cross sign inside depicts the Ar substitutional atom. (a) The vacancy moves from the 2nd neighbour to 5th neighbour with the forward barrier of 0.014 eV and reverse barrier of 0.005 eV. (b) The vacancy moves from the 5th neighbour site to another 5th neighbour site with the forward and reverse barrier of 0.014 eV. (c) Both vacancies move away from the Ar atom with the forward barrier of 0.33 eV and the reverse barrier is 0.29 eV.

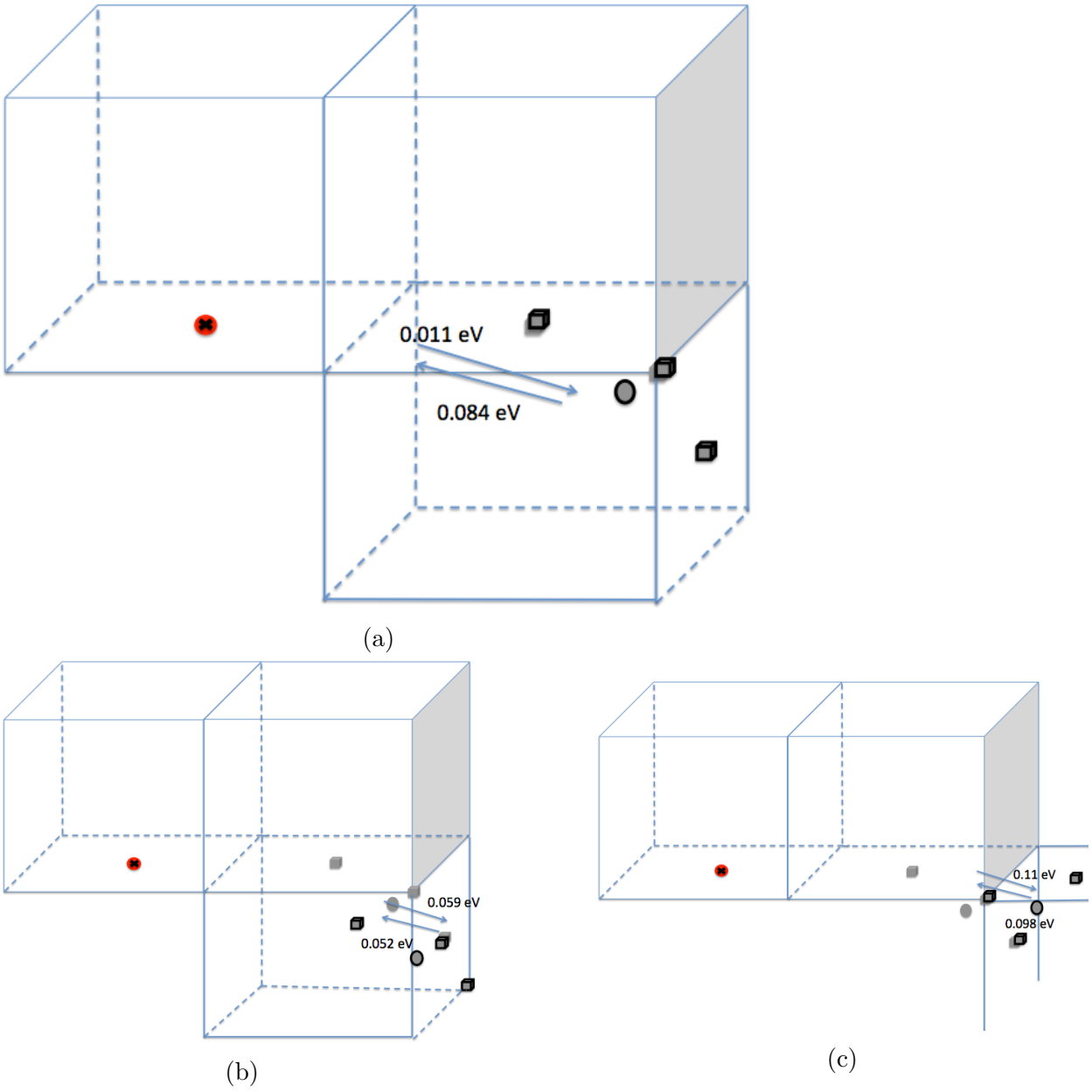

Figure 6.20: Illustration of the diffusion of the Al triangle cluster with an Ar substitutional atom. The grey sphere is the Al interstitial and the grey cube is the Al vacancy. The black outline represents the configuration after transition. The red sphere is the Ar interstitial and the red sphere with the cross sign inside depicts the Ar substitutional atom. (a) The diffusion of the 2 vacancies in 2nd and 5th neighbour with an Ar substitutional atom to the Al triangle cluster with keeping the Ar substitutional with the forward barrier of 0.011 eV and the reverse barrier of 0.084 eV. (b) The diffusion of the Al triangle cluster with an Ar substitutional atom. (c) The diffusion of the Al triangle cluster with an Ar substitutional atom.

Compared with the two vacancies without the presence of Ar (see Figures 6.8, 6.9, 6.10 and 6.11), the two free vacancies are favoured to diffuse towards the Ar substitutional atom with even a smaller barrier. Then the Ar substitutional is no longer stable; it will turn into split vacancy configuration as shown in Figure 6.21.

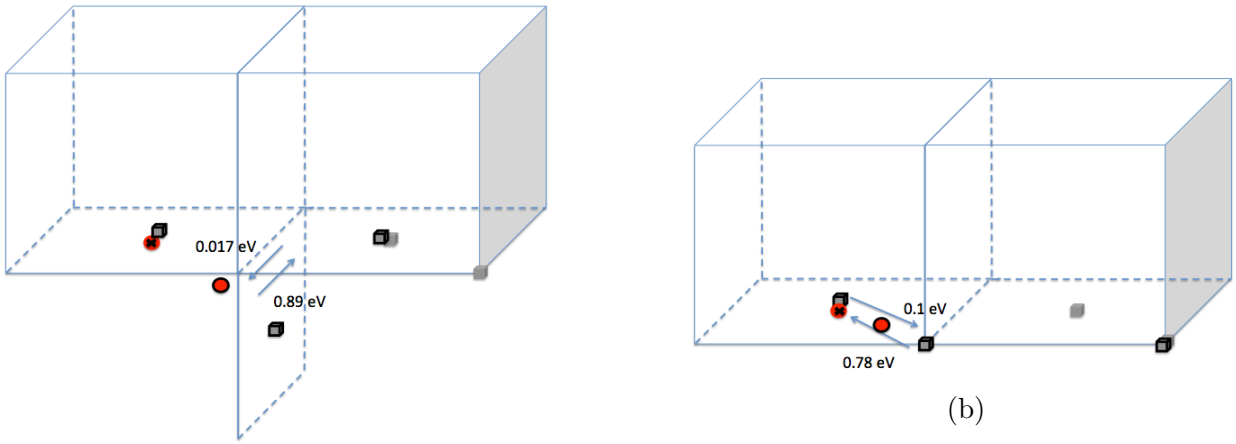

(a) (b)

Figure 6.21: Illustration of the transition of Ar substitutional with 2 vacancies in 2nd and 5th neighbour to the Ar split vacancy with one free vacancy. The grey sphere is the Al interstitial and the grey cube is the Al vacancy. The black outline represents the configuration after transition. The red sphere is the Ar interstitial and the red sphere with the cross sign inside depicts the Ar substitutional atom. (a) The transition of an Ar substitutional atom with 2 vacancies in 2nd and 5th neighbour sites to the Ar split vacancy with keeping the previous vacancy in the 2nd neighbour with the forward barrier of 0.017 eV and the reverse barrier of 0.89 eV. (b) The transition of an Ar substitutional atom with 2 vacancies in 2nd and 5th neighbour sites to the Ar split vacancy keeping the previous vacancy in the 5th neighbour site with the forward barrier of 0.1 eV and the reverse barrier of 0.78 eV.

After the split vacancy configuration has been generated, the free vacancy could diffuse away but this is not favoured (see Figure 6.22). If the free vacancy is close to the split vacancy configuration (see the initial configuration in Figure 6.22), the Ar could oscillate locally with the movement of these vacancies surround it (see Figure 6.23). The structure of the split vacancy will evolve into an Ar interstitial located in the centre of a triangle consisting of 3 Al vacancies (see Figure 6.23e), which is the lowest energy configuration.

Figures 6.23a, 6.23b, 6.23c and 6.23d all show the identical configuration with the initial configuration in Figure 6.23a. This structure is 0.7 eV higher than the vacancy triangle with the Ar at its centre shown as the final configuration of Figure 6.23e. This triangle can diffuse with a barrier of 0.85 eV (see Figure 6.24).

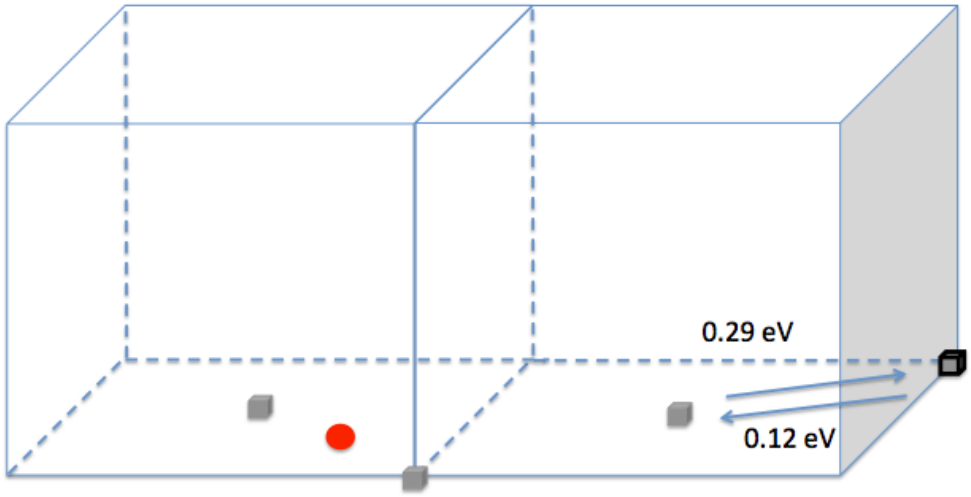

Figure 6.22: Illustration of the vacancy away from the Ar split vacancy with the forward barrier of 0.29 eV and the reverse barrier of 0.12 eV. The grey sphere is the Al interstitial and the grey cube is the Al vacancy. The black outline represents the configuration after transition. The red sphere is the Ar interstitial and the red sphere with the cross sign inside depicts the Ar substitutional atom.

Overall, two free vacancies are more activated than one vacancy; they can diffuse more quickly towards the Ar and attract the Ar from the vacancy site to form small cluster. Then the configuration can diffuse with a barrier around 0.85 eV, which is much lower than the barrier found for Ar in bcc Fe (see Section 4.4.2).

6.5 Conclusions

Similar to Ar in the bcc Fe system, Ar atoms in fcc Al are also favoured to become substitutional and the optimal Ar-to-vacancy ratio of Argon bubbles is also 1 : 1. However, the Ar substitutional atom in fcc Al is not as stable as in bcc Fe. The barriers for an Ar substitutional atom with an Al interstitial or a dumbbell interstitial to diffuse or become only an Ar interstitial is much smaller than the barriers found in bcc Fe. Further, the migration energy barrier for vacancies in fcc Al could diffuse faster than in bcc Fe. When free vacancies approach the Ar substitutional atom, they could attract the Ar from the substitutional site to form an Ar-vacancy cluster, which could diffuse with a smaller barrier than the one we found in bcc Fe. The hop time for this is around 2 seconds at room temperature. Thus Ar

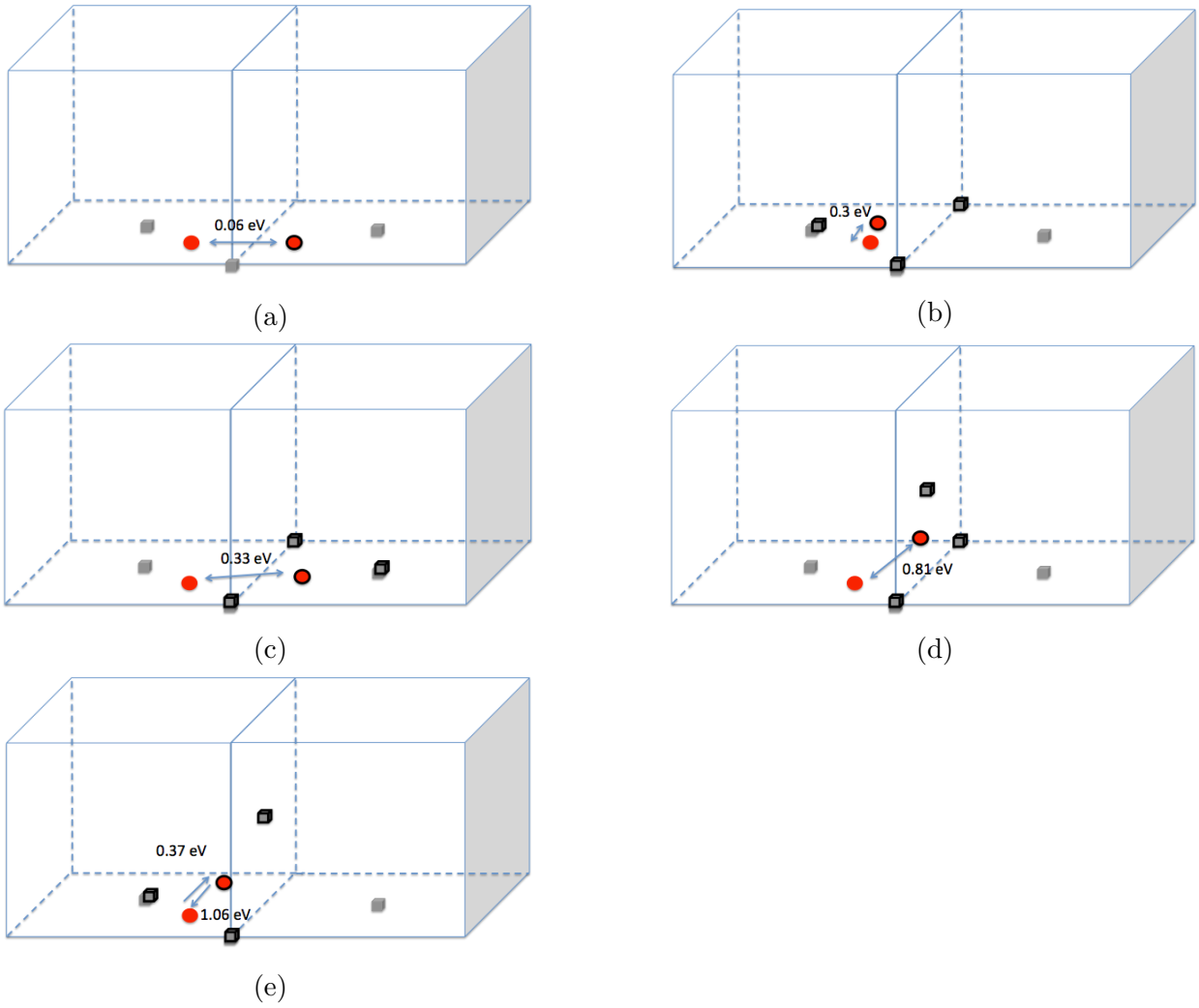

Figure 6.23: Illustration of the transition of the Ar split vacancy with a close by vacancy to the Ar triangle cluster. The grey sphere is the Al interstitial and the grey cube is the Al vacancy. The black outline represents the configuration after transition. The red sphere is the Ar interstitial and the red sphere with the cross sign inside depicts the Ar substitutional atom. (a) The jump of the Ar between these three vacancies with keeping the configuration of the Ar split vacancy with a vacancy with the forward and reverse barrier of 0.06 eV. (b) The initial configuration shown in (a) can have one vacancy moving to the first neighbour site of its original position with a jump of the Ar between these three vacancies. The whole structure is still kept with the forward and reverse barrier of 0.3 eV. (c) The initial configuration shown in (a) can have one vacancy moving to the first neighbour site of its original position with a further jump of the Ar than (b). The whole structure is still kept with the forward and reverse barrier of 0.33 eV. (d) The initial configuration shown in (a) can reorient the structure with the movement of Ar and vacancies. The forward and reverse barrier is 0.81 eV. (e) The configuration shown in (a) forms a vacancy triangle with the Ar interstitial at its centre. The forward barrier is 0.37 eV and the reverse barrier is 1.06 eV.

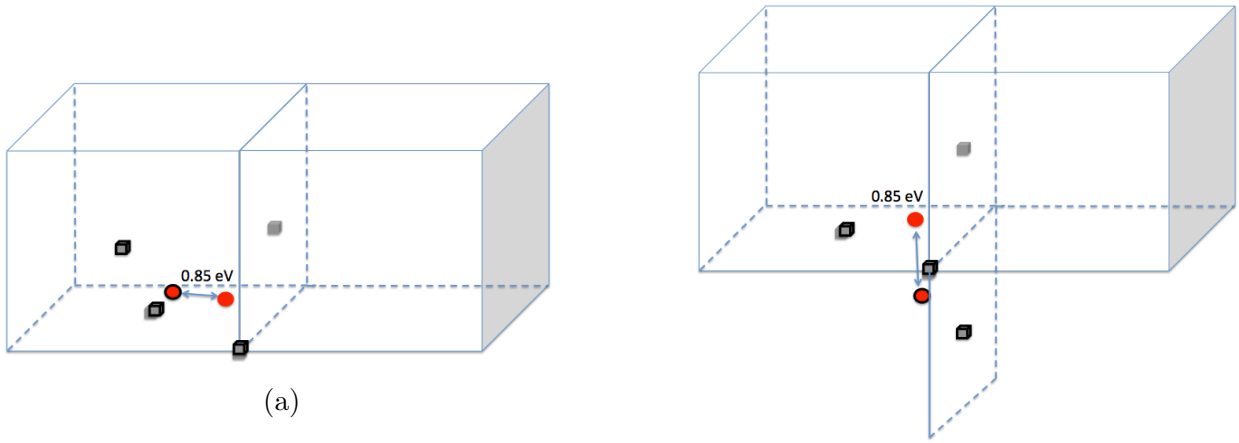

(a) (b)

Figure 6.24: Illustration of the diffusion of the Ar triangle cluster. The grey sphere is the Al interstitial and the grey cube is the Al vacancy. The black outline represents the configuration after transition. The red sphere is the Ar interstitial and the red sphere with the cross sign inside depicts the Ar substitutional atom. (a) The diffusion of the Ar interstitial atom with the movement of one vacancy to the first neighbour site of its original position. The forward and reverse barrier is 0.85 eV. (b) The diffusion of the Ar interstitial atom with the movement of one vacancy to the second neighbour site of its original position. The forward and reverse barrier is 0.85 eV. (a) and (b) show that this triangle cluster could diffuse in three dimensions.

can diffuse via a vacancy mechanism.

Chapter 7

Conclusions and Future Work

7.1 Conclusions

Static calculations show the optimal He-to-vacancy ratio at 0K varies from 1 : 1 up to 4 : 1 for different sizes of He-vacancy clusters in bcc Fe lattices. If such bubbles are subjected to radiation, then they can be modified. At the optimal ratio or above, vacancy capture is favoured, which gives a mechanism for He bubble growth. He interstitials are highly mobile and could diffuse towards and join a bubble for a wide range of He : vacancy ratios if the size is under $\sim$ 1.4 nm. When bubbles reach this size, He diffusion to enlarge the bubble becomes unfavoured due to the lattice strain around it. For this size of the bubble, radiation cascades provide a way to add the additional vacancies required for He to enlarge the bubble.

The Ar-vacancy clusters in bcc Fe are favoured in the 1 : 1 ratio at 0 K. Extra Ar added into a bubble with a 1 : 1 ratio will cause the emission of Fe to keep the same ratio. At 500 K, with an interaction with 1 keV cascades, Ar bubbles with the optimal ratio could emit Fe and gain additional vacancies to obtain a lower ratio than 1 : 1 to enlarge the bubbles. Extra Ar interstitials in a neighbourhood of an existing Ar bubble with a diameter less than 1.2 nm will join the bubble with a small energy barrier. However, isolated Ar interstitials diffuse more slowly than He in bcc Fe and they are favoured to become substitutional with

a barrier of 0.07 eV. If the Ar bubble reaches a certain size, nearby Ar atoms will become substitutional rather than join the bubble. The diffusion of isolated Ar relies on a vacancy driven mechanism.

Xe atoms in bcc Fe have similar properties to Ar. The optimal Xe : vacancy ratio for Xe bubbles varies from 0.6 to 0.8 : 1. Radiation events could enable the optimal Xe bubbles to reduce the ratio by enlarging the bubble through emission of Fe. It is even more difficult for the isolated Xe atom to diffuse in bcc Fe lattice than Ar. A vacancy driven mechanism can make the diffusion possible with a high barrier.

Different from Ar in bcc Fe, in fcc Al, the Ar interstitials could diffuse with a lower energy barrier. They are also favoured to become substitutional within picoseconds at room temperature. After the trap mutation, the Ar substitutional is stable with the formed Al dumbbell interstitial. Free vacancies can diffuse more quickly than those in the bcc Fe system. They could attract the Ar from the substitutional site to form an Ar-vacancy triangle cluster. The diffusion of these clusters is possible with a lower barrier than the one we found in bcc Fe.

7.2 Future Work

7.2.1 The structure of Xenon Bubbles in fcc Al

Work over a number of years has been carried out by the group of Donnelly in the regard to xenon particles embedded in Al crystals [17, 18, 19, 20, 21]. In [17], they point out the Xe particle had an fcc structure with the same orientation as the Al matrix and also observed the Xe bubbles in pure Al matrices [18, 21] with the cuboctahedral shape composed of {111} and {200} facets.

Future work could examine these large clusters and compare the energetics of Xe embedded in a sphere void and a cuboctahedral shape.

Some preliminary results are given simulating the xenon-vacancy clusters in the fcc alu-

minium system, where the ZBL potential was used for the Xe-Al interaction.

A spherical void can be generated by removing atoms from a centre point in the crystal with an adjustable radius. Thus there are two factors to determine the number of vacancies: the position of the centre of the void and the radius of the sphere. This is illustrated in Figure 7.1.

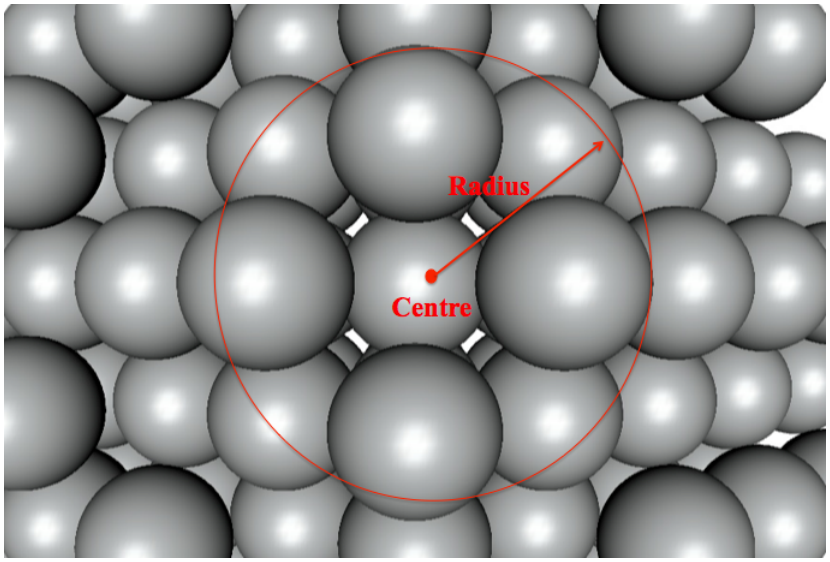

Figure 7.1: The 2D graph to illustrate the way to generate the spherical void. The grey atoms represent Al atoms.

Compared with the universality of the spherical void, the regular cuboctahedral shape is only valid for some fixed number of vacancies. If we relax the limitation in this way that the cuboctahedron is nonregular, we could get more cases at the sacrifice of some symmetry (see Figure 7.2). The following case could illustrate this.

We compare the system energy of both ways to generate the same bubbles and list in Tables 7.1 and 7.2. The reason to choose the $1:1$ ratio is empirical. Because the $1:1$ ratio is allowed for Xe in fcc Al and it could retain the cuboctahedral structure after minimisation.

It is clear that for the cases that the regular cuboctahedral shape could be applied, the spherical configuration has a slightly higher energy, but by checking the energy per vacancy, this difference is within the reasonable tolerance of statistics. If we check the other cases that we relax the limitation, there is no clear conclusion to make a judgement. But the

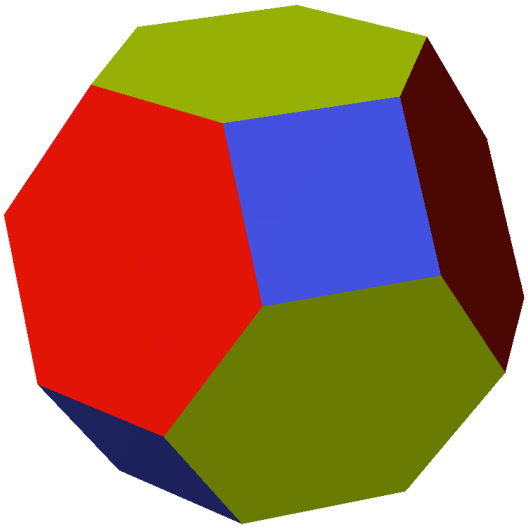

(a)

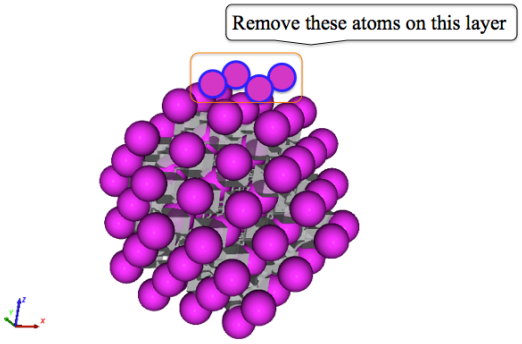

(b)

Figure 7.2: (a) is the diagram to show the regular cuboctahedral shape. (b) is using 2D to illustrate the way to generate the nonregular cuboctahedral void. The grey cubes represent Al vacancies and pink spheres are Xe atoms.

Bubble	system energy (eV) in spherical way	system energy (eV) in cuboctahedral way	energy difference per vacancy (eV)
$Xe_{79}V_{79}$	-359498.47	-359499.42	0.012
$Xe_{201}V_{201}$	-359064.97	-359070.05	0.025
$Xe_{405}V_{405}$	-358352.33	-358356.14	0.0094

Table 7.1: Comparison of two ways to form bubbles. The cuboctahedral here is regular.

Bubble	system energy (eV) in spherical way	system energy (eV) in cuboctahedral way	energy difference per vacancy (eV)
$Xe_{201}V_{170}$	-359163.72	-359161.27	0.014
$Xe_{213}V_{218}$	-359005.98	-359002.45	0.016
$Xe_{250}V_{247}$	-358902.17	-358904.51	0.011
$Xe_{330}V_{328}$	-358619.76	-358622.59	0.0086
$Xe_{378}V_{370}$	-358472.29	-358472.96	0.0018
$Xe_{116}V_{116}$	-359369.43	-359369.43	0

Table 7.2: Comparison of two ways to form bubbles.

energy differences imply the consistent conclusion with the regular case. Even we found for $Xe_{116}V_{116}$, the two ways of construction lead to an identical relaxed structure, which make sense because for a small cuboctahedron, it could be taken as the approximation of the sphere. However, in Figure 7.3, after minimisation, we have the nonregular cuboctahedral shape for both ways.

Figure 7.3: The configurations of bubble $Xe_{116}V_{116}$. From left to right: spherical way before minimisation, spherical way after minimisation, cuboctahedral way before minimisation, cuboctahedral way after minimisation. The grey cubes represent Al vacancies and pink spheres are Xe atoms.

In this preliminary investigation there is no significant difference between using spherical void and cuboctahedron taking the statistics into account. For the smaller bubbles, the cuboctahedral structure has approximately the same shape for the spherical configuration. This problem can be investigated in more detail to obtain a much better understanding of large Xe bubbles in Al and better statistics to draw informed conclusions.

7.2.2 Other potential work

The most detailed work in the thesis concerned He bubbles in bcc Fe since these are the most problematical for causing structural weaknesses in reactor pressure vessels. However the same detailed methodology as used for He could also be extended to other systems including He, Ar, Kr and Xe. The reason that Kr was not considered in the thesis although it is an important nuclear transmutation project was due to time considerations and because its mass lies somewhere between those of the other inert gases. Besides the materials considered in the thesis inert gas bubbles in an ODS alloys could be considered since ODS steels show a good radiation resistance. Previous work by our group has shown that He can decorate the surfaces of the nanoparticle inclusions without growing into large bubbles. So that this

could be an important mechanism to avoid swelling and maintain high-temperature strength. Other materials which should be considered include nuclear fuels where bubble growth is an important problem. The role of defect should also be examined because experiment has shown that the gases prefer to segregate to grain boundaries although they can also form within the grains as shown in Figure 3.2.

One of the topics that was not considered in the thesis was the interaction with surfaces. It is known that beams of energetic inert gases can cause blistering and flaking of surfaces. The otf-KMC technique that was mentioned in Section 2.2 could be an ideal tool for investigating these effects. Indeed in fusion reactors it has been demonstrated experimentally that tungsten fuzz can form at high temperature due to the interaction of He with the walls of a tokomak device. However thin film growth of surfaces in a magnetron sputtering device also involve inert gas interactions and it would therefore be important to develop the work to see the effect in these systems.

In our work generally only one step of the oft-KMC technique was applied but this could be used in many different cases to examine the long time scale behaviour of inert gas diffusion in materials when the diffusion barriers are high. This was not a problem with He in bcc Fe since the diffusion of small He clusters could be investigated using MD since the energy barriers were much lower. The oft-KMC technique is ideal for the investigation of such surface effects.

The optimum gas to vacancy ratio has so far only been determined at 0 K. It should also be possible to determine this at higher temperatures. However some preliminary investigations to try to quantify and to calculate the pressure inside the bubble proved unsuccessful due to the large amount of statistics required for the investigation. However this problem could be revisited in a future study.

Finally as computing power increases *ab-initio* calculations become more feasible. So far these calculations have only been used for parametrising empirical potentials rather than for direct comparison with the results here. This is also a fruitful avenue for future investigation.

References

[1] P. J. Maziasz. Overview of microstructural evolution in neutron-irradiated austenitic stainless steels. *Journal of Nuclear Materials 205*, 205:118–145, 1993.

[2] S. J. Zinkle and L. L. Snead. Microstructure of copper and nickel irradiated with fission neutrons near 230 °C. *Journal of Nuclear Materials*, 225(1995):123–131, 1995.

[3] Y. Chimi, A. Iwase, N. Ishikawa, M. Kobiyama, T. Inami, and S. Okuda. Accumulation and recovery of defects in ion-irradiated nanocrystalline gold. *Journal of Nuclear Materials*, 297(3):355–357, 2001.

[4] B. N. Singh, A. Horsewell, P. Toft, and D. J. Edwards. Temperature and dose dependencies of microstructure and hardness of neutron irradiated OFHC copper. *Journal of Nuclear Materials*, 224(2):131–140, 1995.

[5] N. Hashimoto, T. S. Byun, K. Farrell, and S. J. Zinkle. Deformation microstructure of neutron-irradiated pure polycrystalline metals. *Journal of Nuclear Materials*, 329-333(1-3 PART B):947–952, 2004.

[6] D. Stewart, Y. Osetsky, and R. Stoller. Atomistic studies of formation and diffusion of helium clusters and bubbles in BCC iron. *Journal of Nuclear Materials*, 417(1-3):1110–1114, October 2011.

[7] H. Ullmaier. Review Paper the Influence of Helium on the Bulk Properties of Fusion Reactor. *Nucl. Fusion*, 24(8):1039, 1984.

[8] R. L. Klueh, N. Hashimoto, M. A. Sokolov, K. Shiba, and S. Jitsukawa. Mechanical properties of neutron-irradiated nickel-containing martensitic steels: I. Experimental study. *Journal of Nuclear Materials*, 357(1-3):156–168, 2006.

[9] H. V. Swijgenhoven, J. Moens, J. Vanoppen, and L. M. Stals. 5 keV Ar+-ion damage of an amorphous Fe-Ni-P-B alloy. *Scripta Metallurgica*, 15(6):629–632, 1981.

[10] R. S. Barnes and G. B. Redding. The behaviour of helium atoms injected into beryllium. *Journal of Nuclear Energy. Part A. Reactor Science*, 10:32–35, 1959.

[11] R. S. Barnes and D. J. Mazey. The Migration and Coalescence of Inert Gas Bubbles in Metals. *Proceedings of the Royal Society of London A: Mathematical, Physical and Engineering Sciences*, 275(1360):47–57, 1963.

[12] R. S. Barnes. The generation of vacancies in metals. *Philosophical Magazine*, 5(54):635–646, 1960.

[13] R. S. Barnes and D. J. Mazey. The nature of radiation-induced point defect clusters. *Philosophical Magazine*, 5(60):1247–1253, 1960.

[14] W. D. Wilson, M. I. Baskes, and C. L. Bisson. Atomistics of helium bubble formation in a face-centered-cubic metal. *Physical Review B*, 13:2470–2478, 1976.

[15] J. S. B. T. Evans and A. E. Dusoir. Proportionality and sample size as factors in intuitive statistical judgement. *Acta Psychologica*, 41:129–137, 1977.

[16] S. Blackwell, R. Smith, S. D. Kenny, and J. M. Walls. Modeling evaporation, ion-beam assist, and magnetron sputtering of thin metal films over realistic time scales. *Physical Review B*, 86(3):035416, July 2012.

[17] M. Song, K. Mitsuishi, K. Furuya, C. W. Allen, R. C. Birtcher, and S. E. Donnelly. Structure of nanometre-sized Xe particles embedded in Al crystals. *Journal of Microscopy*, 215(April):224–229, 2004.

[18] C. W. Allen, R. C. Birtcher, S. E. Donnelly, M. Song, K. Mitsuishi, K. Furura, and U. Dahmen. Determination of interfacial tensions for Xe nanoprecipitates in Al at 300 K. *Philosophical Magazine Letters*, 83(February 2015):57–64, 2003.

[19] C. W. Allen, R. C. Birtcher, S. E. Donnelly, K. Furuya, N. Ishikawa, and M. Song. Migration and coalescence of Xe nanoprecipitates in Al induced by electron irradiation at 300 K. *Applied Physics Letters*, 74(1999):2611–2613, 1999.

[20] R. C. Birtcherl, S. E. Donnelly, M. H. Song, N. Ishikawal, K. Mitsuishir, C. W. Allsnt, and R. C. Birtcherr. Melting and crystallization of Xe nanoprecipitates in Al under 1 MeV electron irradiation Melting 3lq . crystallization of Xe nanoprecipitates in Al under 1 MeV electron irradiation. *Journal of Electron Microscopy*, 51:S175–S181, 2002.

[21] K. Mitsuishi, M. Song, K. Furuya, R. C. Birtcher, C. W. Allen, and S. E. Donnelly. Observation of atomic processes in Xe nanocrystals embedded in Al under 1 MeV electron irradiation. *Nuclear Instruments and Methods in Physics Research Section B: Beam Interactions with Materials and Atoms*, 148:184–188, 1999.

[22] S. D. Kenny and A. P. Horsfield. Plato: A localised orbital based density functional theory code. *Computer Physics Communications*, 180(12):2616–2621, 2009.

[23] B. J. Alder and T. E. Wainwright. Phase Transition for a Hard Sphere System. *The Journal of Chemical Physics*, 27(5):1208, 1957.

[24] A. Rahman. Correlations in the motion of atoms in liquid Argon. *Physical Review A*, 136(2A):A405–A411, 1964.

[25] J. B. Gibson, A. N. Goland, M. Milgram, and G. H. Vineyard. Dynamics of radiation damage. *Physical Review*, 120(4):1229–1253, 1960.

[26] L. Vernon, S. D. Kenny, R. Smith, and E. Sanville. Growth mechanisms for TiO2 at its rutile (110) surface. *Physical Review B - Condensed Matter and Materials Physics*, 83(7):1–11, 2011.

[27] R. Smith, editor. *Atomic and Ion Collisions in Solids and at Surfaces*. Cambridge University Press, 1997. Cambridge Books Online.

[28] L. J. Vernon. *Modelling Growth of Rutile TiO2*. PhD thesis, 2010.

[29] C. Scott, S. Blackwell, L. Vernon, S. D. Kenny, M. Walls, and R. Smith. Atomistic surface erosion and thin film growth modelled over realistic time scales. *The Journal of Chemical Physics*, 135(17):174706, November 2011.

[30] G. Henkelman and H. Jónsson. Improved tangent estimate in the nudged elastic band method for finding minimum energy paths and saddle points. *Journal of Chemical Physics*, 113(22):9978–9985, 2000.

[31] J. M. Haile. *Molecular Dynamics Simulation: Elementary Methods*. John Wiley & Sons, Inc., New York, 1st edition, 1992.

[32] M. S. Daw, I. Baskes, S. N. Laboratories, and I. Introduction. Embedded-atom method: Derivation and application to impurities, surfaces, and other defects in metals. *Physical Review B*, 29(12):6443–6453, 1984.

[33] M. W. Finnis and J. E. Sinclair. A simple empirical N-body potential for transition metals. *Philosophical Magazine A*, 50(1):45–55, 1984.

[34] N.W. Ashcroft and N.D. Mermin. *Solid State Physics*. Saunders College, Philadelphia, 1976.

[35] J. E. Jones. On the determination of molecular fields. ii. from the equation of state of a gas. *Proceedings of the Royal Society of London A: Mathematical, Physical and Engineering Sciences*, 106(738):463–477, 1924.

[36] J. F. Ziegler, J. P. Biersack, and U. Littmark. *The Stopping and Ion Range of Ions in Matter*. Pergamon Press, New York, 1985.

[37] R. A. Aziz, A. R. Janzen, and M. R. Moldover. Ab Initio Calculations for Helium: A Standard for Transport Property Measurements. *Physical Review Letters*, 74(9):1586–1589, 1995.

[38] R. A. Aziz and M. J. Slaman. An Analysis of the ITS-90 Relations for the Non-Ideality of 3 He and 4 He: Recommended Relations Based on a New Interatomic Potential for Helium. *Metrologia*, 27(4):211–219, 1990.

[39] M. S. Daw and M. I. Baskes. Semiempirical, quantum mechanical calculation of hydrogen embrittlement in metals. *Physical Review Letters*, 50(17):1285–1288, 1983.

[40] G. J. Ackland, D. J. Bacon, A. F. Calder, and T. Harry. Computer simulation of point defect properties in dilute FeCu alloy using a many-body interatomic potential. *Philosophical Magazine A*, 75(3):713–732, 1997.

[41] M. I. Mendelev, S. Han, D. J. Srolovitz, G. J. Ackland, D. Y. Sun, and M. Asta. Development of new interatomic potentials appropriate for crystalline and liquid iron. *Philosophical Magazine*, 83(35):3977–3994, 2003.

[42] G. J. Ackland, M. I. Mendelev, D. J. Srolovitz, S. Han, and A. V. Barashev. Development of an interatomic potential for phosphorus impurities in -iron. *Journal of Physics: Condensed Matter*, 16(27):S2629–S2642, July 2004.

[43] J. P. Biersack and J. F. Ziegler. Refined universal potentials in atomic collisions. *Nuclear Instruments and Methods in Physics Research*, 194(13):93–100, 1982.

[44] F. Gao, H. Q. Deng, H. L. Heinisch, and R. J. Kurtz. A new FeHe interatomic potential based on ab initio calculations in α-Fe. *Journal of Nuclear Materials*, 418(1-3):115–120, November 2011.

[45] R. E. Stoller, S. I. Golubov, P. J. Kamenski, T. Seletskaia, and Y. N. Osetsky. Implementation of a new FeHe three-body interatomic potential for molecular dynamics simulations. *Philosophical Magazine*, 90(7-8):923–934, March 2010.

[46] G. J. Ackland, D. J. Bacon, A. F. Calder, and T. Harry. Computer simulation of point defect properties in dilute FeCu alloy using a many-body interatomic potential. *Philosophical Magazine A*, 75(3):713–732, March 1997.

[47] A. F. Voter and S. P. Chen. Accurate Interatomic Potentials for Ni, Al and Ni3Al. In *Symposium I Characterization of Defects in Materials*, volume 82 of *MRS Online Proceedings Library*, 1986.

[48] James H. Rose, John R. Smith, Francisco Guinea, and John Ferrante. Universal features of the equation of state of metals. *Phys. Rev. B*, 29:2963–2969, Mar 1984.

[49] R. Fletcher and C. M. Reeves. Function minimization by conjugate gradients. *The Computer Journal*, 7:149–154, 1964.

[50] R. H. Byrd, P. H. Lu, J. Nocedal, and C. Y. Zhu. A Limited Memory Algorithm for Bound Constrained Optimization. *SIAM Journal on Scientific Computing*, 16(5):1190–1208, 1995.

[51] J. Morales and J. Nocedal. Remark on algorithm 778: L-BFGS-B: Fortran subroutines for large-scale bound constrained optimization. *ACM Transactions on Mathematical Software*, 38(1):1–4, 2011.

[52] W. G. Hoover. Canonical dynamics: Equilibrium phase-space distributions. *Phys. Rev. A*, 31:1695–1697, Mar 1985.

[53] T. Schneider and E. Stoll. Molecular-dynamics study of a three-dimensional one-component model for distortive phase transitions. *Phys. Rev. B*, 17:1302–1322, Feb 1978.

[54] H. J. C. Berendsen, J. P. M. Postma, W. F. van Gunsteren, A. DiNola, and J. R. Haak. Molecular dynamics with coupling to an external bath. *The Journal of Chemical Physics*, 81(8):3684–3690, 1984.

[55] G. Henkelman and H. Jónsson. Long time scale kinetic Monte Carlo simulations without lattice approximation and predefined event table. *Journal of Chemical Physics*, 115(21):9657–9666, 2001.

[56] G Henkelman and H. Jónsson. A dimer method for finding saddle points on high dimensional potential surfaces using only first derivatives. *The Journal of Chemical Physics*, 111(15):7010, 1999.

[57] G. T. Barkema and N. Mousseau. Event-based relaxation of continuous disordered systems. *Physical Review Letters*, 77(21):4358–4361, 1996.

[58] N. Mousseau and G. Barkema. Traveling through potential energy landscapes of disordered materials: The activation-relaxation technique. *Physical Review E*, 57(2):2419–2424, February 1998.

[59] A. Pedersen, S. F. Hafstein, and H. Jónsson. Efficient Sampling of Saddle Points with the Minimum-Mode Following Method. *SIAM Journal on Scientific Computing*, 33(2):633–652, January 2011.

[60] C. C. Paige. Computational variants of the Lanczos method for the eigenproblem. *IMA Journal of Applied Mathematics*, 10:373–381, 1972.

[61] B. N. Parlett and D. S. Scott. The Lanczos algorithm with selective orthogonalization. *Mathematics of Computation*, 33(145):217, 1979.

[62] G. Henkelman and H. Jónsson. Improved tangent estimate in the nudged elastic band method for finding minimum energy paths and saddle points. *The Journal of Chemical Physics*, 113(22):9978, 2000.

[63] W. N. E, W. Q. Ren, and E. Vanden-Eijnden. String Method for the Study of Rare Events. *Physical Review B*, 66(5):052301, 2002.

[64] B. Peters, A. Heyden, A. T. Bell, and A. Chakraborty. A growing string method for determining transition states: comparison to the nudged elastic band and string methods. *The Journal of Chemical Physics*, 120(17):7877–86, May 2004.

[65] G. H. Vineyard. Frequency factors and isotope effects in solid state rate processes. *Journal of Physics and Chemistry of Solids*, 3(1-2):121–127, 1957.

[66] S. J. Zinkle. Fusion materials science: Overview of challenges and recent progress. *Physics of Plasmas*, 12(5):058101, 2005.

[67] R. J. Kurtz, A. Alamo, E. Lucon, Q. Huang, S. Jitsukawa, A. Kimura, R. L. Klueh, G. R. Odette, C. Petersen, M. A. Sokolov, P. Spätig, and J. W. Rensman. Recent progress toward development of reduced activation ferritic/martensitic steels for fusion structural applications. *Journal of Nuclear Materials*, 386-388:411–417, April 2009.

[68] G Lucas and R Schäublin. Helium effects on displacement cascades in α-iron. *Journal of Physics: Condensed Matter*, 20(41):415206, October 2008.

[69] S. J. Zinkle, P. J. Maziasz, and R. E. Stoller. Does dependence of microstructural evolution in neutron-irradiated austenitic stainless steel. *Journal of Nuclear Materials*, 206(2-3):266–286, 2008.

[70] T. Yamamoto, G. R. Odette, P. Miao, D. J. Edwards, and R. J. Kurtz. Helium effects on microstructural evolution in tempered martensitic steels : In situ helium implanter studies in HFIR. *Journal of Nuclear Materials*, 386-388:338–341, 2009.

[71] K. Ono. Formation and migration of helium bubbles in Fe and Fe 9Cr ferritic alloy. *Journal of Nuclear Materials*, 307-311(2002):1507–1512, 2010.

[72] J. Henry, L. Vincent, X. Averty, B. Marini, and P. Jung. Effect of a high helium content on the flow and fracture properties of a 9Cr martensitic steel. *Journal of Nuclear Materials*, 367-370:411–416, August 2007.

[73] K. Y. Yu, Y. Liu, C. Sun, H. Wang, L. Shao, E. G. Fu, and X. Zhang. Radiation damage in helium ion irradiated nanocrystalline Fe. *Journal of Nuclear Materials*, 425(1-3):140–146, June 2012.

[74] A. Caro, J. Hetherly, A. Stukowski, M. Caro, E. Martinez, S. Srivilliputhur, L. Zepeda-Ruiz, and M. Nastasi. Properties of Helium bubbles in Fe and FeCr alloys. *Journal of Nuclear Materials*, 418(1-3):261–268, November 2011.

[75] A. Caro, D. Schwen, and E. Martinez. Structure of nanoscale gas bubbles in metals. *Applied Physics Letters*, 103(21):213115, 2013.

[76] N. Gao, H. Van Swygenhoven, M. Victoria, and J. Chen. Formation of dislocation loops during He clustering in bcc Fe. *Journal of Physics: Condensed Matter*, 23(44):442201, November 2011.

[77] Z. F. Di, X. M. Bai, Q. M. Wei, J. Won, R. G. Hoagland, Y. Q. Wang, A. Misra, B. P. Uberuaga, and M. Nastasi. Tunable helium bubble superlattice ordered by screw dislocation network. *Physical Review B*, 84(5):052101, August 2011.

[78] R. E. Stoller and Yu. N. Osetsky. An atomistic assessment of helium behavior in iron. *Journal of Nuclear Materials*, 455(1-3):258–262, December 2014.

[79] D. M. Stewart, Y. N. Osetskiy, and R. E. Stoller. Atomistic Study of Helium Bubbles in Fe: Equilibrium State. In *MRS Proceedings*, volume 1298 of *MRS Proceedings*, pages 79–83, 2011.

[80] T. Jourdan and J. P. Crocombette. A variable-gap model for calculating free energies of helium bubbles in metals. *Journal of Nuclear Materials*, 418(1-3):98–105, November 2011.

[81] S. M. Hafez Haghighat and R. Schäublin. Influence of the stress field due to pressurized nanometric He bubbles on the mobility of an edge dislocation in iron. *Philosophical Magazine*, 90(7-8):1075–1100, March 2010.

[82] E. Hayward and C. Deo. Synergistic effects in hydrogen-helium bubbles. *Journal of Physics: Condensed Matter*, 24(26):265402, July 2012.

[83] D. Terentyev, N. Juslin, K. Nordlund, and N. Sandberg. Fast three dimensional migration of He clusters in bcc Fe and FeCr alloys. *Journal of Applied Physics*, 105(10):103509, 2009.

[84] D. J. Hepburn, D. Ferguson, S. Gardner, and G. J. Ackland. First-principles study of helium, carbon, and nitrogen in austenite, dilute austenitic iron alloys, and nickel. *Physical Review B*, 88(2):024115, July 2013.

[85] L. Yang, H. Q. Deng, F. Gao, H. L. Heinisch, R. J. Kurtz, S. Y. Hu, Y. L. Li, and X. T. Zu. Atomistic studies of nucleation of He clusters and bubbles in bcc iron. *Nuclear Instruments and Methods in Physics Research Section B*, 303:68–71, May 2013.

[86] N. Gao, M. Victoria, J. Chen, and H. Van Swygenhoven. Helium-vacancy cluster in a single bcc iron crystal lattice. *Journal of Physics: Condensed Matter*, 23(24):245403, June 2011.

[87] K. Morishita. Atomistic evaluation of the point defect capture efficiency of He-V clusters in α-Fe. *Nuclear Instruments and Methods in Physics Research, Section B: Beam Interactions with Materials and Atoms*, 255:41–46, 2007.

[88] H. Trinkaus. Energetics and formation kinetics of helium bubbles in metals. *Radiation Effects*, 78(770172261):189–211, 1983.

[89] X. Gai, R. Smith, and S. D. Kenny. Helium Bubbles in Fe: Equilibrium Configurations and Modification by Radiation. *MRS Proceedings*, 1514:21–26, February 2013.

[90] X. Gai, T. Lazauskas, R. Smith, and S. D. Kenny. Helium bubbles in bcc Fe and their interactions with irradiation. *Journal of Nuclear Materials*, 2014.

[91] C Kittle. *Introduction to Solid State Physics*. John Wiley & Sons, Inc., Hoboken, 8th edition, 2005.

[92] E. Hayward and C. Deo. Energetics of small hydrogen-vacancy clusters in bcc iron. *Journal of Physics: Condensed Matter*, 23(42):425402, October 2011.

[93] N. Metropolis, A. W. Rosenbluth, M. N. Rosenbluth, A. H. Teller, and E. Teller. Equation of State Calculations by Fast Computing Machines. *The Journal of Chemical Physics*, 21(6):1087, 1953.

[94] M. C. Marinica, F. Willaime, and N. Mousseau. Energy landscape of small clusters of self-interstitial dumbbells in iron. *Physical Review B - Condensed Matter and Materials Physics*, 83(9):1–14, 2011.

[95] H. Schultz. Defect parameters of b.c.c. metals: group-specific trends. *Materials Science and Engineering: A*, 141(2):149–167, 1991.

[96] C. Domain and C. S. Becquart. *Ab initio* calculations of defects in Fe and dilute Fe-Cu alloys. *Phys. Rev. B*, 65:024103, Dec 2001.

[97] C. C. Fu, F. Willaime, and P. Ordejón. Stability and Mobility of Mono- and Di-Interstitials in α-Fe. *Physical Review Letters*, 92(17):1–4, April 2004.

[98] F. Willaime, C.C. Fu, M.C. Marinica, and J. T. Dalla. Stability and mobility of self-interstitials and small interstitial clusters in -iron: ab initio and empirical potential calculations. *Nuclear Instruments and Methods in Physics Research Section B: Beam Interactions with Materials and Atoms*, 228(14):92–99, 2005. Proceedings of the Seventh International Conference on Computer Simulation of Radiation Effects in Solids.

[99] S. X. Jin, L. P. Guo, Z. Yang, D. J. Fu, C. S. Liu, R. Tang, F. H. Liu, Y. X. Qiao, and H. D. Zhang. Microstructural evolution of P92 ferritic/martensitic steel under argon ion irradiation. *Materials Characterization*, 62:136–142, 2011.

[100] M. Klimenkov. Quantitative measurement of argon inside of nano-sized bubbles in ODS steels. *Journal of Nuclear Materials*, 411(1-3):160–162, 2011.

[101] A. K. Tyagi, R. V. Nandedkar, and K. Krishan. Helium and argon ion damage in metallic glasses. *Journal of Nuclear Materials*, 122:732–736, 1984.

[102] I. Sakamoto, H. Tanoue, N. Hayashi, S. Honda, M. Nawate, and Y. Ikeda. Ar ion irradiation in Au / Fe multilayers. *Journal of Magnetism and Magnetic Materials*, 193:507–510, 1999.

[103] J. F. Dinhut and M. F. Denanot. Solid xenon bubbles in Fe and Mo thin films. *Materials Letters*, 17:37–41, 1993.

[104] C. Templier, R. J. Gaboriaud, and H. Garem. Precipitation of implanted xenon in aluminium. *Materials Science and Engineering*, 69(1):63–66, 1985.

[105] S. Gavarini, N. Toulhoat, C. Peaucelle, P. Martin, J. Mende, Y. Pipon, and H. Jaffrezic. Xenon migration behaviour in titanium nitride. *Journal of Nuclear Materials*, 362:364–373, 2007.

[106] M. Schmid, W. Hebenstreit, P. Varga, and S. Crampin. Quantum Wells and Electron Interference Phenomena in Al due to Subsurface Noble Gas Bubbles. *Physical Review Letters*, 76(13):2298–2301, 1996.

[107] C. Biswas, A. K. Shukla, S. Banik, S. R. Barman, and A. Chakrabarti. Argon Nanobubbles in Al(111): A Photoemission Study. *Physical Review Letters*, 92(11):115506–1, 2004.

[108] C. J. Rossouw and S. E. Donnelly. Superheating of small solid-argon bubbles in aluminum. *Phys. Rev. Lett.*, 55(27):2960–2963, December 1985.

[109] R. S. Dhaka, K. Gururaj, S. Abhaya, G. Amarendra, S. Amirthapandian, B. K. Panigrahi, K. G. M. Nair, N. P. Lalla, and S. R. Barman. Depth-resolved positron annihilation studies of argon nanobubbles in aluminum. *Journal of Applied Physics*, 105(5), 2009.

[110] R. J. Cox and P. J. Goodhew. A combined TEM and X-ray microanalytical study of argon in aluminium. *Journal of Nuclear Materials*, 154(2-3):233–244, 1988.

[111] M. G. Ortega, S. B. Ramos de Debiaggi, and A. M. Monti. Self-diffusion in FCC metals: Static and dynamic simulations in aluminium and nickel. *Physica Status Solidi (B) Basic Research*, 234(1):506–521, 2002.

[112] T. P C Klaver and J. H. Chen. Density functional theory study of alloy element interstitials in Al. *Journal of Computer-Aided Materials Design*, 10:155–162, 2003.

[113] R. Stumpf and M. Scheffler. Ab-initio Calculations of Energies and Self-Diffusion on Flat and Stepped Surfaces of Al and their Implications on Crystal Growth. *Physical Review B*, 53(8):4958–4973, 1994.